ABSTRACT

Title of Dissertation:	THREE-DIMENSIONAL CHARACTERIZATION AND MODULATION OF CORNEAL BIOMECHANICS VIA BRILLOUIN MICROSCOPY
	Joshua N. Webb, Doctor of Philosophy, 2021
Dissertation directed by:	Professor, Giuliano Scarcelli, Fischell Department of Bioengineering

Corneal mechanical properties are needed for diagnosing and monitoring the progression of ocular disorders such as keratoconus, screening for refractive surgeries, and evaluating treatment procedures including corneal cross-linking. Alterations of these mechanical properties are often localized to a specific area within the cornea. However, there exists a clinical gap of measuring local mechanical properties as current methods are contact-based and provide global measurements. The goal of this dissertation is to close this gap by establishing a three-dimensional, noninvasive characterization method of corneal biomechanics.

Previously, our laboratory developed Brillouin microscopy as an imaging modality which can noninvasively extract mechanical measurements of a material. Here, using Brillouin microscopy, we characterized the stiffening effects of accelerated and localized cross-linking procedures with three-dimensional resolution. However,

existing procedures to extract elastic modulus information from Brillouin measurements rely on empirical calibrations because a fundamental understanding between the two had not yet been established. In practice, this limits Brillouin measurements to relative softening / stiffening information, which, while useful to compare protocol efficacies, are not optimal for modeling long-term shape behavior of the cornea in clinical settings.

Here, we address this shortcoming of Brillouin microscopy. First, we identified that both Brillouin-derived mechanical modulus and traditional elastic modulus are dependent on two major biophysical factors: hydration and the mechanical properties of the solid matrix. We derived and experimentally verified a quantitative relationship to describe the distinct moduli dependencies of such factors. Based on these relationships, we derived a procedure to extract the elastic modulus of the cornea from experimental measurements of Brillouin frequency shift and hydration, two clinically available parameters. Thus, the work presented here establishes a spatially resolved, noninvasive method for measuring corneal elastic modulus.

THREE-DIMENSIONAL CHARACTERIZATION AND MODULATION OF CORNEAL BIOMECHANICS VIA BRILLOUIN MICROSCOPY

by

Joshua N. Webb

Dissertation submitted to the Faculty of the Graduate School of the
University of Maryland, College Park, in partial fulfillment
of the requirements for the degree of
Doctor of Philosophy
2021

Advisory Committee:
Professor Giuliano Scarcelli, Chair
Professor Ian White
Professor Alisa Morss Clyne
Professor Huang Chiao Huang
Professor Peter Kofinas
Professor James Bradley Randleman, M.D.

DEDICATION

To my future wife, Emily, for being my biggest motivation and number one fan. Not a single word was written, nor data point collected without your unconditional love and support.

To my mom, Liz, for teaching me to always strive for happiness. To my dad, Norm, for teaching me to always strive to be the best. I am lucky enough to benefit from a great complement of lessons and an even greater complement of parents.

ACKNOWLEDGEMENTS

First, thank you, Giuliano. I am incredibly grateful to benefit from your profound knowledge and evident excitement towards my field. You have pushed me to raise my standard as a writer, taught me to be comprehensive as a researcher, and showed me what it takes to succeed as a scientist. Thank you for your open-door policy by always answering a knock on your office door, an email, or a message on your phone. My appreciation for your mentorship inside of lab is only exceeded by that of your mentorship outside of lab. After four and a half years of being a member of your group, I am leaving a better scientist and a better man thanks to you.

Thank you to my incredibly knowledgeable and helpful lab mates throughout my time in the Optics Biotech Laboratory. Specifically, thank you Dr. Jitao Zhang for helping optimize the Brillouin microscopy setup; Dr. Hongyuan Zhang for helping me with the arithmetic of the theoretical models; Dr. Johnny Suzuki for helping collect Brillouin measurements; Antonio Fiore for helping me consider the index of refraction contributions to Brillouin frequency shift within a rotated cornea; Milos Nikolic for helping me optimize the MATLAB code needed to analyze Brillouin measurements; Christina Conrad for discussing the general scopes of my projects; and Raymundo Rodriguez and Erin Langille for collecting and analyzing mechanical measurements. Thank you to Dr. Giulia Zanini, Dr. Eitan Edrei, Romanus Hutchins, Maggie Zhou, Justin Schumacher, Jake Rosvold, Chenchen Handler, Thomas Mumford, and Angelina

Nou for giving valued feedback of my data throughout the course of my graduate research.

Thank you to my dissertation committee members: Dr. Ian White, Dr. Alisa Morss Clyne, Dr. Huang Chiao Huang, Dr. Peter Kofinas, and Dr. Brad Randleman. The range of topics throughout my dissertation required a wide range of expertise and support, and I am extremely grateful to have had such a committee.

Finally, I would like to humbly thank Robert Fischell for generously funding a year of my research via the Fischell Fellowship.

TABLE OF CONTENTS

CHAPTER 1: INTRODUCTION

The goal of this dissertation is to address a large clinical gap in the diagnostics and characterizations of ocular disorders, such as corneal ectasia, and treatments, such as corneal cross-linking. The clinically observed thinning and bulging associated with ectasia are the results of a localized mechanical imbalance in the anterior segment of the eye. Subsequently, uniformly strengthening the entire cornea via corneal cross-linking is the current standard to stop the progression of unwanted alterations in morphology. However, focusing the cross-linking to the bulged area of an ectatic cornea has shown to increase the long-term refractive outcome by restoring healthy topography.

While measuring local mechanical properties potentially yields earlier diagnostics and personal, localized treatment protocols, current mechanical characterization methods are global and contact-based / invasive. Here, Brillouin microscopy is investigated to close the gap in current technology by noninvasively measuring corneal mechanics with three-dimensional, micron-level resolution. Chapters 3 and 4 validate Brillouin microscopy as a method to measure clinically relevant, three dimensional changes in corneal mechanical properties by characterizing spatially varying properties after two clinically relevant procedures: accelerated and localized cross-linking. However, due to a lack of universal relationship between Brillouin frequency shift and mechanical modulus, Brillouin measurements require carefully controlled experiments with

empirical calibrations. To establish practical clinical capabilities, a quantitative relationship between Brillouin measurements and elastic modulus is necessary. Chapter 5 demonstrates two factors independently affect the Brillouin frequency shift of the cornea: hydration and the solid matrix. Expanding on such, Chapter 6 theoretically and experimentally quantifies the dependence of Brillouin shift and elastic modulus on both hydration and the solid matrix of the cornea. Using the similar contributing factors, a quantified relationship of elastic modulus, depending on both corneal hydration and Brillouin shift, is yielded. This relationship allows for a practical, noninvasive measurement of the elastic modulus of a cornea.

CHAPTER 2: BACKGROUND

2.1 Cornea Anatomy and Structure

The cornea is the outermost, transparent layer of the eye and responsible for over two-thirds of the total refractive power of the human eye, about 43 of the 63 total diopters. The human cornea (approximately 550 μm) is made up of five distinct layers as shown in **Figure 2.1** including, from anterior inwards: epithelium (~45 μm), Bowman's layer (~15 μm), stroma (~500 μm), Descemet's Membrane (~10 μm), and endothelium (~5 μm). The epithelium acts as a thin protective layer of the cornea while endothelial cells help maintain the hydration state within the cornea which is important for maintaining clarity.[1] The Bowman's layer and Descemet's membrane are made of randomly interwoven collagen fibers and act as a protective barrier to the respective adjacent layers.[2,3] The stromal layer accounts for about 90% of the corneal thickness and a majority of the corneal mechanical properties.[4,5]

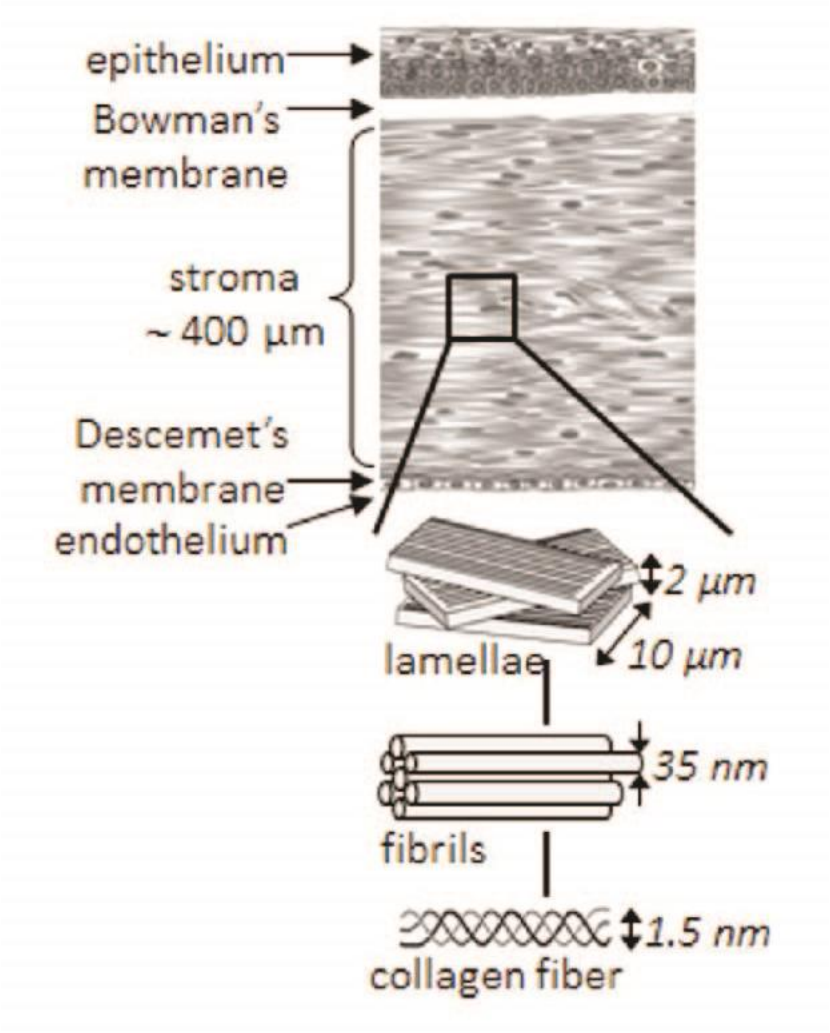

Figure 2.1: Diagram of the layers within the cornea. Adapted with permission.[6]

The stroma is made up of type I, III, V, and VI collagen fibrils (~35 nm diameter) bundled together and organized in flattened layers called lamellae (~2 µm).[7] In the central cornea, roughly 200 layers of lamellae are stacked on top of one another at orthogonal angles while maintaining a preferred direction parallel to the corneal surface.[8] However, it is common for the fibrils within the lamellae to vertically branch out and become interwoven with those of adjacent layers, a phenomenon that increases the rigidity of cornea. As shown in **Figure 2.2**, fibral branching is a depth-dependent

phenomenon.[9] The anterior of the stroma is made up of a dense network of fibers branching in both the lateral and axial directions while the posterior network is much more organized as the fibers run almost exclusively in the lateral direction parallel to the corneal surface. The more spaciously organized posterior section promotes greater water content.[10] As a result, the stiffness of the stroma is greater in the anterior with a decline to the posterior.[11–13] Located between the lamellae lie keratocytes, transparent cells responsible for synthesizing and maintaining the collagen matrix, proteoglycans, and water.[2,3] Keratocytes are more densely populated within the anterior section of the cornea (~29,000 cells/mm^3) versus the posterior sections (~20,000 cells/mm^3).[14] However, it a relatively small number compared to the estimated $2*10^{12}$ cells/mm^3 in other human tissue.[10]

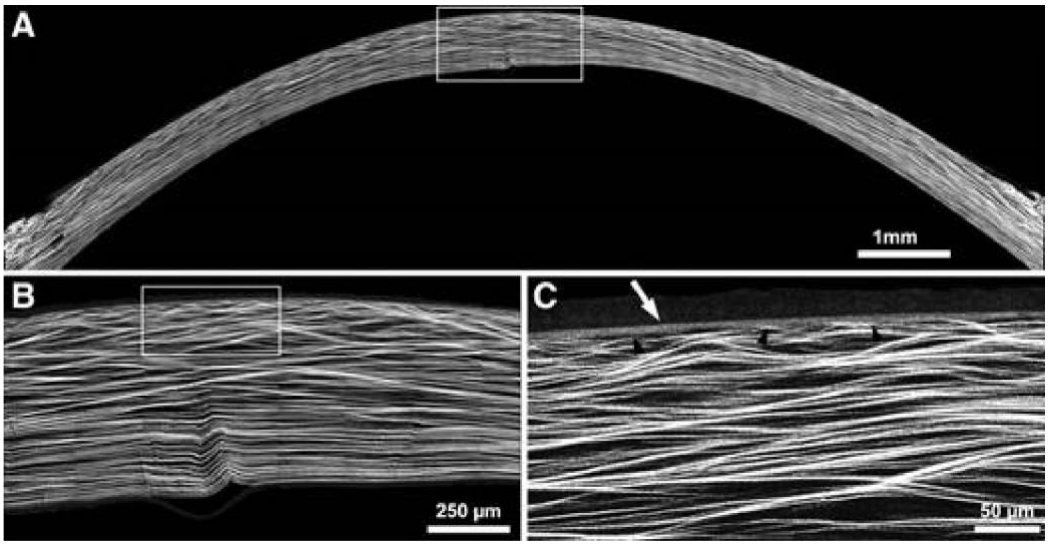

Figure 2.2: Nonlinear optical high-resolution macroscopy image of the cornea. **A:** High resolution image of the corneal cross section **B:** Zoomed-in view of the central portion of the cornea **C:** Anterior section of the cornea. All images show a depth-

dependent branching of collagen fibers as more interweaving occurs in the anterior. Adapted with permission.[9]

2.2 Corneal Ectasia

The cornea relies on its symmetric curvature to properly refract light. Corneal ectatic disorders are characterized by a disruption of that curvature via a localized coning / bulging of the cornea[15,16] and account for over 15% of all corneal transplants performed.[17] Corneal ectatic disorders include keratoconus, in which the progressive coning is more centrally located; pellucidal marginal degeneration, in which the progressive coning is peripherally located, and keratogolobus, which is peripherally located coning is present at birth. Here, we will continue to focus on the most prevalent of the disorders, keratoconus. Keratoconus affects ~1/372 in European countries and as high as ~1/21 in Middle Eastern countries.[18–21] Keratoconus, generally affecting those between the ages of 10 and 25, may progress very slowly over the next few decades of life. If left untreated, keratoconus can result in corneal breakdown, scarring, and the complete loss of functional vision. Ectasia can be brought on following refractive surgery, specifically a result of the ~1 million LASIK operations per year,[16,18,22]

Corneal ectasia is generally graded as mild (< 48 Diopters), moderate (48 to 53 Diopters), or advanced (> 53 Diopters) depending on the steepest curvature of the cone. In addition to measuring the morphology of the cornea, ectasia is often monitored via a thinning of the corneal thickness at the compromised location. However, topography

and tomography measurements of the thinning and bulging associated with the disorder are most relevant for later-stage and severe diagnosis. The alteration in morphology seen in ectasia has long been believed to be due to a compromise in local corneal stiffness; indeed, the disease is highly correlated with mechanical trauma and eye rubbing,[23] a decrease in interwoven collagen fibers and cross-links within the cornea,[24] an increase in proteolytic enzyme digestion of the stroma,[25] and a region-dependent modulus decrease co-located with cone formation.[18] Due to changes in biomechanics preceding clinically observed changes in corneal morphology, efforts have started to focus on using mechanical measurement tools for earlier diagnosis of ectasia.[26–28] Recent studies have shown a significantly increased sensitivity in detecting early, sub-clinical ectasia using biomechanical indexes compared to more traditional topography and tomography measurements.[29–31]

2.3 Corneal Cross-linking

The biomechanical weakening of ectatic corneas is due to the reduction of interwoven fibers connected vertically to adjacent lamellae.[32,33] In the 1990s, it was proposed that cross-linking adjacent collagen fibers together, a phenomenon widely established at the time in polymer chemistry[34] as well as naturally within the human body,[35] could increase the stiffness of the ectatic cornea, thereby, halting any unwanted change in morphology.[36] The procedure, known as the Dresden protocol for the city of origin, calls for soaking the cornea with a photosensitizer (riboflavin) for 30 minutes followed by uniform 3 mW/cm^2 UV-A exposure for another 30 minutes (5.4 J/cm^2) during which riboflavin is continuously applied in 3-5 minute intervals.[37] The first 10-15 seconds of

the cross-linking procedure begins with a Type-II photosensitized reaction as the cornea is in an oxygenated environment. When riboflavin is exposed to UV-A light under aerobic conditions, riboflavin (Rf) is excited to its triplet state (Rf^{*}_{3}) and reacts with available oxygen (O_2) to form singlet molecular oxygen.[38,39] The singlet oxygen has been shown as the primary oxidant in the cross-linking reaction.[40,41] The singlet oxygen attacks double bond groups within a monomer-assembled collagen fibril and form a covalent link between adjacent chains. The oxygen within the cornea is depleted within the first few seconds, upon which the cross-linking reaction turns to a direct oxidative interaction in which oxygen is not required. During these photochemical reactions, Rf^{*}_{3} directly interacts with proteoglycan proteins and the collagen matrix to generate radicals, thereby, promoting cross-linking. Oxygen is naturally replenished throughout the procedure until a Type-II mechanism can play an additional, enhancing role.[39] This initial procedure, performed on *ex vivo* porcine corneas, increased the corneal stiffness by 70%.[36] By increasing the corneal stiffness, it was theorized the morphological changes of the corneas could be halted, saving further loss of refraction. In 2003, the protocol was successfully performed *in vivo* on humans and resulted in only 1 / 23 eyes exhibiting an increase in corneal steeping at the one year post-operation follow up compared to 5 / 23 non-cross-linked control eyes exhibiting a increase in steepness.[42]

While widely used outside of the United States since the early 2000s, the U.S. Food and Drug Administration did not approve corneal cross-linking (CXL) until 2016.[42] In part, this is due to mixed results of CXL as no method could accurately measure the

mechanics of the cornea *in vivo* before and after the procedure. Additionally, adding to the mixed results, experimental protocols have been attempted to improve the treatment leading to a notable difficulty in pinning down the effects of a specific procedure. The development of different procedures stems from the clear shortcomings of the original protocol. For one, the standard Dresden protocol calls for the removal of the cornea epithelium. To minimize patient discomfort and risk of infection, different trans-epithelial CXL procedures have been investigated but results showed suboptimal results as the epithelial barrier prevented CXL from occurring.[43–45]

Additionally, the standard cross-lining procedure is time consuming for the doctor and uncomfortable for the patient. Therefore, clinicians and researchers recently focused on decreasing the overall exposure time of the procedure. It was proposed that treatment time could be shortened by increasing the radiation intensity because the biological effects should only depend on the total energy dose.[46,47] Speeding up the radiation step of the procedure is known as accelerated cross-linking (A-CXL). Although protocols using intensities up to 50 mW/cm^2 for less than 2 minutes of exposure time were suggested,[47] the evidence does not conclusively support accelerated CXL in clinical settings. For example, Wernli *et al.* reported a significant reduction in CXL stiffening when the procedure was performed above a 45 mW/cm^2 intensity[48] and Hammer *et al*. found a decrease in CXL effectiveness when comparing the standard protocol with a treatment using a radiation intensity of just 9 mW/cm^2.[48]

In another attempt to improve the standard CXL procedure, efforts have focused on addressing the localized, focus nature of keratoconus. Roberts, *et al.* first proposed that, rather than uniformly strengthening the entire cornea as does the Dresden protocol, treating only the weaker area of the cornea could result in similar or enhanced results in halting ectasia.[26] Currently, localized cross-linking (L-CXL) is being investigated to lessen the risk of complications associated with the procedure and increase topographic flattening of the cornea compared to that of the Dresden protocol.[49,50] The procedure involves focusing the irradiation to the compromised areas of the cornea rather than the uniform irradiation used during the Dresden protocol. Currently, the irradiation area can be focused laterally by confining and controlling the diameter of the cross-linking light[50–52] as well as controlled along the depth axis by using multiphoton microscopy to focus the light and cross-link point-by-point.

Moving forward, we investigate accelerated cross-linking, focusing on decreasing the overall exposure time of the procedure, and localized cross-linking, focusing on limiting the irradiation to the area of compromised morphology. Both procedures produced mixed results, relying on *ex vivo* data or observational clinical follow ups to evaluate the effectiveness of the procedures due to lack of a three-dimensional, biomechanical characterization.

2.4 Corneal Mechanical Properties

The cornea, like most soft biological tissue, presents a nonlinear stress (σ) and strain (ε) relationship which contains a toe and heel region at low, physiological strains

followed by a more linear region at higher strains.[8,53,54] As demonstrated in **Figure 2.3.A**, this relationship corresponds to the uncrimping of the underlying collagen fibers, the toe region, followed by the sliding of collagen molecules past one another, the linear region. The nonlinearity of the stress and strain relationship necessitates context when describing the mechanical modulus of the cornea. For example, the modulus (E) is defined as the slope (σ / ε) at a specific stress or strain condition. As shown in **Figure 2.3.B**, modulus can be defined as the secant modulus, calculated by finding the ratio of stress to strain at any given condition, the tangent modulus, calculated by finding the derivative or slope between two stress or strain conditions, as well as via a number of other nonlinear models. For the purpose of this dissertation, we will define Elastic modulus similar to Tangent modulus, as the slope between two given strain conditions.

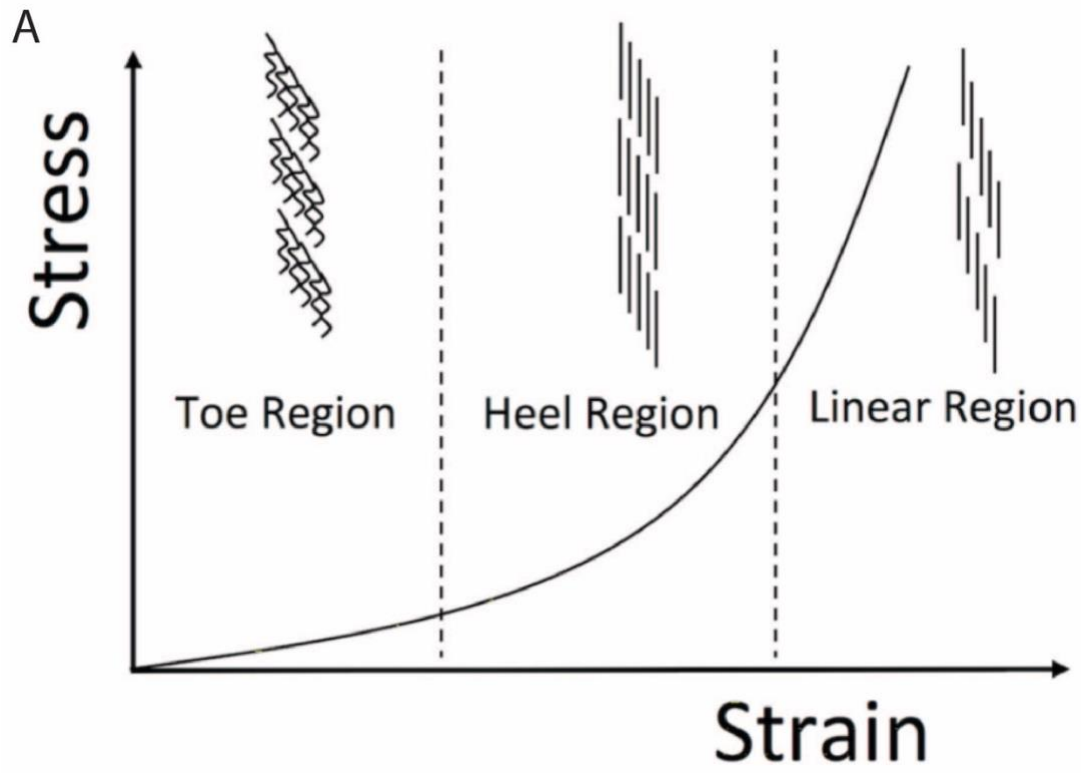

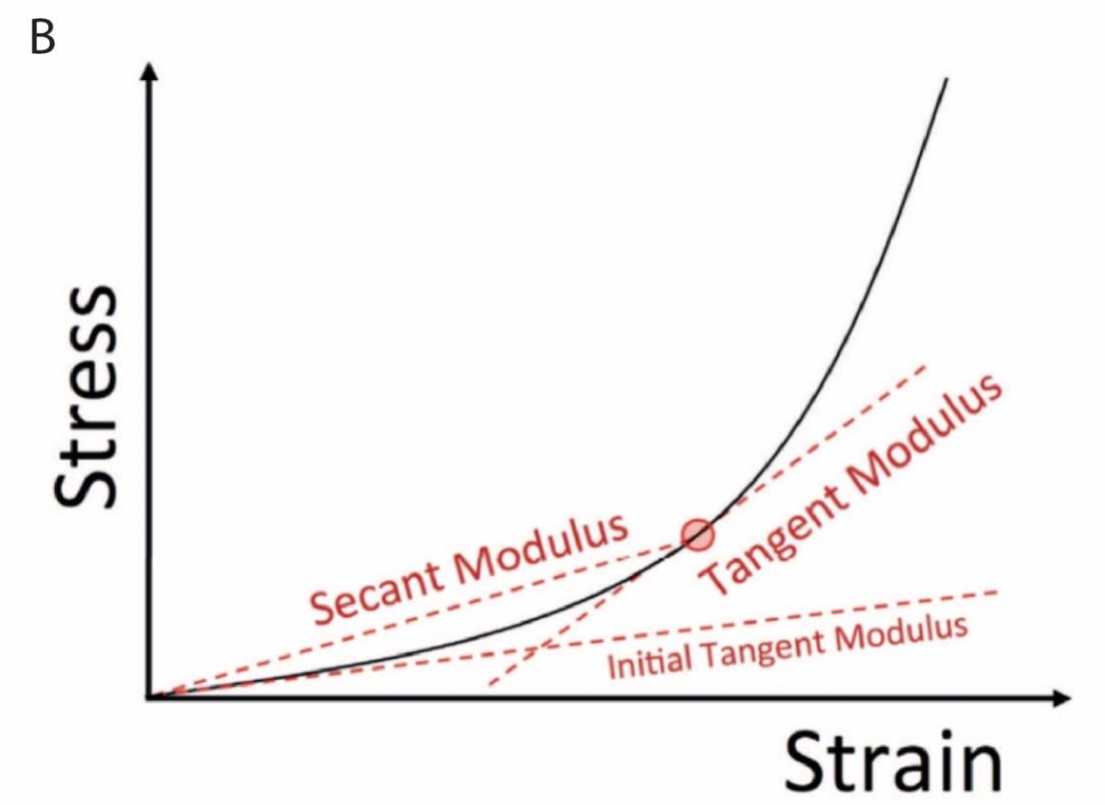

Figure 2.3: Nonlinear relationship between stress vs strain of the cornea. **A**: The nonlinear relationship can be attributed to the uncrimping, removal of microscopic kinks, and then molecular sliding of the collagen molecules. **B**: Examples of different ways to define the mechanical modulus of a corneal stress vs strain curve. Both figures adapted with permission.[8]

This nonlinear relationship is relevant *in vivo* because the stress on the cornea is due to the constant pressure from within the eye known as intraocular pressure (IOP) which can vary in healthy humans from 12 - 22 mmHg and in those with glaucoma from 21 - 70 mmHg.[55] Therefore, the magnitude of IOP and, thereby, the stress applied to the cornea, will influence the stiffness of the cornea at a given time. For example, Ko *et al*. has reported a ~100% increase in tangent modulus in corneas at 12 versus 24 mmHg

IOP.[56] It is important to note that physiological intraocular pressure is only expected to inflict ~14.5 kPa stress and less than a 2% strain on the cornea.[56,57] Especially in *ex vivo* experiments in which the corneas are undergoing large amounts of deformation, the reported modulus of the cornea is highly contingent on the strain at which it is measured due to the exponential relationship between stress and strain. For example, Wollensak *et al.* has reported a 225% increase in the elastic modulus (0.8 MPa vs 2.6 MPa) measured via tensile testing in a cornea under a 33.7 kPa and 86.5 kPa applied stress.

In addition to the nonlinear source of variability, the reported modulus of the cornea also significantly varies based on probing direction of the mechanical test. From a mechanical standpoint, the cornea is generally approximated as a transversely isotropic material,[58] meaning its mechanical properties are uniform on a given *en face* plane of the cornea. However, as the collagen matrix of the cornea displays a preferred directionality, the measured properties change if probed parallel or perpendicular to the surface.[59] Due to most of the collagen fibers running parallel to the surface of the cornea, the tangential modulus is significantly greater than the axial modulus measured orthogonal to the fibers. Even at the same strain, the elastic modulus found via mechanical tests which apply a force parallel to the collagen fibers has been reported to be up to hundredfold greater than that orthogonal to the fibers.[20,60] This is due to stromal collagen aligned parallel to the corneal surface better resisting tangential tensile forces compared to compressive forces working to bend the collagen. As an approximation, the cornea resembles a reinforced composite material with fibers

running in a preferential direction tangential to the surface. When forces are applied along the fiber direction, the Rule of Mixtures applies such that: $E_{tot} = E_1 f_1 + E_2 f_2 + \cdots E_i f_i$ where E_{tot} is the total elastic modulus for the material and E_i and f_i are the elastic modulus and volume fraction of layer i respectively; leading to the stiffest modulus measurement possible. Conversely, when a load is applied orthogonal to the fiber direction, the modulus is calculated by: $E_{tot} = \frac{1}{\frac{f_1}{E_1} + \frac{f_2}{E_2} + \cdots \frac{f_i}{E_i}}$; leading to the weakest modulus measurement. The modulus when a load is applied orthogonal to the collagen fiber direction is, therefore, expected to be dramatically less than the modulus measured when a load is applied in line with the fibers.

As another source of variability within the cornea, the mechanical properties of the cornea, largely dictated by fibral orientation and interconnectivity, exhibit a depth dependent behavior. The anterior of the cornea consists of a higher density of collagen fibers more frequently interwoven with vertically adjacent lamellae, often times extending and anchoring to the Bowman's membrane.[9] The frequency of interwoven fibers decreases with depth within the cornea, leading to the posterior section in which lamellae are loosely stacked and rarely interwoven. Subsequently, the stiffness of the cornea follows a similar depth dependent gradient as the anterior is at least 50% stiffer than the posterior section.[12]

2.5 Mechanical Modalities to Measure In Vivo Corneal Biomechanics

Until the early 2000s, corneal biomechanics could only be measured *ex vivo*. Then, corneal elastography was gradually introduced over the next few decades.

Fundamentally, elastography is the combination of external force and an imaging technique in order to monitor the displacement reaction to said force. In 2005, the Ocular Response Analyzer (ORA) was developed as the first device capable of estimating mechanical properties of the cornea *in vivo*.[61] The premise of ORA revolves around Non-Contact Tonometry (NCT), a device introduced in 1972 to estimate intraocular pressure (IOP).[62] The device administers a measurable air-puff force in order to cause the cornea to inwardly, momentarily deform. During the deformation, the cornea moves inward past applanation into a mild concavity, then responds outward again past applanation into its normal curved shape. Using infrared light and a photodetector, the corneal radius of curvature is monitored throughout the process.[63] In 2000, Luce *et. al.* developed a method to extract mechanical properties from the NCT procedure, known as ORA.[61] The pressure values at both the inward (P1) and outward (P2) applanations were measured, and due to viscous damping, the difference between P1 and P2 demonstrates the ability of the cornea to absorb and dissipate energy. However, due to its imaging system, the ORA is confined to measuring a single point on anterior surface of the corneal apex. The topographical single dimensionality of ORA presents clinical shortcomings. Keratoconus, as well as other ectatic disorders, is characterized by heterogenous mechanical properties and a localized weakening of the cornea often off of the central apex. Therefore, estimating the global mechanical properties of the cornea using an applied force to the center of the cornea extinguishes diagnostic sensitivity as the device as shown ineffective in diagnosing keraotconus.[64,65]

In 2013, Corneal Visualization Scheimpflug Technology (Corvis® ST) introduced an advanced visualization method to NCT.[66] Corvis® ST combines high-speed (4430 frames per second) imaging with an air puff pulse. During the 31 ms pulse, 140 images are captured of the entire central cross-section of the cornea. The Corvis® ST outputs more than 20 different parameters, including IOP, thickness, and detailed information on both applanation points. Certain parameters, including the length of the applanated segment, are reflective of biomechanical properties of the cornea.[67,68] However, intraocular pressure strongly influences Corvis® ST output parameters. Therefore, IOP must be taken into account when measuring biomechanical properties using this technique, strongly limiting the clinical potential. To address this shortcoming, Corvis® ST has been paired with Finite Element Modeling (FEM).[69–71] By using the corneal response to the air puff as an input, FEM iteratively and independently solves for both the IOP and overall, global mechanical properties of the cornea. However, this method is an indirect measurement of corneal biomechanics and not in real-time. Additionally, while an improvement from the one-dimensional measurements of the ORA, the current Corvis® ST system is still relying on measuring the corneal response to an exerted, large scale (mm) air puff force resulting in a global approach and results in overall mechanical estimations of the cornea. The Corvis® ST system, while sensitive to detecting keratoconus, was not sensitive enough to differentiate between the various stages of the disease.[72]

An improvement was made to the imaging device of previous elastography techniques by introducing Optical Coherence Elastography (OCE).[73] OCE is fundamentally

similar to the Corvis® ST device, however, now with an upgraded Optical Coherence Tomography (OCT) imaging system. OCT allows for depth-resolved, micron-level monitoring of corneal displacement. Like Corvis® ST, the device still relies on the single air puff force applied to the apex of the cornea. The now improved displacement measurements are then used as a more precise input into FEM algorithms, solving for biomechanical properties of the cornea. Current OCE systems still only acquire two dimensional cross-sectional images along the apex of the cornea, however, improving acquisition speeds of the OCT-based system could eventually allow for full three-dimensional imaging. Then, in contrast to the global estimations of corneal mechanical properties of previous elastography techniques, OCE would allow for spatially varied measurements in three-dimensions; a potentially vital characteristic of detecting the off-axis mechanical heterogeneity associated with keratoconus.

2.6 Brillouin Microscopy

Brillouin Microscopy has emerged as a noncontact imaging modality to map mechanical properties of biological samples in three dimension at micron-level resolution.[74–81] The technique stems from spontaneous Brillouin scattering; an inelastic scattering process that can be thought of as a combination of Bragg's diffraction and the Doppler Effect first documented by Leon Brillouin in 1922.[82] A monochromatic beam is directed through an objective lens into a material and interacts with spontaneous acoustic waves intrinsic to the sample. The acoustic waves within a material, by expanding and compressing the material, cause periodic fluctuations of density that travel at the speed of sound. The fluctuations of density lead to fluctuations

in refractive index similar to that of a diffraction grating or crystal plane (Bragg's diffraction). However, because the refractive index fluctuations are not static, the scattered light experiences a Doppler frequency shift known as Brillouin frequency shift. The Brillouin frequency shift was first acquired in 1970 using a scanning multipass tandem Fabry-Perot interferometer.[83] Over the next few decades, Brillouin scattering was used to characterize a vast array of material including metallic compounds,[84] hard tissue,[85] films,[86] and so on.[87] However, it was not until the early 2000s, with the development of multi-stage cross axis VIPA spectroscopy allowing for low illumination power and high spectral extinction, that biological samples could be measured.[88,89] Brillouin spectrometers were then combined with confocal microscopy, referred to in combination as Brillouin microscopy, to obtain three-dimensional resolution frequency measurements.[77,90,91] An example of the spectrometer output and acquired spectrum is shown in **Figure 2.4**.

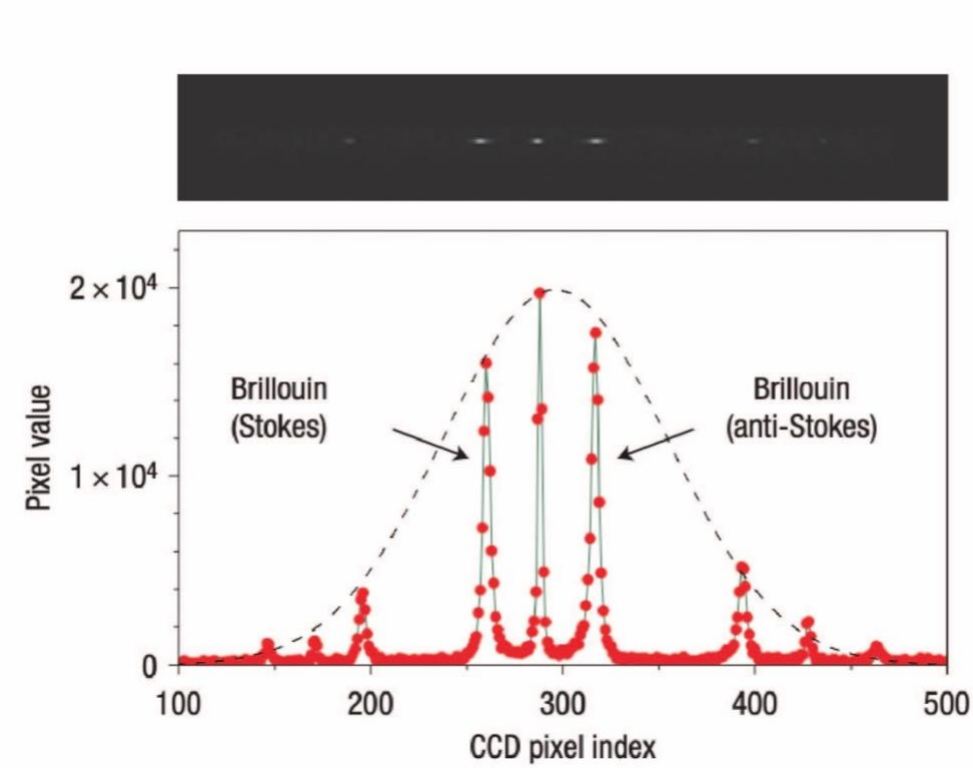

Figure 2.4: Brillouin spectrometer output and transmission profile of distilled water. Adapted with permission.[77]

Our laboratory uses the most up-to-date collection of Brillouin setup innovations (**Figure 2.5**), the most notable being the implementation of two VIPA etalons in cross-axis configuration to optimize extinction.[92] In our setup, we focus the beam onto a sample at relatively low power (10-15 mW) with millisecond acquisition time (~50 ms per pixel) and scan the sample to obtain localized frequency shifts in three dimensions. To quantify the Brillouin shift at each sample location, raw spectra from the charge-coupled device (CCD) camera are fitted using a Lorentzian function and calibrated using the known frequency shifts of water and methanol. From the Brillouin frequency

shift, the local mechanical properties of a material can be estimated using the following relationship:

$$M' = \frac{\rho {\nu_B}^2 {\lambda_i}^2}{4n^2} \qquad (Eqn.\ 2.1)$$

where *M'* is the Brillouin-derived longitudinal modulus (abbreviated throughout as Brillouin modulus), ν_B is the measured Brillouin frequency shift, n is the refractive index of the material, λ_i is the wavelength of the incident photons, and ρ is the density of the material. The density and refractive index parameters scale together, and the ratio of ρ/n^2 can be approximated to ~0.5 g/cm^3 contributing to less than 1% uncertainty in modulus estimation based on literature values.[15,93] Thus, longitudinal modulus can be yielded via Brillouin microscopy.

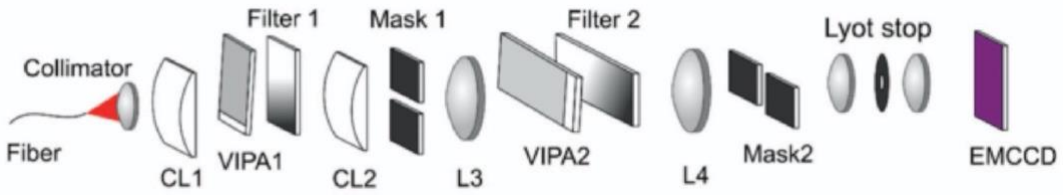

Figure 2.5: Schematic of Brillouin spectroscopy optical setup.[94]

2.7 Brillouin Microscopy Corneal Application

Brillouin Microscopy was first used to study corneal mechanics in 2012 in which Scarcelli *et al.* used the modality to measure the spatially-varying mechanical properties of cornea.[15] This was the first direct measurement of the depth-dependent variation in elastic modulus of the cornea, as shown in **Figure 2.6**.

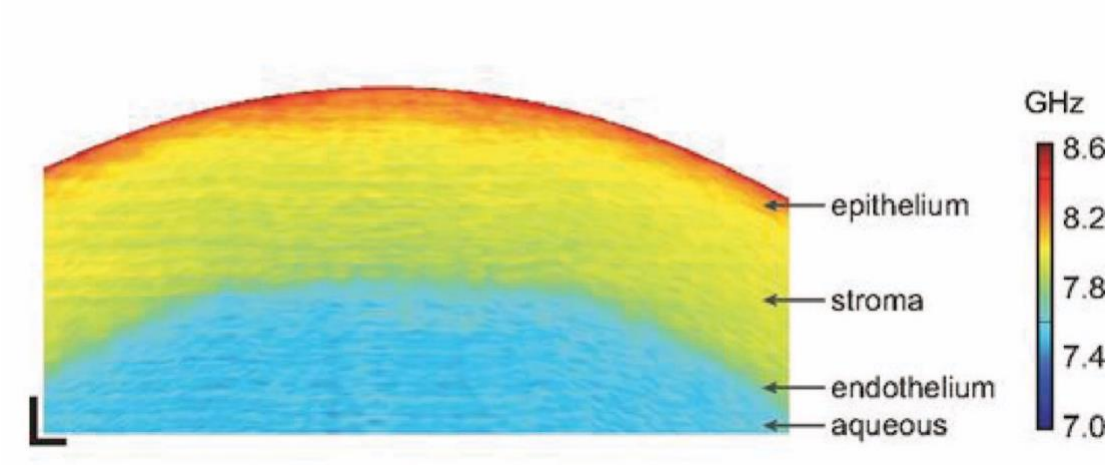

Figure 2.6: Resulting cross-sectional Brillouin map of a bovine cornea (5 x 0.5 mm). Scale bar 200 μm. Adapted with permission.[15]

The corneal stroma exhibited a Brillouin shift gradient from anterior to posterior, with a sharp drop in shift once the aqueous humor was reached beyond the cornea. Since, it was shown the Brillouin shift gradient was in agreement with a depth-dependent mechanical stiffness gradient.[12,13] The gradient was in agreement with collagen density and interwoven organization of collagen fibers, giving the anterior sections of the cornea a greater elastic modulus than the posterior. The measurement also displayed very low lateral variation, which agrees with the transverse mechanical isotropy within the cornea. The technique was also used to measure bovine corneas before and after a cross-linking treatment. The Brillouin measurements showed a significant increase in frequency shift after CXL. More so, the increase in shift was depth-dependent in that the CXL changes were concentrated to the anterior and mid-stroma. The post-CXL, depth-dependent changes observed using Brillouin microscopy were similar to previous findings using low frequency mechanical testing.[95] Soon after, Scarcelli *et.*

al. used Brillouin microscopy to evaluate the effects of porcine cornea cross-linking parameters including soaking / irradiation time and epithelium-off / epithelium-on protocols.[96]

After establishing Brillouin microscopy in porcine and bovine corneas, the technique was used to differentiate between keratoconic and healthy, *ex vivo* human corneas.[11] Here, Brillouin shift was similar between healthy and keratoconic corneas outside of the coned region. However, the shift inside of the cone of a keratoconic cornea was significantly lower than healthy corneas as well as measurements taken outside of the cone of keratoconic samples. The heterogeneity of Brillouin shift found here was in agreement with previous studies which used x-ray scattering techniques to monitor the uneven distribution and organization of lamellae in the cone region of keratoconic corneas.[97] This was the first characterization of mechanical heterogeneity inside a keratotic cornea compared to healthy corneas, and established Brillouin microscopy as a sensitive tool to detect keratoconus in human eyes. In the first *in vivo* trial, Brillouin microscopy detected significant differences within the cone of a keratoconic cornea compared to regions outside the cone and that of healthy patients.[18] Since then, 85 patients (47 healthy, 38 keratoconic) were measured *in vivo* in a study which suggested heterogeneity of Brillouin measurements, more so than thickness or curvature, performs strongly as an early keratoconic marker.[98]

Until now, Brillouin microscopy had been used to measure heterogeneity within a cornea as well as to compare the frequency shift depth profile of virgin and cross-linked

corneas. But notably, no direct correlation existed with low frequency elastic modulus. Here, we unprecedently use the capabilities of Brillouin microscopy to monitor three-dimensional mechanical changes following a variety of up-and-coming cross-linking procedures. We became the first to spatially characterize the stiffening effects of the cornea post accelerated and localized cross-linking by measuring frequency shift in both the lateral and radial directions. Additionally, until now, Brillouin microscopy had been used to measure changes in a single direction, perpendicular to the corneal fibers. However, corneal mechanical properties are largely dictated by the specific organization of the underlying collagen matrix. Here, we demonstrated the ability to detect corneal mechanical anisotropy with Brillouin microscopy. Therefore, our results promote Brillouin microscopy as a modality to fully characterize the relationship of corneal collagen organization and mechanical properties.

2.8 Brillouin-derived Modulus Versus Low Frequency Modulus

The longitudinal modulus measured via Brillouin microscopy is fundamentally different than the standard elastic modulus measured by gold-standard tensile or compression modalities. The longitudinal modulus measures the ratio of an applied uniaxial stress to the material strain in a confined displacement along the longitudinal direction. The cornea, as many biological tissue samples, has high Poisson Ratio as it is nearly incompressible. For an incompressible material, the longitudinal modulus becomes similar to the bulk modulus. Additionally, mechanical measurements of viscoelastic material such as biological tissue are highly contingent on the probing frequency, showing higher modulus with higher frequency.[99] This is due to much

higher probing frequencies outpacing the slower relaxation processes of the viscoelastic sample. The frequency used to measure the longitudinal modulus via Brillouin microscopy is very high (GHz) compared to the quasi-static measurements of elastic modulus. Therefore, due to both the incompressibility and slow relaxation time inherent to biological samples, the Brillouin-derived longitudinal modulus (GPa) is generally orders of magnitude different than traditional elastic modulus (kPa).

While the modulus measured via Brillouin microscopy is different than the traditional elastic modulus, similar underlying properties are responsible for a correlation between the two measurements. A log-log linear fit between Brillouin modulus and low-frequency elastic modulus was first found in tissue samples of porcine ocular lenses,[33] and was later confirmed for other biological material.[100,101] These correlations are consistent with a power-law relationship between the mechanical modulus of soft materials and frequency: $G' = G_0(\omega/\phi_0)^a$ where ω is the frequency and ϕ_0 is the scale factor for frequency.[102] Substituting Brillouin modulus into the equation for quasi-static modulus, we find: $M' = M_0(\omega/\phi_0)^b$. Combining these equations, a log-log relationship has been shown between longitudinal (Brillouin) and elastic modulus. The linear relationship was found as $\log(M') = a * \log(G') + b$ where M' is the Brillouin modulus, G' is the static modulus, and a and b are specific fitting parameters of the sample. Therefore, the relationship between Brillouin measurements and elastic modulus varies based on material, and sample-dependent correlations between Brillouin and elastic modulus have been found in corneas,[101] lenses,[33] polymers,[100] and cells.[100]

The varying, sample-dependent correlations of Brillouin and elastic modulus highlight the rudimentary understandings of the measurements. The moduli are the result of numerous underlying parameters, for example, the water content and solid matrix of the sample. However, it has been raised that these varying correlations are the result of water content, not stiffness, dominating Brillouin modulus measurements of a hydrated material.[103] In highly hydrated hydrogels (92-98.5%) with an elastic modulus between 5-30 kPa, Brillouin modulus appeared insensitive to elastic modulus after accounting for water content. Even within the cornea, the strong role of hydration on Brillouin measurements was previously shown.[104] Therefore, we set out to determine if Brillouin measurements are at all sensitive to hydration-independent components. Here, we demonstrated the ability to detect corneal mechanical anisotropy, a purely solid mechanical component, with Brillouin microscopy through a wide range of water content (72-96%). Nonetheless, detecting mechanical anisotropy demonstrated the presence of a mechanical component within the Brillouin frequency shift, which was independent of hydration, reiterating the ability to detect stiffness measurements.

Once shown that Brillouin measurements depend on both hydration and solid matrix, we better understand the log-log relationship between Brillouin and elastic modulus we and others have observed. Namely, Brillouin and elastic modulus depend on similar underlying parameters when measuring the cornea. However, as evidence by the sample-dependent correlations, the magnitude in which Brillouin and elastic modulus are dependent on these parameters differ. Because of this distinction, a single Brillouin

frequency shift cannot be accurately and universally correlated to the elastic modulus without controlling for or measuring these parameters. Here, we address this shortcoming by studying the underlying parameters of both frequency shift and elastic modulus. We quantifiably define Brillouin frequency shift and elastic modulus in terms of hydration and solid matrix. Doing so increased the overall understanding of the two moduli, including quantifying the sensitivity of each parameter and allowing for more comprehensive interpretations of Brillouin frequency shift. Based on these relationships, we then became the first to define a universal quantified relationship between Brillouin and elastic modulus within the cornea.

CHAPTER 3: MECHANICAL OUTCOME OF ACCELERATED CORNEAL CROSS-LINKING EVALUATED IN THREE DIMENSIONS*

3.1 Introduction

Clinically observed alterations in corneal morphology, a distinguishing characteristic of ectasia, are believed to be the consequence of a non-uniform decrease in stiffness of the corneal stroma.[16,18,105] To combat ectasia, the US Food and Drug Administration has recently approved corneal collagen cross-linking (CXL) to increase the overall stiffness of the cornea. The accepted CXL procedure involves the debridement of the corneal epithelium followed by a 30-minute application of riboflavin solution (0.1% riboflavin, 20% dextran) and an additional 30-minutes of UV-A exposure (3 mW/cm^2; 5.4 J/cm^2).

While effective in stiffening the cornea, the procedure is notoriously extensive and uncomfortable. Recently, a great deal of effort has focused on decreasing the overall treatment time of the CXL procedure. It was proposed that treatment time could be shortened by increasing the radiation intensity, as biological effects should only depend on the total energy dose.[46,47] While protocols featuring intensities up to 50 mW/cm^2 for under 2 minutes of exposure time were suggested,[47] evidence is not conclusive in supporting accelerated cross-linking for clinical settings. Wernli *et al.* reported a

* This work was part of a peer reviewed publication: *Webb et. al., JCRS 43, 2017.*

dramatic reduction in CXL-stiffening when the procedure was performed above a 45 mW/cm^2 intensity.[48] Hammer *et al.* showed a decrease in CXL effectiveness when comparing the standard protocol to that of just a 9 mW/cm^2 radiation intensity.[106] Previous mechanical studies observed the stiffness changes as a function of irradiance regime without spatial resolution.[48,106] To assess the spatially-varying effects of accelerated CXL (A-CXL), indirect techniques have been used such as fluorescence imaging to assess riboflavin penetration or Optical Coherence Tomography to quantify the depth location of refractive index changes within the stroma (i.e. the demarcation line).[47,107,108] Here, we used recently-developed Brillouin microscopy, which can directly assess corneal mechanics with three-dimensional resolution, to observe the depth-dependence of stiffening following accelerated CXL protocols.

3.2 Methods

3.2.1 Corneal Collagen Cross-linking (CXL)

Fresh porcine eyes were obtained from a local slaughterhouse (Frederick, Maryland). For all eyes, the epithelium was carefully removed by scraping with a razor blade. The eyes were then dissected in order to punch two 5 mm corneal disc samples (Integra Miltex ® Disposable Biopsy Punch). Both disc samples were treated with one drop of 0.1% riboflavin/20% Dextran solution every 3 minutes for 30 minutes. After undergoing identical procedures, one of the two samples was set aside as the control while the other sample was exposed to UV radiation. 1 drop of riboflavin was applied to the exposed and control corneas every 5 minutes during radiation to maintain identical hydration. In all experimental settings, a constant UV-A energy of 5.4 J/cm^2

was provided by a high-power UV Curing LED System (Thorlabs, Newton, NJ). We performed four treatment regimens, featuring 3 (n = 4), 9 (n = 6), 34 (n = 6), and 50 (n = 6) mW/cm^2 radiation intensity at 30, 10, 2.65, and 1.80 minutes of illumination time respectively, as summarized in **Table 3.1**.

Table 3.1: Corneal cross-linking treatment regimen by group.

Group	Eyes	Irradiation Energy (J/cm^2)	Irradiation Intensity (mW/cm^2)	Irradiation Time (min.)
1	4	5.4	3	30.00
2	6	5.4	9	10.00
3	6	5.4	34	2.65
4	6	5.4	50	1.80

3.2.2 Brillouin Microscopy

Following the CXL procedure, both the control and cross-linked corneal discs were imaged via Brillouin microscopy with setup and procedures described previously in literature[94] as well as the *Background* (*Chapter 2.6*). Briefly, the confocal Brillouin microscope utilized a 532 nm laser with an optical power of 10 mW. Light was focused into the sample by a 20x objective lens with numerical aperture of 0.4 (Olympus) with transverse resolution of ~1 μm and depth resolution of ~4 μm. The scattered light, collected through the same objective, was coupled into a single mode fiber and delivered to a two-stage VIPA spectrometer featuring an EMCCD camera (Andor, IXon Du-897). Each Brillouin spectrum was acquired in 0.2 seconds. To quantify the Brillouin shift at each sample location, raw spectra from the camera were fitted using

a Lorentzian function and calibrated using the known frequency shifts of water and glass.

From the Brillouin frequency shift, the local mechanical properties of the cornea can be estimated using *Equation 2.1*. The spatially varying ratio of ρ/n^2 was approximated to the constant value of 0.57 g/cm^3 based on literature values[15,93]; we estimate this to introduce a 0.3% uncertainty throughout the cornea.

3.2.3 Brillouin Frequency Shift Image Analysis

The corneal samples were set next to each other on the Brillouin microscope and imaged within the same acquisition run. Therefore, each scan imaged the frequency shift of both the control and cross-linked sample as a function of depth. For each scan, a depth cross-section (XZ) was collected, producing a 1000 μm (lateral) x 1400 μm (axial) image of Brillouin shift. A central sliver of each corneal cross-section was chosen for consistent post-processing analysis. In addition to the entire cornea sample, the cross-sections were divided into three equal segments (anterior, central, and posterior) for depth analysis. For such analysis, the depth of cornea (d) was normalized for each set of corneal samples in order to compare the Brillouin modulus of each sample in the anterior ($0 < d \leq 0.33$), central ($0.33 < d \leq 0.66$), and posterior ($0.66 < d \leq 1$).

3.2.4 Compressive Biomechanical Testing

All samples were measured with compressive mechanical testing immediately after Brillouin imaging using a home-built compressive stress-strain instrument. The instrument consisted of a metallic baseplate, topped with finely gritted sandpaper to prevent unwanted slippage and a downward-moving plunger containing a force-measuring loading cell (Futek, Irving, CA) which is controlled via a motorized translational stage (Zaber, Vancouver, BC). Prior to every sample, the plunger was systematically moved downward until a reaction force from the baseplate was detected. The recorded plunger position was then recorded and later used to calculate the total thickness of the sample.

The corneal sample was placed on the bottom plate of the instrument and the plunger compressed the sample at a constant downward rate of 10 μm/s. Using a custom designed LabView software program (National Instruments, Austin, TX), the increasing compression force from the plunger and the corresponding material displacement were measured to produce the stress-strain curve of the material. The plunger position at which a reaction force was first sensed was noted in conjunction with the previously recorded base-plate position to accurately quantify the thickness of each sample. To obtain the elastic modulus of a sample, we plotted respective Stress (*Force/Area*) vs Strain (*Displacement/Thickness*) graphs and quantified the slope of the linear segment of the curve following the sleek strain. Using the Stress vs Strain curve for each sample, the elastic modulus was reported by fitting the tangent line at 15%

strain. A consistent 15% strain was chosen to observe the linear elastic behavior of the biological tissue as demonstrated by Wernli *et al*.[48]

3.2.5 Statistical Analysis

First, to characterize individual CXL protocols, a paired, two tailed t-test was performed by comparing CXL samples with their respective controls cut from the same eye. Then, to compare different irradiation conditions, the stiffening effects of CXL protocols were analyzed by comparing the percent difference of both Brillouin and elastic moduli. The percent difference for both the Brillouin modulus and elastic modulus were found per eye using the following equation: *Modulus (X) Percent Difference* $= 100(X_{CXL} - X_{Control})/(X_{Control})$. The respective moduli percent differences for the samples in each irradiation group were averaged ± standard error of the mean. A Wilcoxon Rank-Sum Test was used to assess the significance in comparisons between samples and/or corneal sections. P values less than or equal to 0.05 were considered statistically significant.

3.3 Results

3.3.1 Corneal Cross-linking-induced Changes in Elastic Modulus

To assess the stiffening effects of each CXL procedure, the elastic modulus of the CXL samples were compared to their respective controls punched from the same porcine eye. This comparison showed that all CXL protocols produced a statistically significant ($p \leq 0.05$) increase in stiffness compared to non-irradiated control conditions. Then, we compared the mechanical outcome of the varying CXL

procedures by quantifying the percent change in elastic modulus with respect to each control. **Figure 3.2** depicts the average percent change in elastic modulus ± standard error of the mean for the four irradiation conditions. The standard protocol, 3 mW/cm^2 of UV-A power for 30 minutes, was significantly more effective than the 34 ($p \leq 0.05$) and 50 mW/cm^2 ($p \leq 0.01$), the 9 mW/cm^2 condition was statistically significantly higher than the 50 mW/cm^2 ($p \leq 0.01$), and there was no significant difference between the 34 and 50 mW/cm^2 conditions.

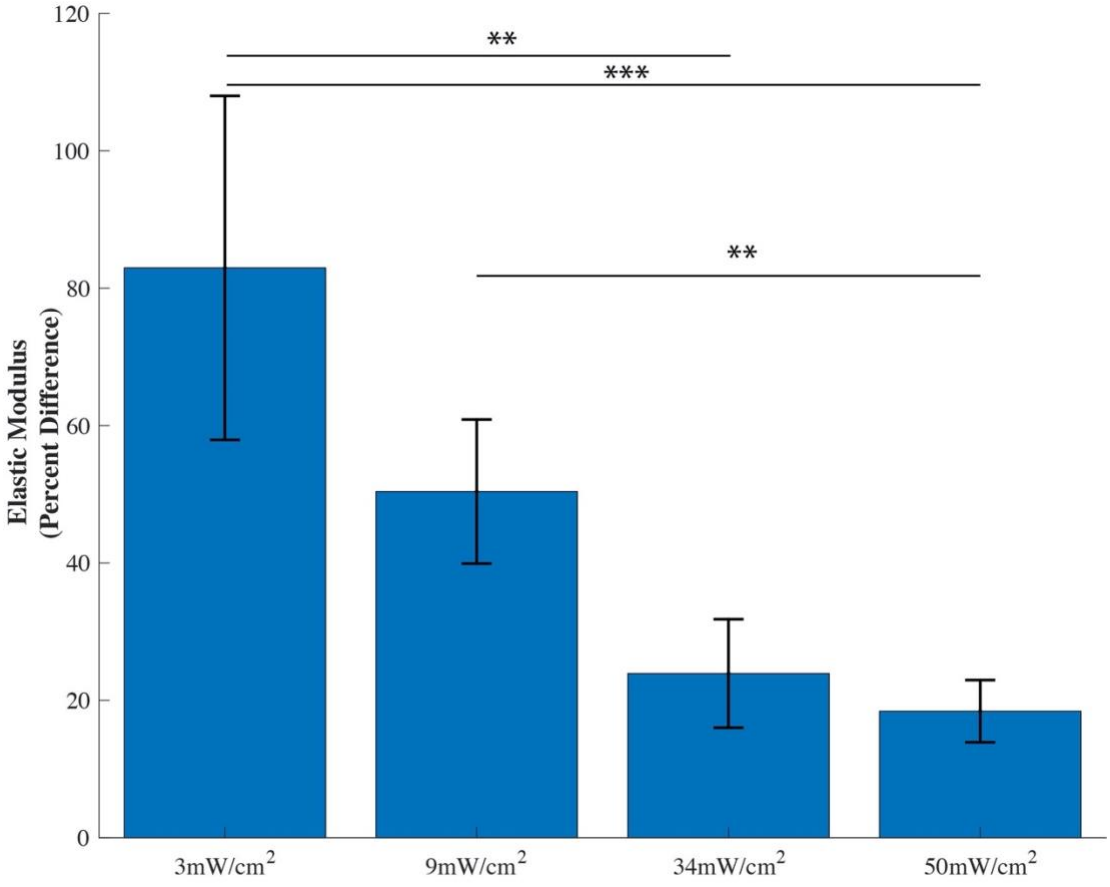

Figure 3.1: Elastic modulus as a function of irradiation condition. The averaged percentage change in elastic modulus for each irradiation condition from 3 to 50 mW/cm2. As the intensity increases, the change in elastic modulus decreases. Error

bars represent the standard error of mean (SEM) for each condition (** = $p \leq 0.01$; *** = $p \leq 0.001$).

3.3.2 Corneal Cross-linking-induced Changes in Brillouin Modulus

To compare with the compressive mechanical test, we calculated the Brillouin modulus from the Brillouin frequency shift and averaged the value over the whole sample. First, as for the traditional modulus analysis, the Brillouin modulus of CXL samples were compared to their respective non-irradiated controls. All CXL protocols produced a statistically significant ($p \leq 0.05$) increase in corneal stiffness compared to their control. **Figure 3.2** shows the stiffness outcome of the CXL protocols as measured by Brillouin microscopy. **Figure 3.2.A** depicts representative cross-sectional Brillouin images of corneas from each irradiation condition with the color encoding the Brillouin frequency shift at each location. We then computed the percent change of Brillouin modulus for each irradiation condition. **Figure 3.2.B** summarizes the stiffening as a function of radiation intensity. The 3 mW/cm^2 CXL condition resulted in higher corneal stiffening than the 9 mW/cm^2 ($p \leq 0.05$), 34mW/cm^2 ($p \leq 0.01$), and 50 mW/cm^2 ($p \leq 0.01$), the 9mW/cm^2 had significantly higher stiffening than the 34mW/cm^2 ($p \leq 0.01$) and 50 mW/cm^2 ($p \leq 0.01$), and the 34 and 50 mW/cm^2 irradiation conditions did not significantly differ in CXL-induced stiffening.

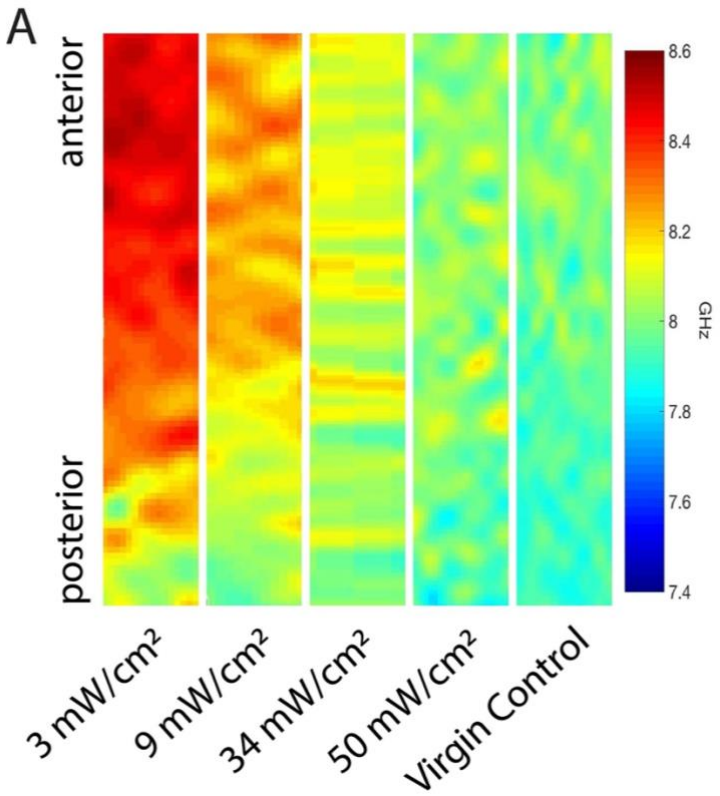
A
anterior
posterior
8.6
8.4
8.2
8
7.8
7.6
7.4
GHz
3 mW/cm²
9 mW/cm²
34 mW/cm²
50 mW/cm²
Virgin Control

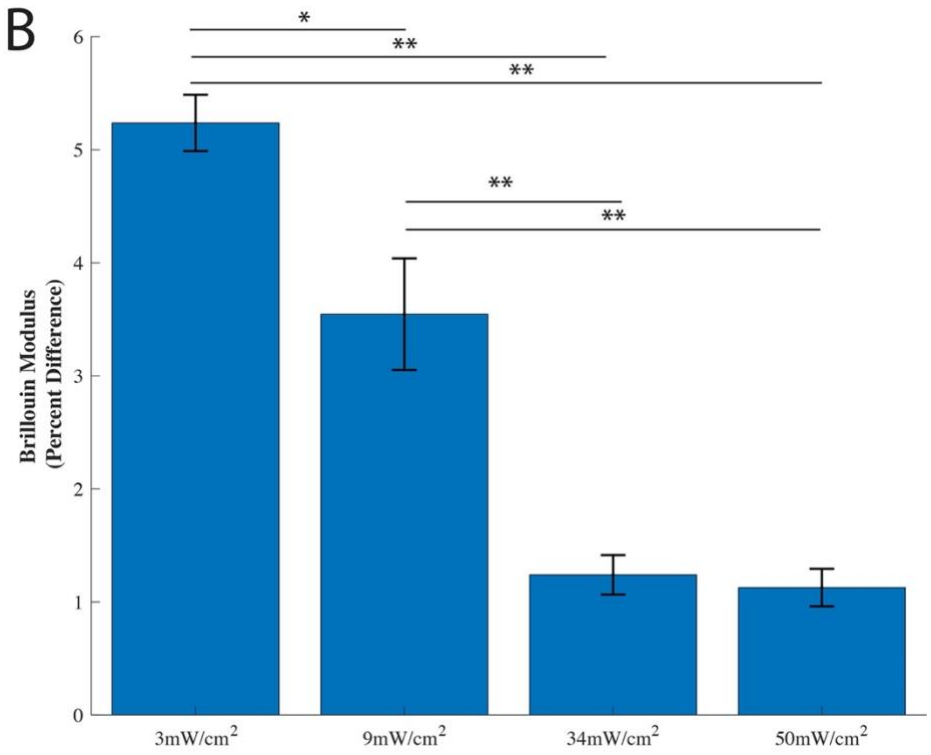
B
Brillouin Modulus
(Percent Difference)
0
1
2
3
4
5
6
*
**
**
**
**
3mW/cm²
9mW/cm²
34mW/cm²
50mW/cm²

Figure 3.2: Brillouin modulus as a function of irradiation condition **A**: Representative image (700 μm x 100 μm) produced with Matlab software (color map: jet) of the Brillouin shifts for each condition. Because of the relationship between shift and Brillouin modulus, a higher Brillouin shift correlates to a higher Brillouin modulus. The corneal slices are positioned anterior up. **B**: The averaged percentage change in Brillouin modulus for each irradiation condition from 3 to 50 mW/cm^2. As the intensity increases, the overall change in Brillouin modulus decreases. Error bars represent the SEM for each condition (* = $p \leq 0.05$; ** = $p \leq 0.01$).

3.3.3 Quantifying the Correlation Between Changes in Elastic and Brillouin Modulus

Figure 3.3 shows the relationship between elastic modulus and the average Brillouin modulus of the cornea sample. Each of the four points in **Figure 3.3** represents the average of all the samples at a given irradiation condition. As radiation intensity decreased, both the elastic modulus percent change and the Brillouin modulus percent change increased at a similar rate. The similar rate of increase resulted in a highly statistically significant linear correlation between the percent change of elastic modulus and the percent change of Brillouin modulus with $R^2=0.985$.

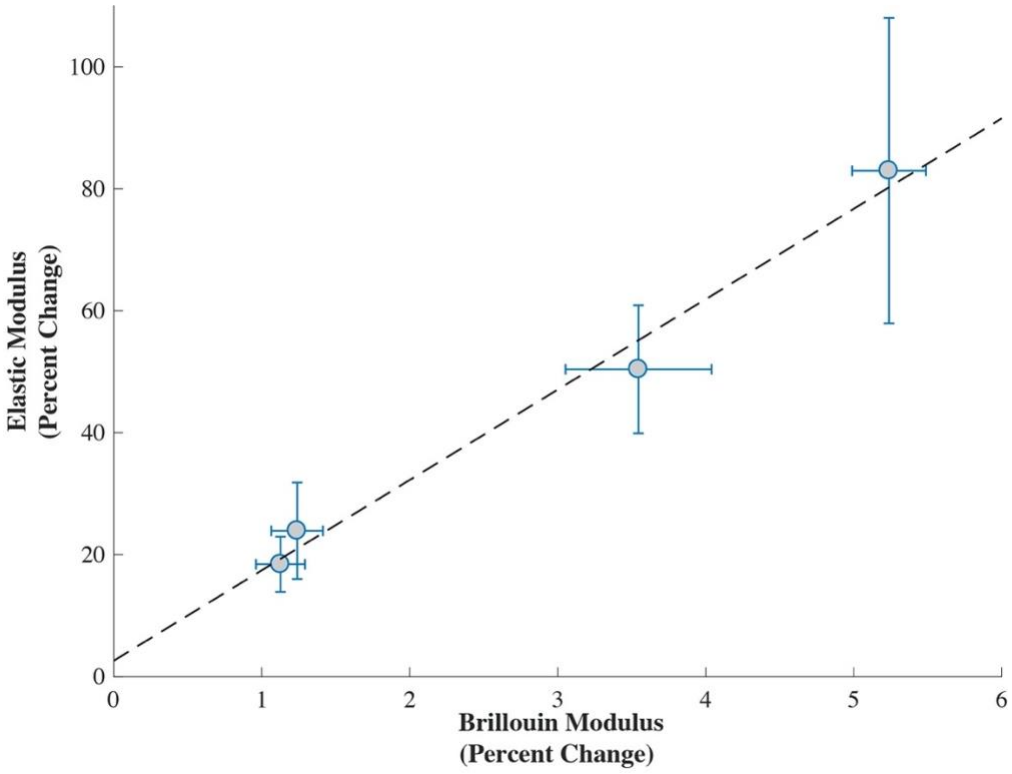

Figure 3.3: Correlation between percentage difference of mechanically-yielded elastic modulus and Brillouin microscopy–derived Brillouin modulus. The correlation yielded a line of best fit of $y = 14.82x + 2.605$ with a correlation coefficient of $R^2 = 0.985$. Error bars represent the SEM for each condition.

3.3.4 Depth-dependent Changes in Brillouin modulus Following Corneal Collagen Cross-linking

Finally, we used Brillouin microscopy to perform a depth-dependent analysis on the corneas. We calculated the percent change in Brillouin modulus in anterior, central and posterior sections of the cornea. **Figure 3.4** shows the percent change in Brillouin modulus for each irradiance condition in the anterior, central, and posterior of the cornea. Comparing the stiffening of the 3 mW/cm^2 and 9 mW/cm^2 conditions, there

was no statistical significance in the anterior section. However, the difference between the two conditions was statistically significant ($p \leq 0.05$) in the central and posterior sections of the corneas. In all sections, the 3 mW/cm^2 produced significantly more stiffening ($p \leq 0.01$) than the 34 and 50 mW/cm^2 conditions. The stiffening from the 9 mW/cm^2 sample significantly differed from that of the 34 mW/cm^2 sample in the anterior ($p \leq 0.01$) and the 50 mW/cm^2 sample in the anterior ($p \leq 0.01$) and central ($p \leq 0.05$). There were no significant differences in stiffening at any section between the two most accelerated conditions.

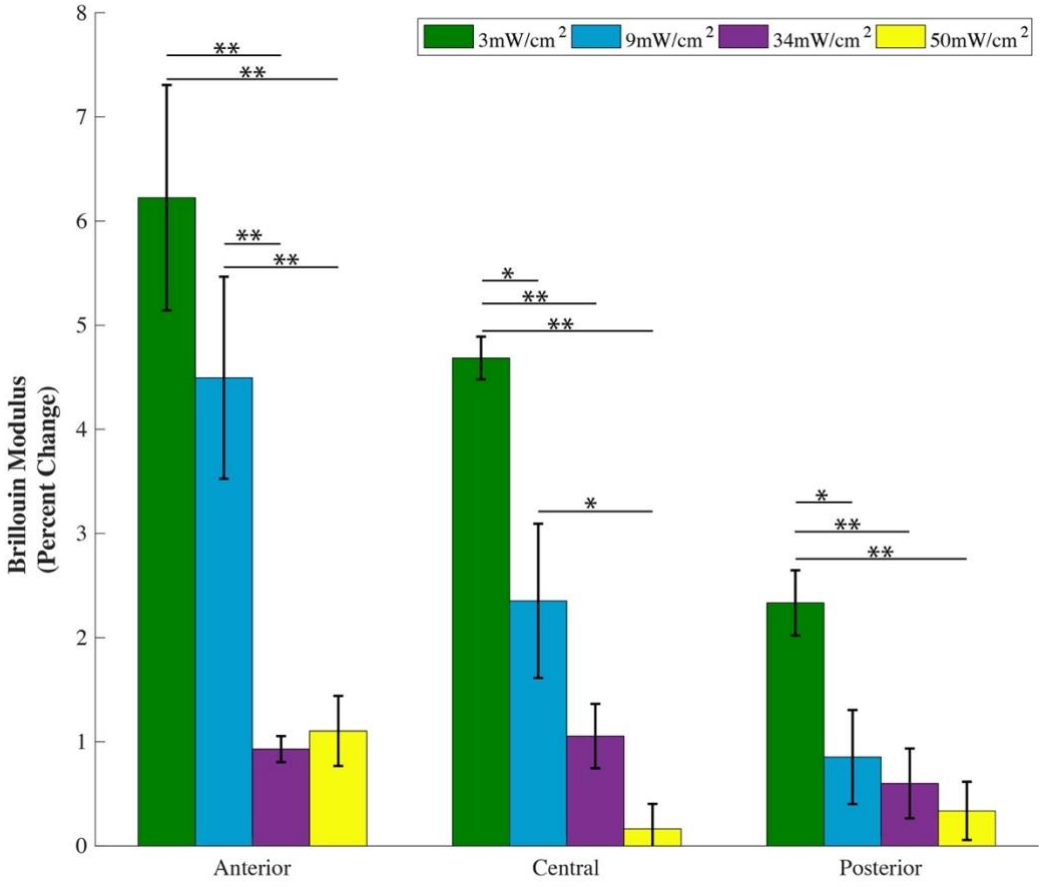

Figure 3.4: Depth-dependent Brillouin modulus as a function of irradiation condition. Brillouin modulus at a constant energy dose of 5.4 J/cm^2 as a function of radiation intensities and exposure times (green) 3 mW/cm^2 for 30.0 minutes, (blue) 9 mW/cm^2

for 10.0 minutes, (purple) 34 mW/cm^2 for 2.65 minutes, and (yellow) 50 mW/cm^2 for 1.80 minutes as well as corneal section (anterior, central, and posterior). Error bars represent the SEM for each condition (* = $p \leq 0.05$; ** = $p \leq 0.01$).

3.4 Discussion

In this study, we evaluated the stiffening effects of accelerated corneal cross-linking protocols. To minimize the control-to-sample variability, two discs were punched from each cornea to act as the non-irradiated control and cross-linked sample respectively. Keeping a constant energy dose of 5.4 J/cm^2, we performed four corneal cross-linking regimens with varying power and exposure time. To first validate our cross-linking procedures, we compared the resulting stiffness of our cross-linked samples to the respective control samples via stress-strain testing and Brillouin modulus derivation. The two techniques consistently showed a significant stiffening effect of CXL for all conditions.

Next, we compared the standard protocol, 3 mW/cm^2 of UV-A radiation intensity for 30 minutes of exposure time, to different accelerated protocols. We first used a commonly accepted compression test to compare the stiffening effects of each regime. The standard CXL protocol, 3mW/cm^2 of UV-A radiation for 30 minutes of exposure time, produced a significantly higher percent difference in elastic modulus than the 34 and 50 mW/cm^2 conditions. The 9 mW/cm^2 condition yielded a significantly higher stiffening effect than the most accelerated protocol. Thus, while the Bunsen-Roscoe law predicts the cross-linking effects should be similar at a constant energy, our

mechanical analysis yielded a radiation intensity/exposure time dependence of stiffening. This is in agreement with previous papers that analyzed accelerated CXL stiffness with compressive mechanical testing. The observed increases in elastic modulus at each irradiance condition, varying from 83% to 18% as a function of radiation power, all fall between the reported values of Hammer *et al.* and Wernli *et al.*[48,106] The consistency between our values and that found in similarly conducted literature furthered validated our results. However, the studies presented notable differences in the trend between irradiance condition and stiffening effect. Hammer *et al.* reported a significant decrease in stiffening when the standard 3 mW/cm^2 irradiation condition was compared to 9 and 18 mW/cm^2 accelerated protocols.[106] Wernli *et al.* reported a statistically significant difference in comparing cross-linked samples to their respective controls up until a maximum radiation intensity of 45 mW/cm^2 for 2 minutes of exposure time. However, unlike our findings and that of Hammer *et al.*, the study demonstrated a relatively constant effect of cross-linking from 3 mW/cm^2 through roughly 45 mW/cm^2 before experiencing a significant decrease in stiffening magnitude.[48] The differences in results could depend on the variability in experimental procedures. For example, Wernli *et al.* kept the corneas immersed in a pool of riboflavin solution for 30 minutes prior to UV-A exposure. Our protocol more closely resembled that of Hammer *et al.* in that riboflavin drops were incrementally applied to the cornea for a total of 30 minutes prior to radiation exposure. Differing from Hammer *et al.*, our protocol used corneal punches rather than the entire globe. This distinction, by minimizing the solution run-off due to a decreased sample curvature, may be responsible for our greater stiffening effects.

The results of the stress-strain testing were also used to validate Brillouin microscopy. We have previously determined a log-log linear correlation between elastic modulus and Brillouin-derived Brillouin modulus.[33] Therefore, our linear correlation between the percent change in elastic modulus and Brillouin modulus agrees with the previously found relationship.

Using Brillouin microscopy, we were able to uniquely expand on our findings as well as those of relevant studies by observing the effects of CXL as a function of depth. This analysis yielded particularly interesting results when comparing the standard protocol (3 mW/cm^2 for 30 minutes) to the slightly accelerated protocol (9mW/cm^2 for 10 minutes). When the entire cornea was analyzed, the standard condition displayed a significantly higher Brillouin modulus than the 9 mW/cm^2 protocol. From depth-dependent analysis, the two treatments did not show statistically significant differences in anterior stroma, but they showed statistically significant differences in the central and posterior portions of the cornea. This suggests the overall difference between the two conditions was primarily due to the distinction in the deeper sections. Our findings on depth-dependent stiffening via CXL are in agreement with those of Aldahlawi *et* al.,[109] who used the resistance to enzymatic degradation properties of cross-linked corneas to test the effective depth of the procedure. The study similarly showed, up until a maximum radiation power of 18 mW/cm^2 for 5 minutes of exposure time, that accelerating the cross-linking procedure has little effect on the anterior of the corneal stroma but reduces the effective depth of CXL.

It has been suggested that oxygen is a key limiting factor in the CXL process, as CXL had no significant stiffening results when conducted in a low-oxygen environment.[110] Specifically, it is hypothesized the cross-linking procedure begins with a Type-II photochemical mechanism in which oxygen, once transformed into the reactive species, is consumed as the predominant reaction drivers and catalyze the covalent bonding of collagen and other matrix proteins in the stroma.[40] Following oxygen depletion and a shift to a direct, oxygen-independent reaction, oxygen is gradually replenished throughout the cornea. At this point, oxygen, again via a Type-II reaction, enhance the cross-linking mechanism.[39] Based on this knowledge, at high radiation intensity, the rate of oxygen depletion could exceed the rate of oxygen replenishment via diffusion. In particular, the available oxygen concentration is a depth-dependent quantity as it is increasingly difficult for the oxygen to diffuse deeper into the cornea. Therefore, the difference between oxygen depletion and replenishment correlates to both depth and radiation intensity. As a result, when comparing 3 mW/cm^2 and 9 mW/cm^2 conditions for example, it is expected that the anterior portions of the corneas would have similar results while larger stiffening differences should be observed deeper into the corneas. This phenomenon would explain the lower stiffening we observed at the deeper sections of the accelerated cross-linked corneas as the Type-II reaction, requiring oxygen replenishment, is unavailable. However, this effect is primarily seen in the 9 mW/cm^2 condition as the 34 and 50 mW/cm^2 conditions significantly lack stiffening at all three sections of the stroma when compared to the standard protocol. The reported anterior lack in stiffening of the most accelerated

protocols may be an effect of the measurement technique used. Brittingham *et al*., when comparing the standard 3 mW/cm^2 and 9 mW/cm^2 conditions, demonstrated a significant decrease in depth of the demarcation line following accelerated protocols.[111] Therefore, it is possible that for our highest accelerated conditions, the most effected depth of the CXL is too shallow to significantly detect using our Brillouin microscopy parameters. However, it is worth noting that a similar threshold of stiffening efficiency was also observed from Wernli *et al*.[48] It is possible that when the procedure is performed at such a rapid rate, oxygen is unable to diffuse back into the cornea to a significant depth. Past a threshold of a sufficiently oxygenated stroma, we would expect to observe very little stiffening effects of CXL due to the low oxygen environment as reported by Richoz *et al.*[110]

3.5 Conclusion

Corneal collagen cross-linking is a clinically performed procedure used to increase the stiffness of the cornea in order to halt the progression of ectasia. Due to the time-consuming nature of the procedure, accelerated techniques have been explored without compromising total energy dosage. We first confirmed the sub-optimal effects of accelerated cross-linking compared to the standard 3 mW/cm^2 condition. We then, by employing the depth-dependent analysis of Brillouin microscopy, performed the first three-dimensional, mechanical characterization of accelerated CXL. The overall lack of stiffening of an accelerated protocol can primarily be attributed to the sub-optimal stiffening in the posterior sections of the cornea. Now better understood, the lack of

stiffening should be highly considered when clinically performing accelerated CXL procedures to prevent ectasia.

CHAPTER 4: BIOMEHANICAL IMPACT OF LOCALIZED CORNEAL CROSS-LINKING BEYOND THE IRRADIATED TREATMENT AREA*

4.1 Introduction

Corneal ectasia is characterized by alterations in corneal morphology due to a non-uniform decrease in the stiffness of the cornea.[18,26,112] However, the US Food and Drug Administration-accepted cross-linking procedure to halt cornea ectasia calls for soaking the cornea with a photosensitizer (riboflavin) followed by uniform, global UV-A exposure.[42,110,113] The procedure leads to the creation of additional chemical bonds throughout the corneal tissue collagen, thereby, increasing overall corneal strength.[20]

Localized CXL (L-CXL) has recently been proposed to address the spatially dependent characteristics of ectasia.[50–52] By limiting the irradiated area, the risk of complication and infection is expected to diminish due to less epithelial removal,[114] potential haze, and stromal damage.[50] Most importantly, because the stiffening is concentrated in the mechanically compromised area of the cornea, greater local topographical flattening is expected.[49] However, the biomechanical properties of the cornea after localized CXL procedures have not yet been evaluated due to the lack of characterization methods capable of measuring corneal mechanical properties with three-dimensional resolution.

* This work was part of a peer reviewed publication: *Webb et. al., JRS 35, 2019.*

The purpose of this study was to noninvasively measure and characterize the spatial distribution of the modulus of the cornea following localized CXL using Brillouin microscopy and determine the magnitude and extent of the stiffening effect from CXL beyond the irradiated (UV-A exposed) region of the cornea.

4.2 Methods

4.2.1 Corneal Cross-linking-induced Changes in Brillouin Modulus

Freshly enucleated porcine eyes were obtained from a local slaughterhouse. They were kept in ice during the transportation until the start of the experiment. The experiment was completed within 8 hours after the sacrifice of the porcine. All corneas with intact epithelium were visually inspected to avoid using damaged or unclear tissue prior to any experimentation. Localized CXL was performed *ex vivo* by restricting illumination during CXL to half the porcine cornea using a customized mask. Localized CXL was performed using a traditional UV protocol and a protocol using blue light.

4.2.2 UV-A Localized Corneal Cross-linking (UV L-CXL)

To illustrate the issue, we performed UV localized CXL experiment on one porcine eye after epithelial debridement followed by the administration of one drop of 0.1% riboflavin solution every 3 minutes for 20 minutes. Next, a constant UV-A (365 nm) power of 9 mW/cm^2 was applied via a high-power UV Curing LED System (Thorlabs, Newton, NJ) for 10 minutes.[48,106] As the primary purpose of the UV light experiment was to illustrate the spatial variation of CXL procedure and to minimize any potential variation in tissue hydration, an accelerated protocol was chosen and implemented.

Half of the cornea was blocked from UV using a homemade, sharp-edged mask placed directly above the anterior of the cornea. During UV exposure, one drop of riboflavin solution was administered to the cornea at 5-minute intervals. The UV L-CXL methods are outlined in **Table 4**. Using Brillouin microscopy, we analyzed the biomechanical properties of the sample in three dimension and calculated the transition zone.

4.2.3 Blue light / Localized Corneal Collagen Cross-linking (Blue light CXL / L-CXL)

Because the UV-A lamp is an extended source emitting incoherent light, it was reasonable to assume that radiation could not be confined to sharp transitions; thus, we utilized a blue laser and validated a CXL protocol using blue light.

For the blue light localized CXL experiment, 10 porcine eyes had epithelial debridement followed by the administration of one drop of 0.1% riboflavin solution every 3 minutes for 20 minutes. Similar to previous experiments performing blue light CXL,[15,115] the cornea was then exposed to 15 mW/cm^2 blue light (447 nm) radiation for 20 minutes via a blue diode laser light source (Opto Engine LLC, Salt Lake City, UT). During blue light exposure, one drop of riboflavin solution was applied at 5-minute intervals. In a similar manner to UV L-CXL, the blue light procedure was localized using the blocking mask. The Blue Light L-CXL methods are outlined in **Table 4.1**.

Using Brillouin microscopy, we analyzed the biomechanical properties of each sample and calculated each transition zone. We aligned the transition zones of the corneas at 50% respective normalized stiffness and averaged across the depth axis.

Table 4.1: Corneal cross-linking methods.

Parameters	Variable (UVA Light)	Variable (Blue Light)
Treatment target	Ectasia	Ectasia
Fluence (total) (J/cm^2)	5.4	18
Soak time and interval (minutes)	20 (q3)	20 (q3)
Intensity (mW)	9	15
Treatment time (minutes)	10	20
Epithelium status	Off	Off
Chromophore	Riboflavin	Riboflavin
Chromophore carrier	Dextran	Dextran
Chromophore osmolarity	Iso-osmolar	Iso-osmolar
Chromophore concentration	0.1%	0.1%
Light source	UVA (365nm) UV Curing LED System (Thorlabs, Newton, NJ)	Blue (447nm) Diode Laser (Opto Engine LLC, Salt Lake City, UT)
Irradiation mode (interval)	Continuous	Continuous
Protocol modifications	Blocking mask	Blue laser light, Blocking mask
Protocol abbreviation in manuscript	UV L-CXL (Localized)	Blue Light L-CXL (Localized)

4.2.4 Brillouin Microscopy

A confocal Brillouin microscope was utilized with similar configuration of previous studies[94] as well as outlined in *Background* (*Chapter 2.6*) but at a different incident wavelength. Briefly, a 660 nm laser with an optical power of 15 mW was focused into the sample by a 40x objective lens with numerical aperture of 0.6 (Olympus), a transverse resolution of ~1 μm, and depth resolution of ~2 μm. The scattered light, collected through the same objective, was coupled into a single mode fiber and

delivered to a two-stage virtually imaged-phase-array (VIPA) spectrometer featuring an electron multiplying charge coupled device (EMCCD) camera (Andor, IXon Du-897). Each Brillouin spectrum was acquired in 0.15 seconds. To quantify the Brillouin shift at each sample location, raw spectra from the camera were fitted using a Lorentzian function and calibrated using the known frequency shifts of water and glass.

From the Brillouin frequency shift, the local mechanical properties of the cornea can be estimated using *Equation 2.1*. The spatially varying ratio of ρ/n^2 was approximated to the constant value of 0.57 g/cm^3 based on literature values[15,93]; we estimate this to introduce a 0.3% uncertainty throughout the cornea. Previously, we have validated the strong relationship (R > 0.9) between Brillouin-derived modulus and the elastic modulus found via gold-standard stress-strain compression tests on porcine corneas.[101]

4.2.5 Calculation of Transition Zones

The primary metric quantified in this study was the transition zone between the fully irradiated and non-irradiated corneal areas. A sharp-edged mask was used throughout the protocols to define the two sections. While several different parameters were evaluated, including light intensity and Brillouin modulus, a common computation of the transition zone was conducted on each respective image.

To calculate the transition zone, the light intensity was averaged along the perpendicular axis normal to the transition edge and normalized using the equation:

$$[I_n] = \frac{([I] - [I_{min}])}{([I_{max}] - [I_{min}])} \quad (Eqn.\ 4.1)$$

where I_n is the normalized intensity, I is the average measured intensity, and I_{min} and I_{max} are the intensities at the lowest and greatest plateau respectively. We calculated the transition zone as the distance between 10% and 90% of the maximum value. Only the anterior third of the cornea was used for analysis of the transition zone of CXL procedures as that was the region primarily affected by localized cross-linking.[101,116] For Brillouin maps, Brillouin modulus was used in place of light intensity throughout the calculation of transition zone.

4.2.6 Biomechanical Testing

To validate the blue-light protocol, we compared the elastic modulus of control and blue light-cross-linked buttons punched from the same respective cornea. 8 porcine corneas were dissected. Two 5 mm central corneal disc samples were created (Integra Miltex Disposable Biopsy Punch) from each cornea. Both disc samples were treated with one drop of 0.1% riboflavin solution every 3 minutes for 20 minutes. One of the two samples was set aside as the control while the other sample was fully exposed to 15 mW/cm^2 blue light radiation for 20 minutes. During the irradiation process, hydration of both the control and exposed discs was maintained via the application of 1 drop of riboflavin solution at 5-minute intervals.

Next, mechanical properties of each sample were tested using a Microsquisher compressive stress-strain instrument (model: MT G2) and the associated Squisherjoy

software (Cellscale, Waterloo, Ontario). The instrument directly compressed the corneal samples using a 6 mm x 6 mm plate attached to a 0.5588 mm diameter microbeam. To obtain the elastic modulus of a sample, the Stress (*Force/Area*) vs Strain (*Displacement/Thickness*) curve was obtained and the slope of the linear segment of the curve following the sleek strain was quantified. For each sample, we reported the modulus at 1.5-4.5% strain.

4.2.7 Measurement of Light Propagation from Blue Light L-CXL Setup

In order to isolate the transition zone generated by the blue light source alone, using the Blue Light L-CXL setup, we replaced the corneal sample with a complementary metal–oxide–semiconductor (CMOS) camera (Mightex Systems, Toronto, Ontario). The camera has a 1280 x 1024 monochrome resolution with 5.2 μm per pixel and 50 ms exposure time. To quantify the light exposure at the varying depths of the cornea, we placed the camera at a distance 0, 500, and 1000 μm from the mask; 0 μm to represent the anterior surface and 1000 μm to represent the posterior edge at the estimated maximum porcine corneal thickness. At the three distances, respective images were captured, and the light transition zone was calculated.

4.2.8 Measurement of Light Scattering Within the Cornea

Light scattering within the cornea could result in riboflavin outside of the directly irradiated area becoming excited, thereby, cross-linking surrounding cornea that is otherwise covered by the mask. To measure light scattering throughout the L-CXL

procedure, we mimicked the Blue Light L-CXL setup at three conditions. First, we replaced the cornea with a CMOS camera at a distance 3 mm from the mask. Respective images (n = 7) were taken, and transition zones calculated based on measured light intensity. Following each image capture, we placed a 5 mm punched porcine cornea disc on top of the CMOS camera. Under the same conditions, images were captured and analyzed.

Finally, we subjected punched discs (n = 4) to one drop 0.1% riboflavin solution every 3 minutes for 20 minutes. We then placed the cornea on the camera, captured respective images, and similarly analyzed the riboflavin/cornea transition zone.

4.2.9 Statistical Analysis

For gold-standard biomechanical analysis, the elastic modulus of samples extracted from the same cornea were calculated as previously indicated and compared using a Wilcoxon Signed Rank Test. To compare the corneal scattering-induced transition zones to their respective controls, we performed a Wilcoxon Signed Rank test. To compare the scattering-induced transition zones of riboflavin-soaked corneas to virgin corneas and cornea-omitted controls, a Mann-Whitney U test was performed.

4.3 Results

4.3.1 Cross-linking Transition Zone Measured via Brillouin Microscopy

Figure 4.1.A shows the Brillouin map of a UV-induced, locally cross-linked cornea. Brillouin microscopy revealed two distinct lateral regions within the cornea that extend the entire depth: a fully cross-linked section and a non-cross-linked section. The two regions primarily varied in anterior stiffness. Importantly, these sections were separated by a remarkably broad transition zone. **Figure 4.1.B**, a transverse profile of the normalized Brillouin shift, shows an evident transition zone between the cross-linked and non-cross-linked sections.

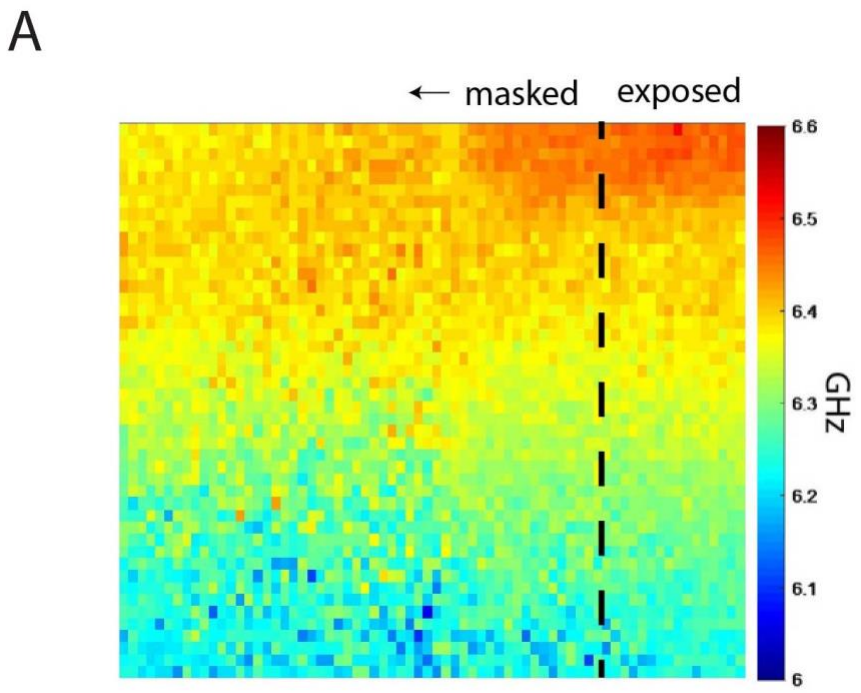

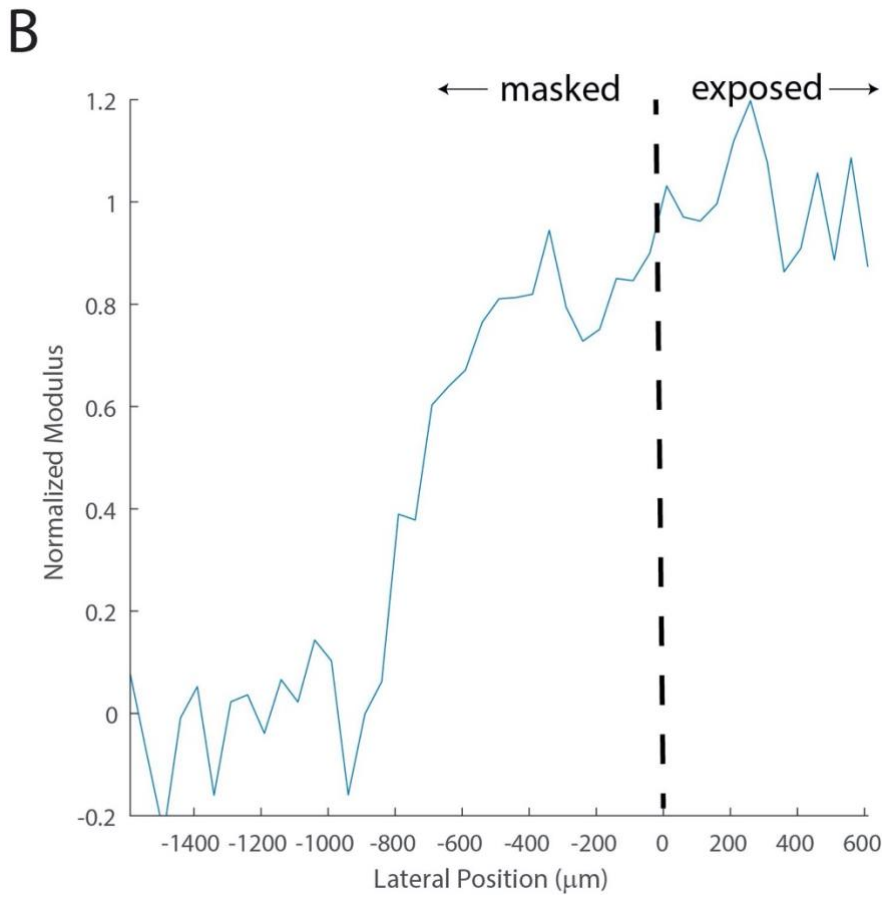

Figure 4.1: Brillouin microscopy detection of a transition zone between masked and exposed sections of the cornea **A:** Representative Brillouin map (4000 μm x 700 μm) produced with MATLAB software (color map: jet) depicting the Brillouin shifts of a UV-induced, locally crosslinked porcine cornea positioned anterior up. The dotted line illustrates the edge of the UV blocking mask, differentiating the blocked and exposed sections of the cornea. A higher Brillouin shift correlates to a higher Brillouin modulus. **B**: The normalized Brillouin shift versus lateral position. Similar to 1a, the dotted line illustrates the edge of the UV blocking mask. The transition zone was taken as 10-90% normalized shift.

4.3.2 Blue Light Cross-linking Procedures Stiffer Cornea

Figure 4.2 shows the cross-linking capabilities of the blue light protocol. Specifically, **Figure 4.2.A** displays representative Brillouin maps of control and blue light-cross-linked corneas. To validate the stiffening effects of the blue-light protocol, we compared the Microsquisher®-derived elastic modulus of control and blue light-cross-linked buttons punched from the same respective cornea. As summarized in **Figure 4.2.B**, the blue light-cross-linked samples showed significantly higher elastic modulus ($p \leq 0.05$) than the untreated controls, yielding a modulus of 3972.2 ± 1048 Pa vs 1419.7 ± 312.8 Pa respectively (180% the elastic modulus of their respective controls).

A

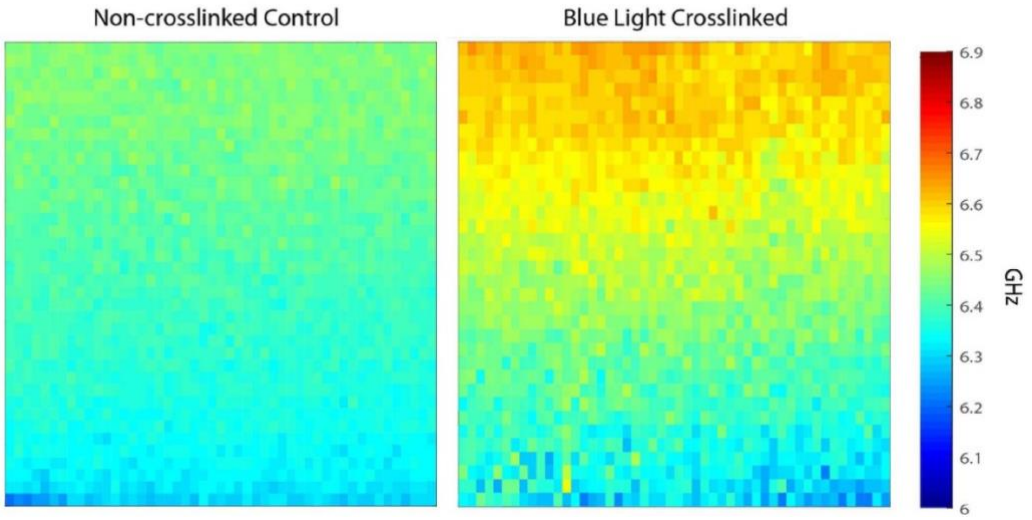
Non-crosslinked Control
Blue Light Crosslinked
6.9
6.8
6.7
6.6
6.5
6.4
6.3
6.2
6.1
6
GHz

B

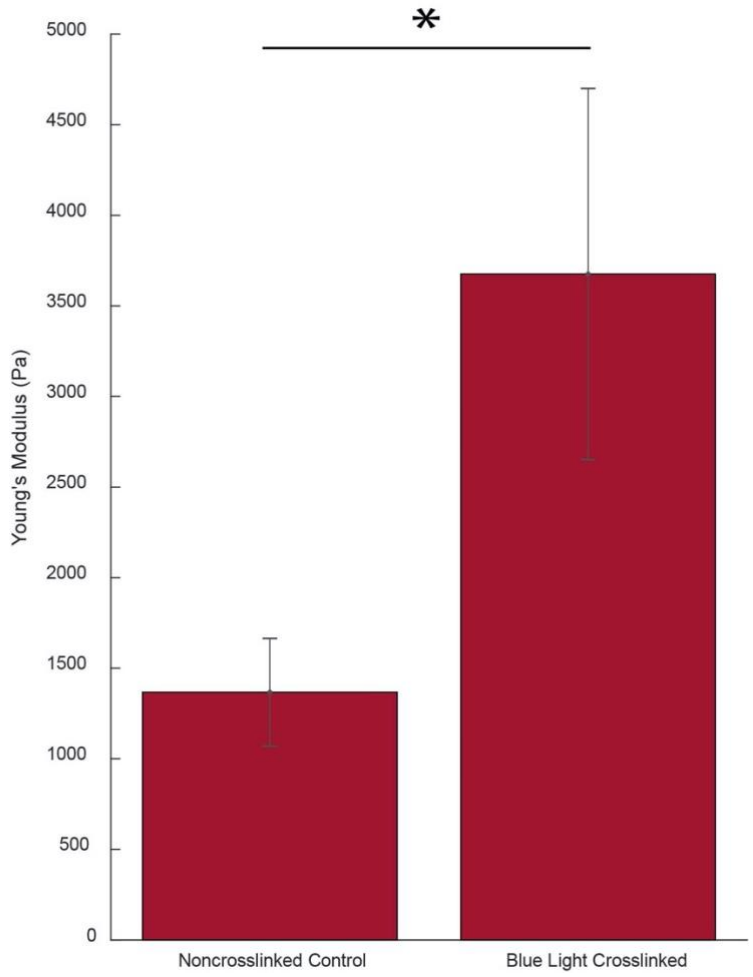
*
5000
4500
4000
3500
3000
2500
2000
1500
1000
500
0
Young's Modulus (Pa)
Noncrosslinked Control
Blue Light Crosslinked

Figure 4.2: Validation of blue light cornea cross-linking **A**: Representative Brillouin maps (4000 μm x 700 μm) produced with MATLAB software (color map: jet) of both a virgin (control) as well as a blue light-crosslinked porcine cornea positioned anterior up. The crosslinked cornea was exposed to 15 mW/cm^2 blue light for 20 minutes. **B**: Bar graph comparing the elasticity, found via Microsquisher® compression, of control corneal punches and crosslinked punches. Error bars represent SEM for each condition (* = $p < 0.05$).

4.3.3 Quantifying the Transition Zone Produced During Localized CXL Procedure

Figure 4.3 quantifies the transition zone induced strictly from the blue light L-CXL optical setup. The transition zone broadened as distance between camera and mask increased from 0 to 500 and 1000 μm, mimicking the anterior, central, and posterior sections of the porcine cornea, respectively.

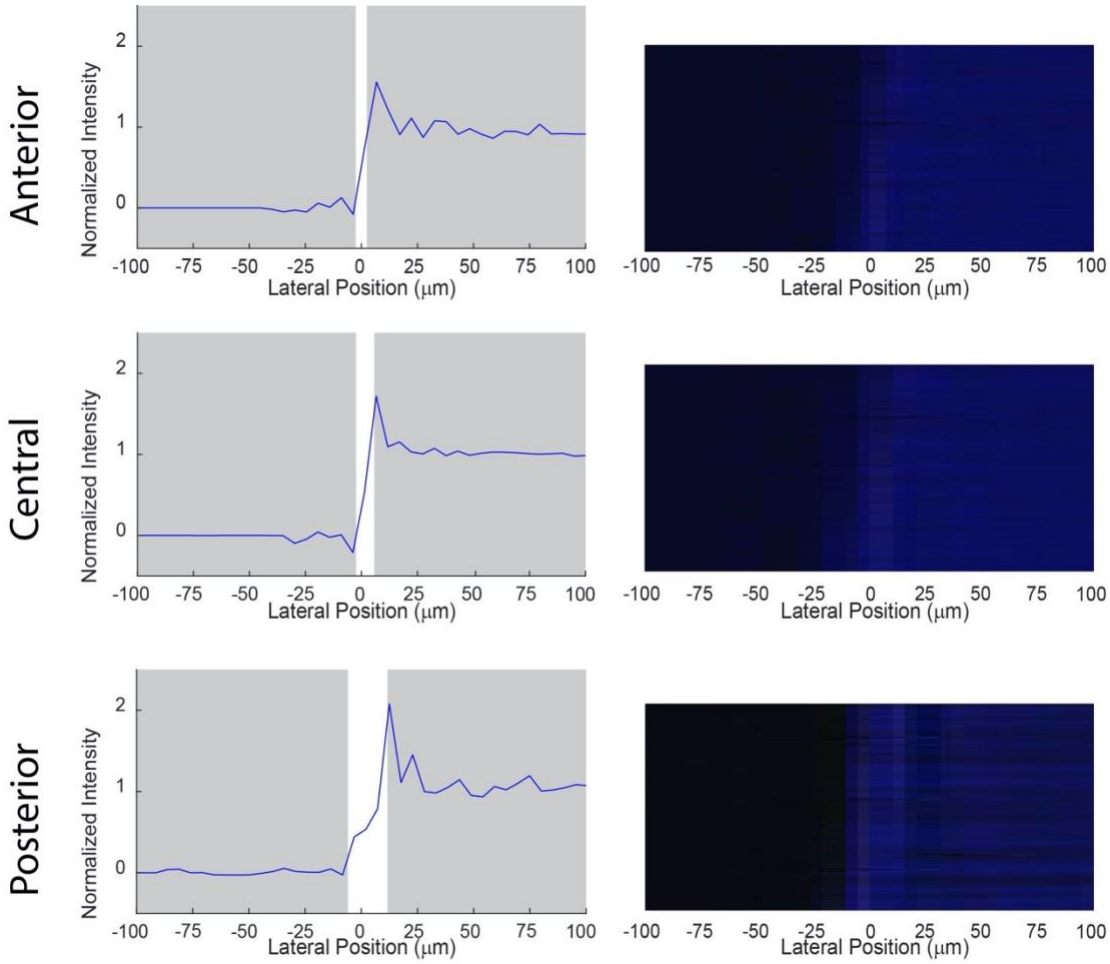

Figure 4.3: Depth analysis of optically induced transition zones. Transition zone and representative light intensity image at anterior (0 μm), central (500 μm), and posterior (1000 μm) depths from the blocking mask generated from the blue light alone. The normalized light intensity versus lateral position was analyzed using Mightex CMOS-captured images at 0, 500, and 1000 μm between the mask and camera, representing the sharpest possible transition zones through air. Point 0 μm on the horizontal axis was located at 50% normalized intensity. The transition zone at any depth did not exceed 25 μm.

At its broadest, the transition zone due to illumination was still less than 25 μm. **Figure 4.4** shows the average normalized transition zone in the blue light cross-linked porcine eyes of 610 μm extending beyond the mask surface.

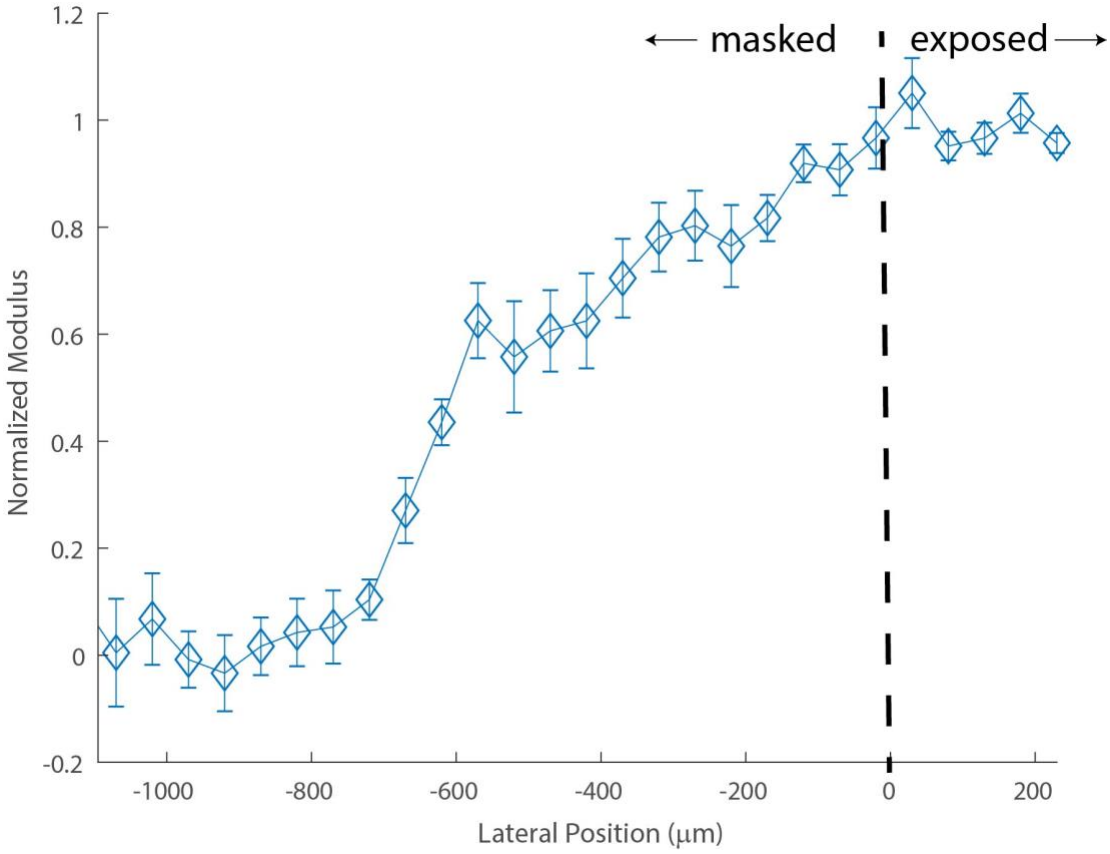

Figure 4.4: Brillouin modulus versus lateral position of locally cross-linked cornea. Averaged normalized transition zone of (n = 10) porcine corneas post blue light L-CXL. The dotted line illustrates the edge of the UV blocking mask, differentiating the blocked and exposed sections of the cornea. The average transition zone was calculated between the 10% and 90% of the maximum plateau of normalized shift. Error bars represent SEM for each position.

4.3.4 Quantifying the Scatter-induced Cross-linking Transition Zone

Figure 4.5 quantifies the scattering-induced transition zones throughout the cornea during blue light L-CXL. Through just air, therefore without any corneal scattering, a sharp transition zone of 37 $\pm$ 8.9 μm was found.

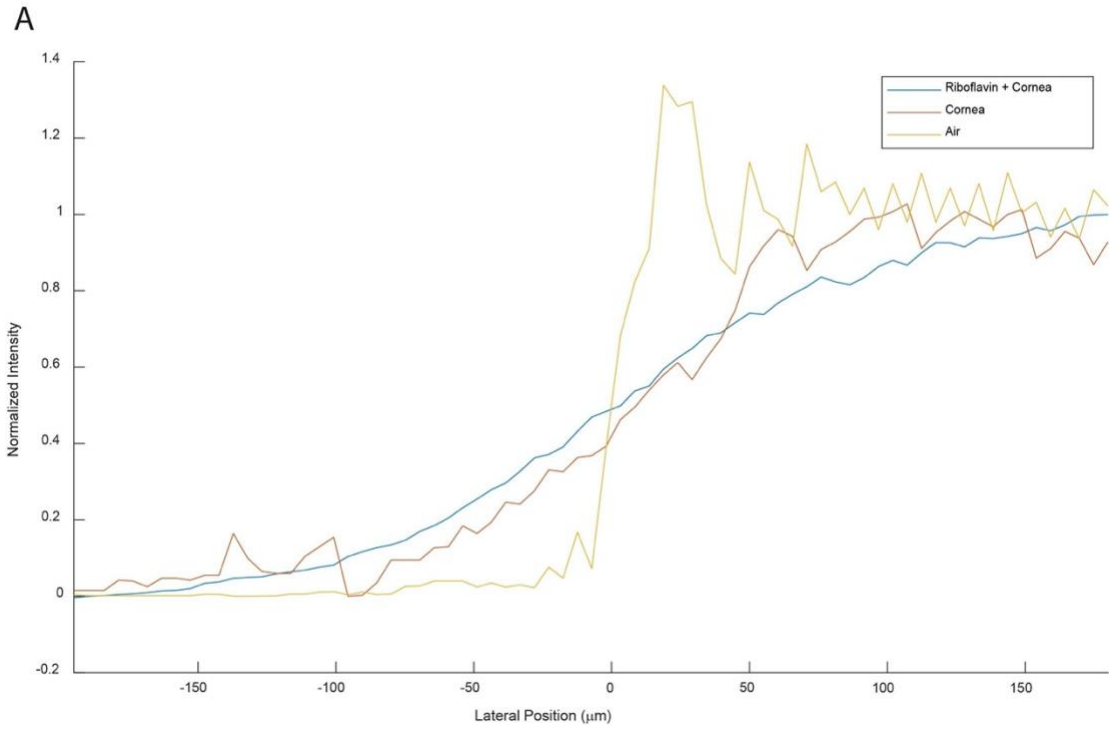

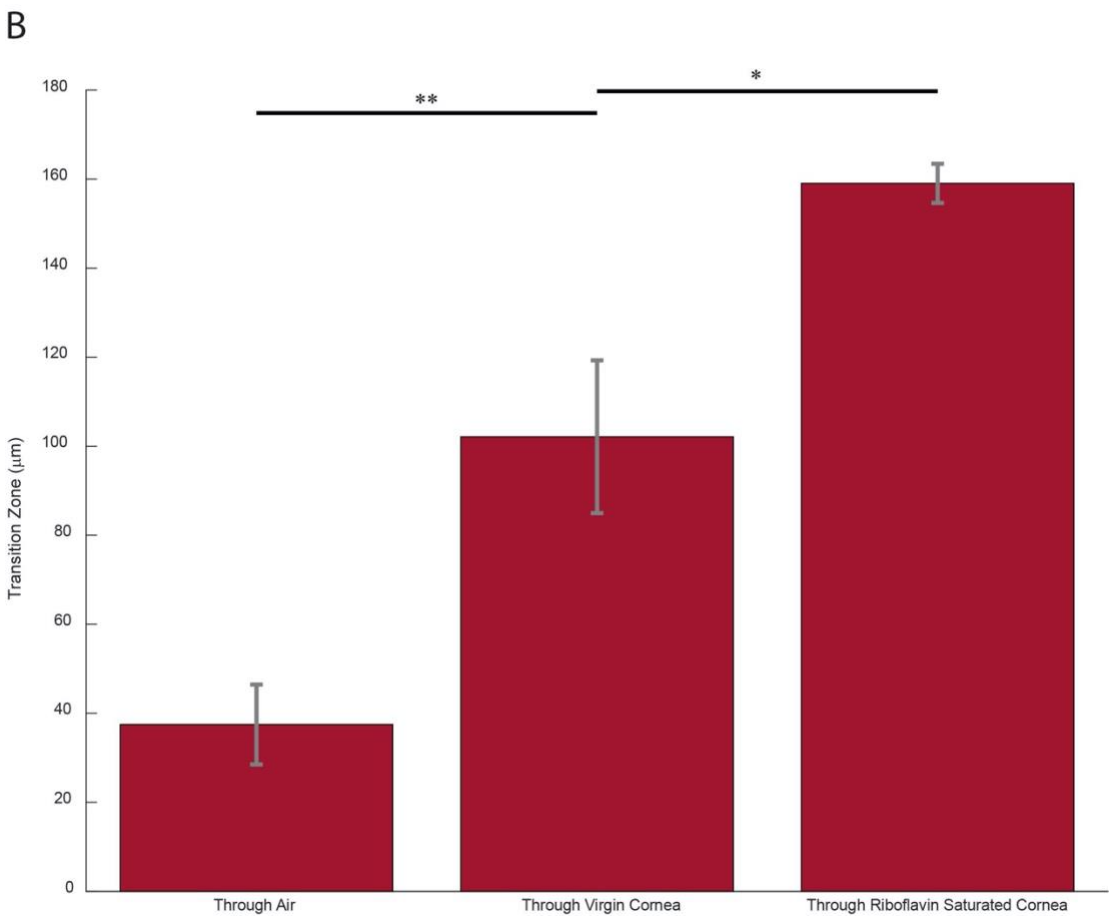

Figure 4.5: Summary of transition zone contributions. **A**: Representative graphs of the normalized light intensity versus lateral position from the 0 point at 50% intensity as the light traveled through air, a virgin cornea, and a riboflavin-soaked cornea to quantify light scattering propagation in each environment **B**: Bar graph representing the average transition zone as light traveled through three distinct environments. Error bars represent SEM for each condition (* = $p < 0.05$, ** = $p < 0.01$)

This is consistent with **Figure 4.3** as we had to increase distance between the mask and camera from 1 to 3 mm which caused the slight increase in transition zone. In an untreated cornea, the transition zone significantly increased to 102 $\pm$ 17.2 μm ($p \leq$

0.01). The transition zone of the cornea increased even further due to the presence of riboflavin, reaching 159 $\pm$ 3.2 μm; a significantly increased transition zone compared to the untreated cornea condition ($p \leq 0.05$). A summary of the transition zone findings can be found in the **Table 4.2**.

Table 4.2: Transition zones observed from each protocol.

Protocol	Average Transition Zone (μm)
Blue Light L-CXL	610
Light Propagation	25
Virgin Corneal Scattering	102
Riboflavin-Soaked Corneal Scattering	159

4.4 Discussion

In this study, we characterized the spatially varying stiffness of the cornea following L-CXL. Biomechanical imaging analysis via Brillouin microscopy demonstrated two distinct regions: a cross-linked area and a non-cross-linked area. The shift versus depth profile of the cross-linked section mimicked that of a uniformly cross-linked cornea.[11] As expected, the cross-linked section markedly differed from the non-cross-linked section in the anterior region.[11,15,101] The two sections were separated by a broad transition zone. Therefore, the cross-linking effect extended greater than the area exposed to light.

To investigate if the effect was optically induced, we replaced the UV light source with a blue laser to optimize sharpness and set the CXL procedure to replicate the stiffening

results of UV cross-linking. Under localized protocol, we observed a transition zone of over 600 μm even though the blocking mask produced an illumination transition zone through air of less than 25 μm. The broad zone within locally cross-linked corneas must be due to an intrinsic characteristic of the cornea or CXL procedure.

The experiments conducted were on *ex vivo* porcine corneas. With time, *ex vivo* corneas become increasingly opaque, thereby, becoming more susceptible to light scattering. In order to validate our findings for future *in vivo* settings, we measured the scattering effect of the porcine corneas. We found that, at a 3 mm distance from the mask, the corneal transition zone was significantly greater than the illumination transition zone through air. The scattering induced solely by the porcine corneas contributed to roughly 100 μm transition zone and increased further to over 150 μm after the corneas were soaked in riboflavin. *In vivo* corneas have lower natural scattering property,[117,118] therefore, our results represent an upper bound of the transition zone one may find *in vivo*.

Blue light was used in this experimental set up. At 15 mW/cm^2 for 20 minutes, the blue light stiffened the corneas to 180% the elastic modulus of their respective controls. This can thus be considered a suitable model to simulate the stiffening of standard CXL protocols performed using UV.[119] Clinical application calls for columnized UV-A exposure. A clinically used, columnated UV system, creating a well-confined source of light, should produce similar results to that of our setup. Here, we used a coherent laser for illumination understanding it to be an ideal optical scenario regarding the

transition zone. As expected, the blue coherent light allowed us to obtain sharp confinement of the illumination.

After considering of all these different factors, we estimated less than 250 μm of the 610 μm transition zone being due to light-related effects. Therefore, as summarized in **Table 4.2**, a large portion of the transition zone remains unaccounted by light phenomena. A number of factors could be contributing to this effect. The area of cross-linking depends on the distribution of riboflavin concentration during light exposure, absorbed photons of light, and oxygen exposure to activated riboflavin.[42,110,113,119] Throughout the 20 minutes of light exposure, there exists a diffusion of oxygen radicals and/or hydrogen peroxide,[119,120] both of which contribute to cross-linking. Therefore, any diffusion of such reactants could result in the extended cross-linking area. Furthermore, the cornea becomes increasingly turbid throughout cross-linking,[121,122] accounting for increased scattering of light as the procedure is performed. Light scattering throughout the process of L-CXL could result in the excitation of riboflavin molecules outside of the irradiated area, subsequently leading to cross-linking within the transition zone.

Localized cross-linking protocols have garnered added attention recently.[50–52] Seiler and colleagues employed localized cross-linking with treatments with customized maximal irradiation ranging from 5.4 J/cm^2 up to 10 J/cm^2 centered on the maximum posterior elevation in concentric rings and found improved maximal flattening and corneal regularization at one year but unknown long term stabilization effects.[52]

Cassagne and colleagues performed topography-guided CXL in zonal patterns with total irradiance ranging from 5.4 J/cm^2 in regions surrounding the cone to 15 J/cm^2 on top of the cone using 30 mW/cm^2 pulsed ultraviolet-A irradiance and found significant improvements in CDVA, Maximum keratometry (Kmax), mean keratometry in the inferior part of the cornea (I index), a demarcation line that was more pronounced in maximally treated areas but less pronounced in surrounding regions at one year.[50] Nordström and colleagues performed asymmetrical treatment zone centered on the area of maximum corneal steepness with treatment energies ranging from 7.2 J/cm^2 to 15.0 J/cm^2 and found improved visual acuity, spherical refractive error, and K max as compared to uniformly applied CXL using 5.4 J/cm^2 pulsed fluence.[51]

None of these protocols were based on any specific corneal stiffness alteration but rather on the general concept of applying greater irradiation leading to greater stiffness in the maximal cone region and less in surrounding regions. As localized CXL protocols become more sophisticated over time and specific corneal stiffening outcomes are targeted, the biomechanical impact on the transition zone will need to be taken into account during treatment planning.

4.5 Conclusion

Corneal ectasia is a local disruption in the integrity of the collagen matrix, resulting in a localize decrease in stiffness. To treat ectasia, corneal collagen cross-linking has been approved, yet focuses on the global cornea rather than the precise, compromised location. It has been theorized that focusing the treatment to the compromised location

would result in a safer procedure with more beneficial long-term effects. However, until now, no direct method was able to characterize the stiffening results of L-CXL. Here, we utilized the unique capabilities of Brillouin microscopy to measure the mechanical effects of L-CXL. We found a broad transition zone of approximately 600 μm between the fully cross-linked and non-cross-linked sections of the cornea in localized CXL procedures. Therefore, there exists a stiffening effect which extends beyond the irradiated area. We quantified the contribution of light propagation through the cornea, finding it only partially describes the extent of the transition zone. Finally, we validated our transition zones were not due to *ex vivo* scattering artifacts and, therefore, are a result of intrinsic corneal properties. When conducting localized CXL clinically, it will be important to account for increased stiffening outside of the irradiated area.

CHAPTER 5: DETECTING MECHANICAL ANISOTROPY OF THE CORNEA USING BRILLOUIN MICROSCOPY*

5.1 Introduction

Corneal mechanical strength is primarily provided by the stromal layer, which comprises 90% of total corneal thickness. The corneal stroma consists of nanometer-thick collagen fibrils packed into 250-300 distinct fibers, or lamellae.[123] Much effort has gone into understanding the underlying network of the collagen fibers, as the organization of the collagen network of the corneal stroma directly determines its biomechanical properties.[124] The primary source of biomechanical strength is in the anterior third of the corneal stroma, where the collagen fibers interweave with one another.[12,13] Severing the anterior fibers during the creation of a LASIK flap can lead to the onset of cornea ectasia due to the overall decrease in mechanical properties;[125,126] and corneal cross-linking (CXL) has shown to increase the overall corneal strength by promoting the fiber-to-fiber connections primarily in the anterior part of the corneal stroma.[11,127]

From a mechanical standpoint, the cornea is generally approximated as a transversely isotropic material,[58] meaning its mechanical properties are uniform on a given *en face* plane of the cornea but change if probed normal or perpendicular to the surface.[128] X-ray diffraction[32] and second/third harmonic generation[129,130] studies have demonstrated

* This work was part of a peer reviewed publication: *Webb et. al., TVST 9 (7), 2020.*

that fibers display a strongly preferred direction parallel to the corneal surface, with only a small variation of ± 3.5°, and are stacked orthogonally layer by layer.[131] The resulting mechanical anisotropy is a defining characteristic of the cornea: previous *ex vivo* measurements have reported the corneal stiffness to be hundred-fold larger when probed tangentially to the corneal surface (i.e. parallel to the collagen fibers) than when probed orthogonally to the corneal surface.[132–135] Therefore, the corneal stiffness probed in a given direction will result, to first approximation, from combination of the tangential and perpendicular moduli in orthogonal directions. Cornea mechanics as a whole is also affected by the hydration state of the cornea,[136–138] an important factor to consider given that the hydration state changes in both short and long term following clinical procedures.[139–141]

For the mechanical characterization of the cornea, Brillouin microscopy has recently emerged as an intriguing modality to perform measurements *in vivo*, in three dimensions, and without contact.[15,77,100] Historically, measuring the Brillouin frequency shift has proved beneficial in studying the mechanical changes of the cornea including characterizing cross-linking efficiency[101,142] and monitoring the progression of keratoconus.[18] Recently, the effects of water content on frequency shift have been investigated,[104] and Brillouin microscopy has been used to detect the changes in corneal hydration that accompany Fuchs' Corneal Dystrophy.[143] From a mechanical standpoint, Brillouin microscopy probes micron-level unit volumes. In this scale, Brillouin microscopy measurements of anisotropy are not sensitive to macro-level changes in hydration unless such changes in hydration affect fiber distribution at a

micron-scale level.[144] Hereby, we will refer to such hydration-independent changes in mechanical properties as changes in solid mechanics or, equivalently, changes to stromal tissue.

Brillouin microscopy has not yet been demonstrated to detect the mechanical anisotropy of the cornea. Besides the practical consequence of an incomplete characterization of corneal mechanical properties, this has generated an important question on whether, at a fundamental level, the Brillouin scattering phenomenon can be sensitive to mechanical properties that are independent to hydration at a micron-scale. The purpose of this study was to determine and demonstrate the sensitivity of Brillouin measurements to corneal mechanical anisotropy in the presence of water.

5.2 Methods

5.2.1 Brillouin Microscopy

A confocal Brillouin microscope was utilized with similar configuration of previous studies[94] as well as outlined in *Background* (*Chapter 2.6*). Briefly, a 660 nm laser with power of 15 mW was focused into the sample by an objective lens (20X / 0.4 NA, Olympus Corporation of the Americas, Center Valley, PA) with lateral resolution of ~1 μm and depth resolution of ~4 μm. The scattered light, collected through the same objective, was coupled into a single mode fiber and delivered to a two-stage virtually imaged-phase-array (VIPA) spectrometer featuring an electron multiplying charge coupled device (EMCCD) camera (IXon Du-897, Andor Technology, Belfast, United

Kingdoms). Each Brillouin spectrum was acquired in 0.2 seconds. To quantify the Brillouin shift at each sample location, raw spectra from the camera were fitted using a Lorentzian function and calibrated using the known frequency shifts of water and methanol.

From the Brillouin frequency shift, the local mechanical properties of the cornea can be estimated using *Equation 2.1*. The spatially varying ratio of $\frac{\rho}{n^2}$ was approximated to the constant value of 0.57 g/cm^3 based on literature values[92,93,145–147]; we estimate this to introduce a 0.3% uncertainty throughout the cornea. We have previously validated the strong correlation (R^2 = 0.98) between changes in Brillouin-derived longitudinal modulus of elasticity and tangent modulus of porcine corneas at very low strain (< 10%).[101]

5.2.2 Measurements of Porcine Corneal Globes and Buttons

Porcine eyes were obtained on the day of enucleation from a local slaughterhouse (Wagner Meats, Mount Airy, MD) as well as the day following enucleation via overnight delivery (J&J Packing Company, Brookshire, TX); all eyes were kept on ice until the start of each experiment. All corneas were inspected prior to use and damaged or unclear tissue was discarded prior to experimentation. For all eyes, the epithelium was removed by careful debridement with a razor blade. Eyes were randomly assigned to either be measured as intact globes or first dissected in order to measure central 5.0 mm punched buttons (Disposable Biopsy Punch, Integra Miltex, York, PA).

Both cornea globes and buttons were mounted on the Brillouin microscope using a 360° inclinational stage with 1° measurable increments. Prior to mounting on the stage, button samples were rested on a microscope slide via a coupling gel (Systane Ultra Lubricating Eye Drops). As demonstrated by Fig. 1A, the samples were measured at a selected angle respective to the incident laser with 0° indicating the incident laser was positioned orthogonal to the corneal surface and +/- indicating inclination directionality. Based on this directional axis, a 90° rotation would position the incident laser parallel to the preferred fiber direction; thereby, tangential to the corneal surface. For the intact globes, scanning order was 0°, +15°, -15°, +30°, -30°. For the buttons, scanning order was 0° followed by 30°. Each scan, including the time it took to rotate the cornea and reposition the incident beam, was no longer than 3.5 minutes. The number of angle variations was chosen to minimize the total time between the first and last scan in order to limit dehydration artifacts while still demonstrating an evident difference in probing direction. The maximum angle of 30° was chosen in order to maintain adequate signal intensity of our setup and to minimize optical artifacts from tilting the sample. It is worth noting that with each inclination, the corneal thickness appears to increase in the Brillouin image as it is probed at an angle. For analysis, the thicknesses of the scans were normalized and the anterior third of the cornea was used for analysis while a sample (100 μm x 200 μm) of aqueous humor within the eye globe or lubricant gel applied to the posterior of the cornea button was used as respective, isotropic controls.

5.2.3 Corneal Hydration / Dehydration

Corneal hydration was controlled and monitored throughout the experiments. Prior to a scan, corneal buttons were subjected to hydration / dehydration protocols similar to *Shao et. al.*[104] in which the button was immersed in distilled water for 30-180 minutes to induce hydration or left out in air for 15-30 minutes to induce dehydration. Following each respective protocol, the cornea was weighed (W') and imaged via Brillouin microscopy. The cornea was then left out to completely dry in air for 72 hours and reweighed (W_0). The hydration (H), a unitless ratio between the mass of the water content and dry mass of the cornea, at the time of each measurement was then calculated as:

$$H = \frac{w' - w_0}{w_0} \qquad \textit{(Eqn. 5.1)}$$

5.2.4 Statistical Analysis

To compare the Brillouin-derived longitudinal modulus of elasticity of corneal buttons rotated at 0° and 30° as well as the Brillouin frequency shift of 0° repeated measurements, a Wilcoxon Signed-Rank Test was performed. To compare the Brillouin frequency shift of virgin and cross-linked corneas, a Wilcoxon Rank Sum Test was performed. For measurement consistency, throughout the paper we reported average values ± standard error of anterior third of the stroma.

5.3 Results

5.3.1 Mechanical Anisotropy of Intact Porcine Corneas

A dependence of Brillouin frequency shift on the angle of inclination of the cornea was observed as shown in **Figure 5.1**. Intact corneas (n = 10) were mounted on an inclinational stage and imaged via Brillouin microscopy at 0°, +15°, -15°, +30°, and -30° relative to the incident laser (**Figure 5.1.A**). **Figure 5.1.B** depicts representative Brillouin maps of a single cornea scanned at 0°, +15°, -15°, +30°, and -30°. As indicated by the warmer colors, the Brillouin frequency shift increases with the angle of inclination and symmetrically with respect to the 0° configuration, i.e. the configuration where the probed modulus is perpendicular to the direction of the collagen fibers. **Figure 5.1.C** shows a quantification of this effect for n = 10 intact corneal samples. The frequency shift was at a minimum (6.44 ± 0.04 GHz) when the cornea was rotated 0° to the incident laser, i.e. when the measurements were probed orthogonal to the collagen fiber direction. As the cornea was rotated further from the initial 0° position, the measured shift followed a sinusoidal-squared relationship with probing angle with an average frequency shift of 6.49 ± 0.03 GHz, 6.49 ± 0.04 GHz, 6.53 ± 0.03 GHz, and 6.53 ± 0.03 GHz at +15°, -15°, +30°, and -30° respectively. The average shifts of equal but opposite angles (i.e. +15°, -15°) displayed the same frequency shift within the instrument sensitivity, demonstrating hydration effects due to dehydration were negligible. Further evidence that the changes in frequency shift were due to mechanical anisotropy was the constant behavior of aqueous humor within each eye globe, which was used as an isotropic control. From the experimental start to

finish (0° vs -30°), the average frequency shift of aqueous humor deviated only slightly (from 6.11 ± 0.02 GHz to 6.13 ± 0.01 GHz) and was ascribed to a loss of signal strength in the posterior portion of the sample and/or instrument sensitivity error.

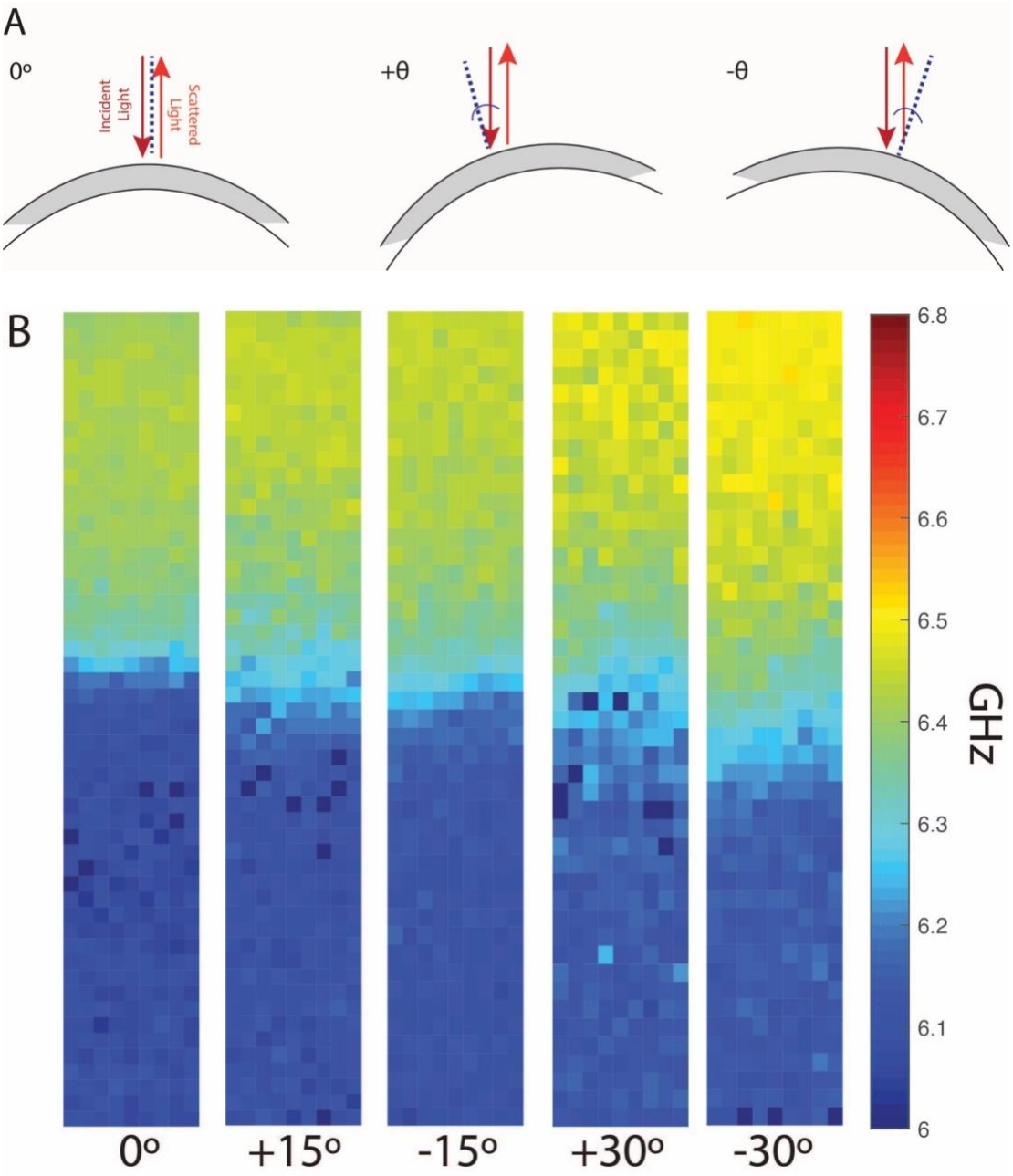

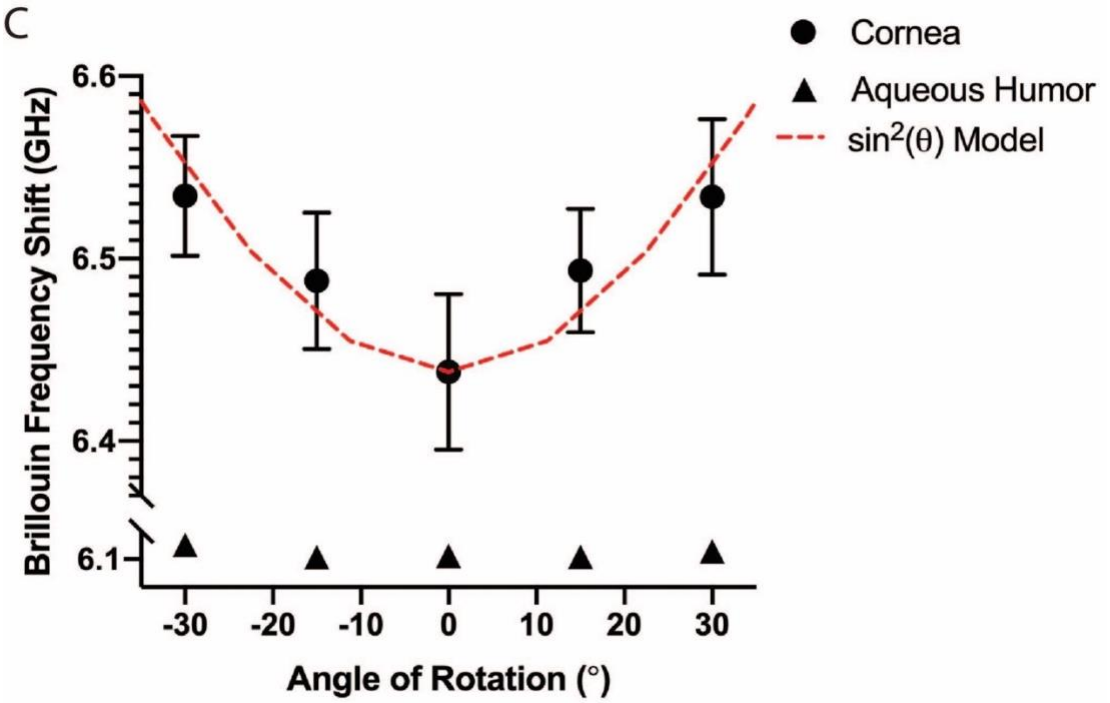

Figure 5.1: **A**: Schematic demonstrating the probing angle of the incident and collected scattered light relative to the corneal surface. 0° indicates the incident laser is positioned orthogonal to the corneal surface; +/- indicates the directionality relative to 0°. The dotted blue line shows the normal path to the corneal apex. **B**: Representative Brillouin frequency maps (200 μm x 1200 μm) of a single cornea scanned at 0°, +15°, -15°, +30°, -30° inclination relative to the incident laser. The globes are depicted anterior upwards with aqueous humor at the bottom of the image. The warmer colors correspond to a higher frequency shift. **C**: Average Brillouin frequency shift of the anterior third of (n = 10) identical corneas (*dots*) and a 200 μm x 100 μm sample of aqueous humor (*triangles*) measured at 0°, +15°, -15°, +30°, -30° inclination relative to the incident laser. A $\sin^2$ model (*dotted line*) was plotted with a wavelength of 180° fit to the experimental data. Error bars represent the standard error of the mean for each inclination and are within the size of the symbol when not seen.

5.3.2 Mechanical Anisotropy of Porcine Corneal Buttons

To increase the control over the measurement conditions, experiments were performed on central corneal buttons punched from *ex vivo* porcine globes. **Figure 5.2.A** shows representative images of the same cornea sample measured at 0° and 30°. The measured Brillouin frequency shifts were converted to longitudinal modulus of elasticity, using the incident laser wavelength of 660 nm and assuming a constant index of refraction and density of 1.37 and density of 1080 kg/m^3 for corneal tissue.[15,104] **Figure 5.2.B** demonstrates the difference in longitudinal modulus of elasticity, derived via Brillouin microscopy, between identical corneas (n=10) measured at 0° then 30°. The average longitudinal modulus of elasticity ± standard error of the anterior third section of the corneas at +30° inclination (2.66 ± 0.03 GPa) significantly differed ($p < 0.01$) from the same corneas measured at 0° inclination (2.60 ± 0.03 GPa). As an isotropic sample control, index-matching, lubricant gel was placed on the posterior side of the cornea and measured at each inclination. The gel at 30° and 0°, 2.37 ± 0.06 GPa and 2.37 ± 0.04 GPa respectively, did not significantly differ ($p > 0.05$) and the difference between the two was within instrument sensitivity (10 MHz). To test for unwanted changes in Brillouin-derived longitudinal modulus of elasticity due to dehydration and/or temperature changes between scans, (n = 10) corneas were measured at 0° ($M_{0°}^{initial}$) followed by a repeated measurement again at 0° ($M_{0°}^{repeat}$); replicating the time between measurements at 0° then 30°. As shown in **Figure 5.2.C**, the average difference in longitudinal modulus of elasticity between the repeated measurements ($M_{0°}^{repeat} - M_{0°}^{initial}$) was not significantly different than zero ($p > 0.05$)

and within the instrument sensitivity, indicating no change in frequency shift due to the time between scans.

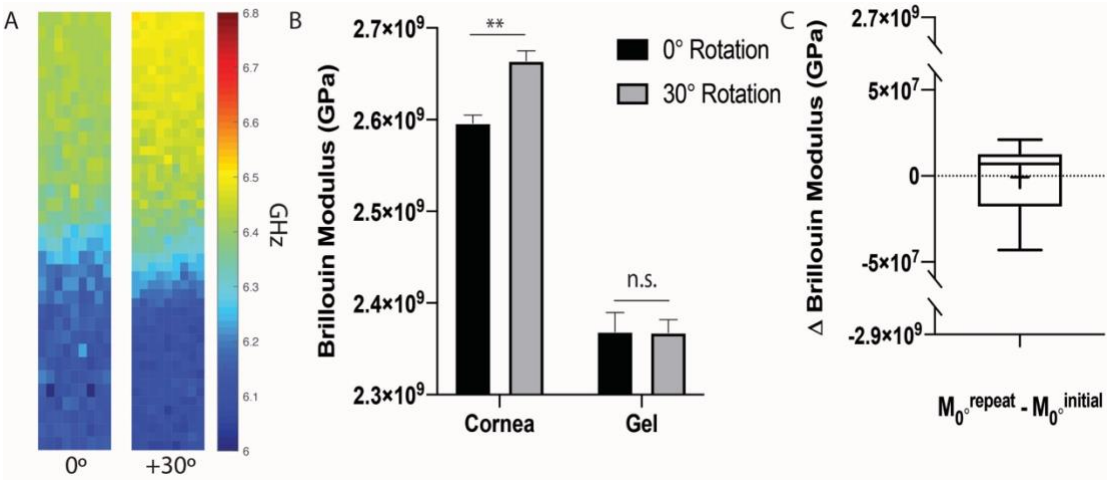

Figure 5.2: **A**: Representative Brillouin frequency maps (200 μm x 1200 μm) of a single cornea and gel scanned at 0° and 30°. The cornea is positioned anterior upward. The warmer colors correspond to a higher frequency shift and, thereby, a higher longitudinal modulus of elasticity. **B**: Average longitudinal modulus of elasticity derived via Brillouin frequency shift, of (n = 10) individual corneal anterior sections as well as the isotropic gel applied to the posterior of each sample rotated at 0° and 30°. Error bars represent standard error of the mean for each condition. **C**: Difference in Brillouin-derived longitudinal modulus of elasticity between (n = 10) identical, repeated measurements of corneas scanned at 0°. The cross within the box represents the mean value while the horizontal line represents the median. (** = $p < 0.01$)

5.3.3 Mechanical Anisotropy at Varying Hydration Levels

We next determined how the sensitivity to mechanical anisotropy of Brillouin microscopy was affected by the hydration level of the cornea samples. To do this, we compared the Brillouin frequency shift of (n =26) corneas, each with a distinct level of hydration resulting from a previously described dehydration / hydration protocol, measured at 0° (Ω_{0°) and then 30° (Ω_{30°). The average frequency shift of the anterior third of each cornea was calculated at both inclinations and Ω_{30° vs Ω_{0° was plotted (Fig. 3). The data within **Figure 5.3** includes a large range of corneal hydrations throughout the experiment from 2.58 to 22.49, corresponding to 72.0% and 95.7% water content respectively. The water content of most species is ~76% in normal physiological conditions, which corresponds to a hydration level of 3.2 (=H_0);[148] therefore, our range included all values within physiological expectation. Experimental data are fit extremely well by the linear fit $\Omega_{30^\circ} = \Omega_{0^\circ} + 0.06$ (R^2 = 0.98) with slope 1.0 and origin intercept of 60 MHz.

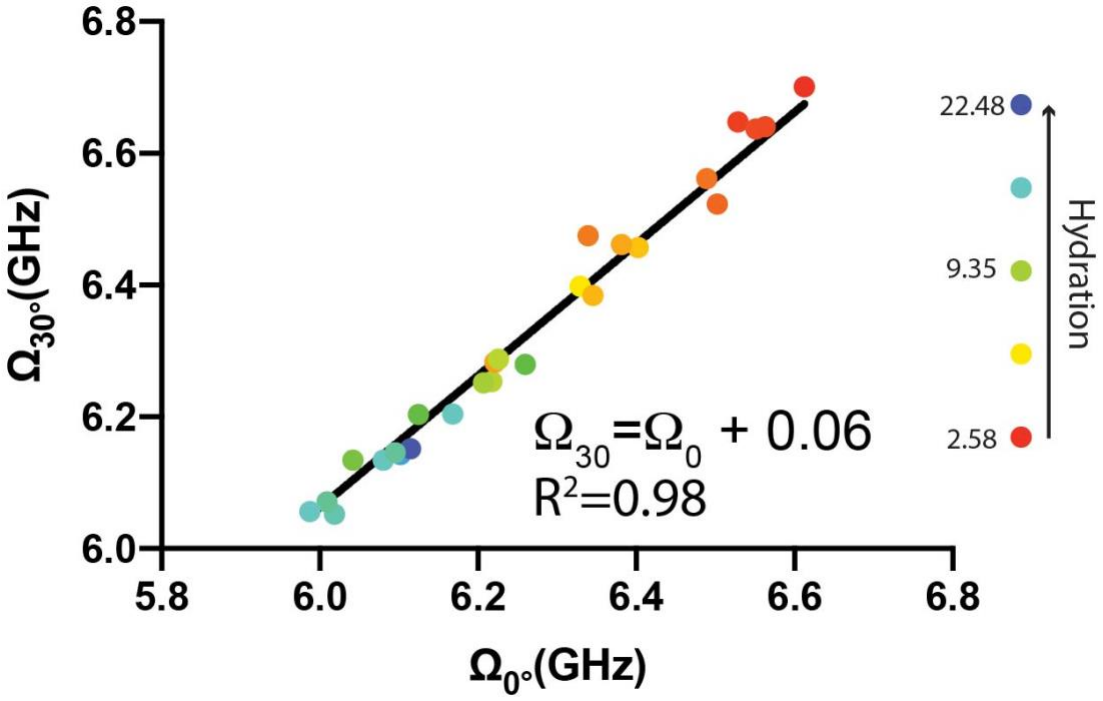

Figure 5.3: Average Brillouin frequency shifts of the anterior third of individual corneas (n = 26) imaged at 0°($\Omega_{0°}$) and 30° ($\Omega_{30°}$). The samples varied in hydration from 2.58 to 22.49, as the colder and warmer colored dots correspond to higher and lower levels of hydration respectively. A line with a slope fixed at 1.0 was fit as $\Omega_{30°} = \Omega_{0°} + 0.06$ ($R^2 = 0.98$).

5.4 Discussion

The anisotropy of the cornea is central to the mechanical function of the cornea and comes from the unique architecture of collagen fibers within the stroma: the elastic modulus probed parallel to the collagen fiber orientation has been shown to be remarkably larger than the one probed orthogonal to the fiber direction.[132–135] Brillouin microscopy is an emerging modality capable of probing corneal mechanics without contact or perturbations, thus offering unique *in vivo* potential. However, until now,

no Brillouin measurement has detected the mechanical anisotropy present within a cornea.

Brillouin microscopy measures the frequency shift induced by light interacting with acoustic phonons propagating within a material; in back-scattering configuration, it probes the high-frequency longitudinal modulus of elasticity of a material in the direction of the incident laser. Previously, Brillouin microscopy had been shown to detect mechanical anisotropy of non-biological samples or isolated fibers[76,78,149] but not of the cornea, or other biological tissues. Naturally, this has raised the question as to whether the Brillouin phenomenon in biological, hydrated samples loses sensitivity to mechanical properties that are intrinsic to the solid collagen network of the stromal tissue. In order to evaluate the sensitivity of Brillouin microscopy to mechanical anisotropy, cornea samples were imaged at varying angles of inclination and various levels of hydration. Because Brillouin measurements probe the longitudinal modulus of elasticity along the direction of the laser beam in back-scattering geometry, as we probed higher angles of corneal inclination, i.e. closer to parallel with the collagen fibers, the Brillouin frequency shift increased. Due to the relationship between frequency shift and longitudinal modulus of elasticity, we can deduce that Brillouin microscopy detected higher mechanical modulus as the inclination of the collagen fibers within the cornea changed from orthogonal to parallel to the incident laser. Specifically, the increase followed the expected $\sin^2(\theta)$ relationship consistent with expectations and previous literature for a material with transverse mechanical anisotropy with two principal moduli along perpendicular and parallel directions.[78,149]

Importantly, as demonstrated by the constant slope of one in Fig. 3, the mechanical anisotropy detected between 0° and 30° remained constant throughout hydration conditions ranging from 72.0% and 95.7% water content. The 60 MHz origin intercept is consistent with **Figure 5.2** and can be interpreted as the frequency shift due solely to the solid mechanical differences, independent from hydration, between a cornea measured at 30° and 0°. This suggests that, unlike synthetic hydrogels, where Brillouin microscopy was found to lose sensitivity to mechanical changes at high water content,[103,150] Brillouin microscopy does not lose sensitivity to changes in solid mechanics of the cornea even in highly hydrated samples.

There are limitations to our study. The current study provides information on the transverse corneal anisotropy, i.e. when the cornea is rotated in respects to the depth axis. However, there are a number of benefits to assessing in-plane anisotropy by comparing the stiffness across the nasal-temporal direction versus the superior-inferior direction.[101] In the future, now that we have proven Brillouin microscopy is capable of measuring corneal anisotropy, we will look to measure mechanical differences across other directions within the cornea. Additionally, the procedure performed in this study refers to the central and anterior part of the porcine cornea (0.2 x ~0.25 mm). Therefore, the mechanical anisotropy will need to be characterized in the human cornea to gain specific information of clinical procedures on middle or peripheral sections of the human cornea with potentially different orientation of collagen fibers. Furthermore, in our ex vivo experiments, we measured corneal weight to quantify hydration; to

practically translate these procedures to clinical setting, hydration will need to be quantified via corneal thickness.

For Brillouin measurements performed on intact eye globes, both *in vivo* and *ex vivo*, this sensitivity must be taken into account as the frequency shift will be dependent on the angle of the collagen fibers, thereby, the natural curvature of the eye. Therefore, similar to the recently developed polarization-sensitive (PS)-OCT which compensates for scanning angle-induced artifacts,[151,152] *en face* Brillouin maps of the cornea can be normalized based on the angle dependence of Brillouin shift found in this study.

5.5 Conclusion

The collagen network throughout the cornea presents unique, directionally dependent mechanical properties. In order to better understand the link between cornea microstructure and mechanical properties, a direct, three-dimensional device with micron-level resolution is required. However, until now, Brillouin microscopy had not shown sensitive to these directionally dependent mechanical properties. Here, by combining Brillouin measurements of different geometrical configuration, we demonstrated that Brillouin measurements are sensitive to the mechanical anisotropy of the cornea. Detecting mechanical anisotropy suggested Brillouin microscopy as an effective method to study the collagen directionality and mechanical relationship. More so, the detection established the capability of Brillouin microscopy to measure pure mechanical properties which are independent from water content, paving the way

towards isolating the contributions of hydration and solid mechanics on Brillouin frequency shift.

CHAPTER 6: QUANTITATIVE RELATIONSHIP BETWEEN BRILLOUIN SHIFT AND ELASTIC MODULUS*

6.1 Introduction

Within the cornea, a weakened elastic modulus is an early indication of keratoconus,[153] as the weakened cornea, under intraocular pressure, leads to the clinically observed bulging associated with the disease.[154] Additionally, an undetected weakened cornea that undergoes a refractive procedure also has a very high risk of developing ectasia.[125] In addition, to treat keratoconus and other ectatic disorders, corneal cross-linking is performed to increase the elastic modulus the cornea.[127] Therefore, accurate measurements of corneal elasticity provide a vital tool in early keratoconus diagnosis, refractive procedure screenings, and assessing the treatment of ocular disorders.

Brillouin microcopy is a noninvasive method to extract mechanical properties of a sample, potentially bridging this clinical gap. However, Brillouin measurements, probing the longitudinal modulus of material at high frequency, have only yielded information on the elastic modulus at physiological time scales via empirical correlations and in tightly controlled experimental conditions.[33,100,101] We hypothesize that, although the Brillouin-derived longitudinal modulus and traditional elastic modulus are fundamentally different quantities, such correlations stem from a common dependence on underlying biophysical and biochemical factors. Namely in the cornea,

* This work was part of a peer reviewed publication: *Webb et. al., TVST 9 (7), 2020.*

the mechanical properties are largely dictated by two factors: hydration and the solid matrix modulus. Indeed, as described in *Chapter 5*, Brillouin frequency shift depends on both water content and the mechanical properties of the solid matrix through a wide range of hydration (2.5 – 22.5).[155] Gold-standard, low frequency elastic modulus of biological material are also expected to depend on both hydration and the solid matrix modulus.[156–158] Here, we theoretically and experimentally quantify relationships within the cornea in which Brillouin and low frequency elastic modulus depend on hydration and the corneal solid matrix. Using the moduli dependencies of hydration and solid matrix, we also derive a quantitative procedure to extract the elastic modulus of the cornea from experimental measurements of Brillouin frequency shift and hydration, two clinically available parameters.

6.2 Methods

6.2.1 Corneal Hydration / Dehydration

Corneal hydration was controlled and monitored throughout the experiments in an identical manner as *Chapter 5.2.3*. Prior to a scan, corneal buttons were subjected to hydration / dehydration protocols similar to *Shao et. al.*[104] in which the button was immersed in distilled water for 30-180 minutes to induce hydration or left out in air for 15-30 minutes to induce dehydration. Following each respective protocol, the cornea was weighed (W') and imaged via Brillouin microscopy. The cornea was then left out to completely dry in air for 72 hours and reweighed (W_0). The hydration (H), a unitless ratio between the mass of the water content and dry mass of the cornea, at the time of each measurement was then calculated using *Equation 5.1*.

6.2.2 Corneal Cross-linking

CXL was used to vary the mechanical properties of corneal buttons. One drop of riboflavin solution (riboflavin 0.1% - dextran 10%) was topically applied to the button every 3 minutes for 20 minutes. Then, the saturated button was exposed to a constant 9 mW/cm^2, 365 nm UV-A light (UV Curing LED System, Thorlabs, Newton, NJ) for 10 minutes, during which one drop of riboflavin solution was administered at the 5-minute interval. An accelerated cross-linking protocol was used in order to minimize any variation in tissue hydration and expedite overall procedure time.

6.2.3 Brillouin Microscopy

A confocal Brillouin microscope was utilized with similar configuration of previous studies[94] as well as outlined in *Background* (*Chapter 2.6*) to imagine samples throughout this study. Briefly, a 660 nm laser with power of 15 mW was focused into the sample by an objective lens (20X / 0.4 NA, Olympus Corporation of the Americas, Center Valley, PA) with lateral resolution of ~1 μm and depth resolution of ~4 μm. The scattered light, collected through the same objective, was coupled into a single mode fiber and delivered to a two-stage virtually imaged-phase-array (VIPA) spectrometer featuring an electron multiplying charge coupled device (EMCCD) camera (IXon Du-897, Andor Technology, Belfast, United Kingdoms). Each Brillouin spectrum was acquired in 0.2 seconds. To quantify the Brillouin shift at each sample location, raw spectra from the camera were fitted using a Lorentzian function and calibrated using the known frequency shifts of water and methanol.

From the Brillouin frequency shift, the local mechanical properties of the cornea can be estimated using *Equation 2.1*. The spatially varying ratio of $\frac{\rho}{n^2}$ was approximated to the constant value of 0.57 g/cm^3 based on literature values[92,93,145–147]; we estimate this to introduce a 0.3% uncertainty throughout the cornea.

6.2.4 Modeling Brillouin Shift Dependence on Hydration and Solid Mechanics

Previously, Shao *et al*. described the dependence of corneal Brillouin shift from corneal hydration.[104] Here, we extend the aforementioned model to include the effect of solid mechanics. The Brillouin frequency shift is a function of incident wavelength (λ), longitudinal modulus of elasticity (M), mass density (ρ), and refractive index (n) as shown by:

$$\Omega = \frac{2}{\lambda} n \sqrt{\frac{M}{\rho}} = \frac{2}{\lambda} n \sqrt{\frac{1}{\rho \beta}} \qquad (Eqn.\ 6.1)$$

Given that, for soft tissues, one can approximate the Poisson's ratio as ~0.5 and, therefore, nearly incompressible, longitudinal modulus is dramatically higher than shear modulus (μ):

$$K = \frac{1}{\beta} = M - \frac{4\mu}{3} \qquad (Eqn.\ 6.2)$$

Therefore, the bulk modulus (K) is approximately equal to the longitudinal modulus of elasticity and tissue compressibility (β), which normally is considered as the inverse of the bulk modulus, can approximated as the inverse of the longitudinal modulus of elasticity for this model.[103] To account for the changes in Brillouin shift due to

hydration, we can use the following biphasic approximation as performed in the original Brillouin shift model:

$$n = n_w f_w + n_s(1 - f_w) \qquad (Eqn.\ 6.3.a)$$

$$\rho = \rho_w f_w + \rho_s(1 - f_w) \qquad (Eqn.\ 6.3.b)$$

$$\beta = \beta_w f_w + \beta_s(1 - f_w) \qquad (Eqn.\ 6.3.c)$$

The subscripts $_w$ and $_s$ denote the contributions from the water and solid components respectively; f_w denotes the volume fraction of water within the tissue.

We can indicate the changes in volume fraction of water as:

$$H = \frac{f_w}{1.25(1-f_w)} \qquad (Eqn.\ 6.4.a)$$

and

$$f_w = f_{w0}(1 + x) \qquad (Eqn.\ 6.4.b)$$

where the subscript $_0$ implies a physiological value; and the variable $x = \frac{H-H_0}{4H+H_0}$ conveniently describes the change in tissue hydration (*H)*. This allows *Equations 6.3.a,b,c* to be rewritten in terms of the hydration change x:

$$\Delta n = (n_w - n_s) f_{w0} x \qquad (Eqn.\ 6.5.a)$$

$$\Delta \rho = (\rho_w - \rho_s) f_{w0} x \qquad (Eqn.\ 6.5.b)$$

$$\Delta \beta = (\beta_w - \beta_s) f_{w0} x \qquad (Eqn.\ 6.5.c)$$

The model, thus far, only describes changes in the quantities due to hydration. However, while index and density changes can be fully described by changes in hydration, the compressibility of the sample can also change as a result of changes in

solid mechanics independent of hydration. Thus, the compressibility in *Equations 6.5.c* needs to include an additional term reflecting changes in solid compressibility ($\Delta\beta_s$):

$$\Delta\beta = (\beta_w - \beta_s) f_{w0} x + \Delta\beta_s (1 - f_{w0}) \qquad (Eqn.\ 6.6)$$

where $\Delta\beta_s = \beta_s - \beta_{s0}$. We can therefore derive an equation to describe the Brillouin frequency shift behavior as a result of small changes in both hydration and solid mechanics:

$$\Omega = \frac{2}{\lambda}(n_0 + \Delta n)\sqrt{\frac{1}{\rho_0 + \Delta\rho}}\sqrt{\frac{1}{\beta_0 + \Delta\beta}}$$

$$= \Omega_0 \times (1 - 0.114x) \times \frac{1}{\sqrt{1 - 0.19x}} \times \frac{1}{\sqrt{1 + 0.77x + 5.54\times10^8 \Delta\beta_s}} \qquad (Eqn.\ 6.7)$$

where all values for numerical parameters are listed in **Table 6.1**.[104,148,159–162]

Table 6.1: Various parameters input into the model to yield *Equation 6.7*.

Parameter	Value
f_{w0}	0.8
H_0	3.2
n_0	1.375
n_w	1.335
n_s	1.531
ρ_0	$1050\ \frac{kg}{m^3}$
ρ_w	$1000\ \frac{kg}{m^3}$
ρ_s	$1250\ \frac{kg}{m^3}$
β_0	$3.61\times 10^{-10}\ Pa^{-1}$
β_w	$4.31 \times 10^{-10}\ Pa^{-1}$

β_{s0}	$0.83 \times 10^{-10}\ Pa^{-1}$
Ω_0	6.49 GHz

6.2.5 Measuring the Elastic Modulus via Compression Testing

The mechanical properties of 5 mm corneal buttons were tested using a Microsquisher compressive stress-strain instrument (model: MT G2) and the associated Squisherjoy software (Cellscale, Waterloo, Ontario). The instrument directly compressed the corneal samples using a 6 mm x 6 mm plate attached to a 1.5748 mm diameter microbeam. The plate was manually lowered until fully engaging the corneal sample. Then, over the course of 4 s, a ramped preload of 100 μN was applied before holding its position for an additional 60 s. Immediately after the hold, the cornea underwent a 30% strain over the course of 72 seconds. To obtain the elastic modulus of a sample, the Stress (*Force/Area*) vs Strain (*Displacement/Thickness*) curve was obtained and the slope of the linear segment of the curve following the sleek strain was quantified. For each sample, we reported the elastic modulus at 1.5 - 4.5% strain. To account for experimental variability, the elastic modulus and hydration values were averaged within hydration groups of 3 (i.e. H = 0-3, 3-6, and so on).

6.2.6 Modeling Elastic Modulus Dependence on Hydration and Solid Mechanics

We will approximate the cornea as a biphasic, porous material comprised of a fluid (water) and solid (matrix) component and adapt models previously used for biological tissue.[163,164] The elastic modulus of a material can be obtain using the relationship to shear modulus (μ) and Poisson's ratio (ν):

$$E = 2\mu(1+\nu) \qquad (Eqn.\ 6.8)$$

where μ is shear modulus and ν is the Poisson ratio of the mixture. As the water content is varied, both the shear modulus and the Poisson's ratio of the mixture will vary. The varying shear modulus of a biphasic material can be written in terms of water content:

$$\mu = \mu_s(1 - f_w) \qquad (Eqn.\ 6.9)$$

where μ_s is the shear modulus of solid component of the mixture without pores and f_w, like in the previous section, is volumetric water fraction. Then, the Poisson's ratio can too be written in terms of water content in biological tissues:

$$\upsilon = \frac{H_A - 2\mu_0(1-f_w)}{2H_A - 2\mu_0(1-f_w)} \qquad (Eqn.\ 6.10)$$

where

$$H_A = \frac{D_0(1-f_w)^n}{\alpha(2-f_w)^2}(f_w)^{2-n} \qquad (Eqn.\ 6.11)$$

where D_0 is the diffusivity of water in the aqueous solution and α and n are material parameters of the biological sample. For our case, by saturating the cornea using distilled water, D_0 is the diffusivity of water in water (water self-diffusion = $2.3*10^{-9}$ m^2/s at 25° C).[165] Gu *et. al.* fit parameters $\alpha = 3.39*10^{-18}$ m^2/Ns and n = 3.236 remained constant for both agarose gel (2-14.8% w/w) and bovine cartilage.[166] Therefore, these parameters were kept constant for our porcine cornea model.

Combining these equations, we yield a theoretical relationship of elastic modulus that depends on water content and the shear modulus of the solid matrix:

$$E = 2\mu_s(1-f_w) * 1 + \frac{\frac{D_0(1-f_w)^n}{\alpha(2-f_w)^2}(f_w)^{2-n} - 2\mu_0(1-f_w)}{2\left(\frac{D_0(1-f_w)^n}{\alpha(2-f_w)^2}(f_w)^{2-n} - \mu_0(1-f_w)\right)} \qquad (Eqn.\ 6.12)$$

6.3 Results

6.3.1 Decoupling Brillouin Shift Dependence on Hydration and Solid Mechanics in CXL Procedures

It is widely expected that CXL affects corneal mechanics both via immediate hydration changes and via more lasting changes in solid mechanics.[139,167,168] Corneal buttons in virgin conditions (n = 26) and CXL conditions (n = 15) of varying hydrations (from 2.58 to 22.49) were prepared and measured according to the procedures described in the methods section. A statistically significant difference was measured between virgin and cross-linked corneas at low, medium and high hydration (Table 6.2).

Table 6.2: Brillouin Frequency Shift of Virgin vs CXL Corneas

Hydration	**Ω_{virgin} (GHz)**	**Ω_{CXL} (GHz)**	**Significance**
Low (H < 5)	6.51 ± 0.03	6.64 ± 0.02	** (p < 0.01)
Medium (5 < H < 10)	6.29 ± 0.03	6.38 ± 0.02	* (p < 0.05)
High (H > 10)	6.09 ± 0.02	6.20 ± 0.02	** (p < 0.01)

To further understand the dependence on hydration and solid mechanics, the Brillouin frequency shift of the anterior section of each cornea was measured and plotted as a function of hydration (**Fig. 6.1**). **Figure 6.1** also shows the prediction of *Equation 6.7* (*blue line*) as the theoretical model describing the dependence of Brillouin frequency shift on hydration. Here, Ω_0 was fit to 6.49 GHz and $\beta_s = 0.83 \times 10^{-10}$ Pa^{-1} ($\beta_s =$

β_{s0}; $\Delta\beta_s = 0$) as we assumed no changes in solid compressibility due to changes in hydration.

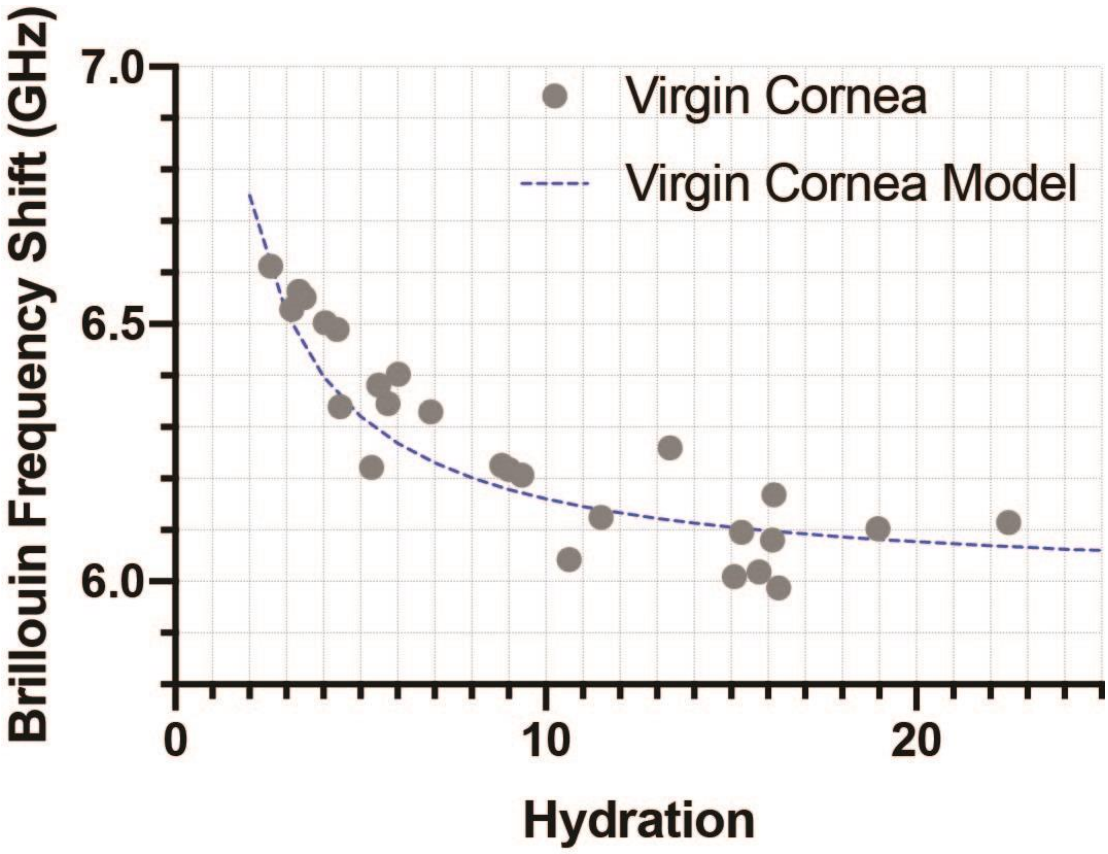

Figure 6.1: Average Brillouin frequency shift of the anterior of (n = 26) virgin corneas versus the measured hydration (*dots)*. Computational model of the relationship between Brillouin frequency shift, hydration, and solid compressibility in which $\Delta\beta_s$ = 0 as $\beta_s = \beta_{s0} = 0.83 \times 10^{-10}$ Pa^{-1} (*blue line*).

We then plotted Brillouin shifts of virgin and CXL corneas as a function of hydration in the same plot (**Fig. 6.2**). Here, *Equation 6.7* was plotted (*red line*) with an identical Ω_0 of 6.49 GHz, while β_s was fit to the cross-linked data as a free parameter and best fit resulted to be 0.30×10^{-10} Pa^{-1}. It can be clearly seen that the experimental data

follows the model prediction well in both virgin and CXL conditions, i.e. the Brillouin shift changes as a function of hydration are consistent with the model in both conditions. Importantly, the CXL corneas have distinctly higher Brillouin shifts purely due to the mechanical response of the solid component(s) β_s independent of hydration. Specifically, the change in Brillouin shift due purely to CXL-induced solid mechanics modifications amount to ~100 MHz, which can be easily measured by current Brillouin clinical instruments.

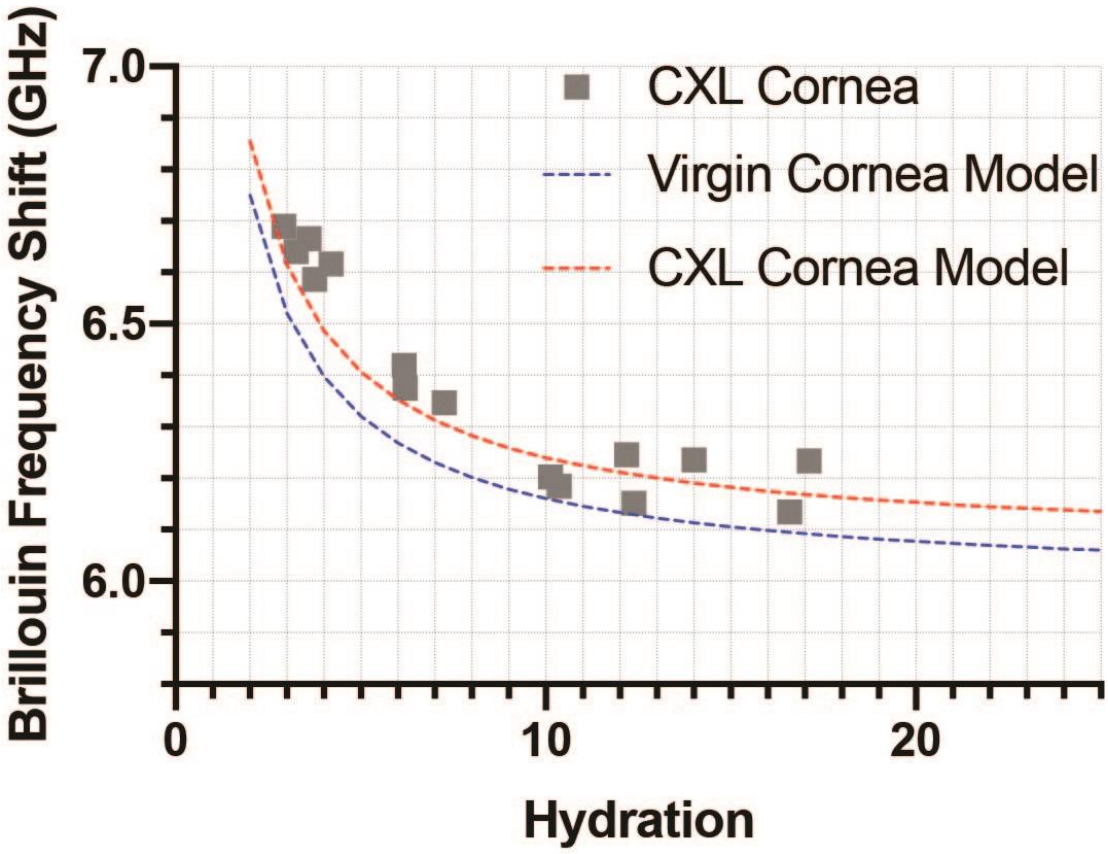

Figure 6.2: Average Brillouin frequency shift of the anterior of (n = 15) cross-linked corneas versus the measured hydration (*squares)*. Computational model of the relationship between Brillouin frequency shift, hydration, and solid compressibility in

which $\beta_s = 0.30 \times 10^{-10}$ Pa^{-1}, therefore, $\Delta\beta_s = 0.53\times 10^{-10}$ Pa^{-1}. The Virgin model in which $\Delta\beta_s = 0$ was identical represented (*blue line*).

6.3.2 Decoupling Elastic Modulus Dependence on Hydration and Solid Mechanics in CXL Procedures

To validate our theoretical model of the elastic modulus dependence on hydration and solid mechanics, 5 mm corneal samples were subjected to a variety of hydration and cross-linking conditions. **Figure 6.3** shows the theoretical equation (*Eqn. 6.12*) as well as experimental data using standard compression testing. The data presented here were virgin corneas, only varying in hydration while preserving a constant solid shear modulus. Therefore, *Equation 6.12* was fit to the experimental data by treating shear modulus of the solid matrix (μ_s) as a free parameter and solving for elastic modulus as a function of hydration.

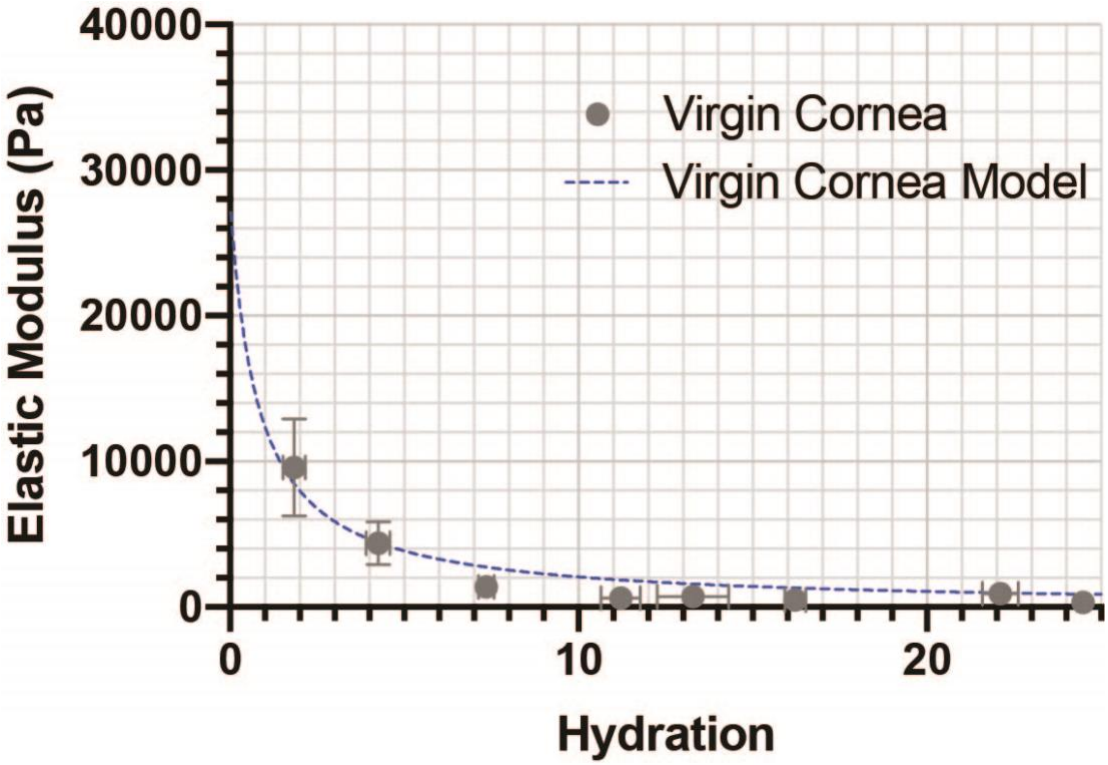

Figure 6.3: Elastic modulus versus hydration. The elastic moduli of n = 30 virgin corneas were averaged in hydration increments of three (circles). Computational model of the relationship between elastic modulus, hydration, and solid matrix was plotted in which μ_s = 9.3 kPa (*blue line*). The theoretical model fit our experimental data with an R^2 = 0.92. Error bars represent SEM.

By fitting for μ_s, we yielded a shear modulus of the solid matrix of 9.3 kPa within a virgin cornea. The clear fit to our experimental data validated the theoretical model in describing the relationship of elastic modulus at varying hydrations of the cornea. The solid shear modulus is within range of other measurements;[13,135] however, the exact value will depend on specific condition and measurement method. For example, the elastic moduli values found here differ than those found pre cross-linking in *Chapter 3*

and *4*. This can be explained by previously not accounting for hydration as well as differences in mechanical measurement protocols. Previously, virgin corneas referred to empirically controlled samples that did not undergo the cross-linking procedure. However, the hydrations of these corneas were not monitored yet can vary due to, for example, swelling during the transportation of the eyes and / or dehydration during exposure to the riboflavin / Dextran solution. As demonstrated by **Figure 6.3**, even subtle variations in hydration cause significant fluctuations of the elastic modulus. Additionally, the mechanical measurement techniques varied between chapters. We here reported elastic modulus between 1.5 and 4.5% strain while *Chapter 3* reported the modulus at 15% strain. In *Chapter 4*, although the modulus was reported over a similar strain, the measurement protocols differed in terms of strain rate and preloading conditions.

We then described the relationship between the elastic modulus of CXL corneas as a function of hydration and compared such to our virgin model (**Fig. 6.4**). Here, the model for cross-linked corneas was fit by again treating μ_s as a free parameter but keeping all other parameters consistent with the virgin model. Doing so yielded a μ_s for cross-linked corneas as 31.2 kPa. The difference in elastic modulus between the two lines can be attributed to the difference in shear modulus of the solid matrix (μ_s) between the virgin and cross-linked corneas. Cross-linking resulted in a 235% change in modulus compared to the virgin samples, agreeing with previously reported changes in shear modulus after cross-linking.[169] This change is greater than that measured

previously in *Chapter 3*; these differences can be explained by hydration monitoring and variances in experimental protocols as mentioned previously.

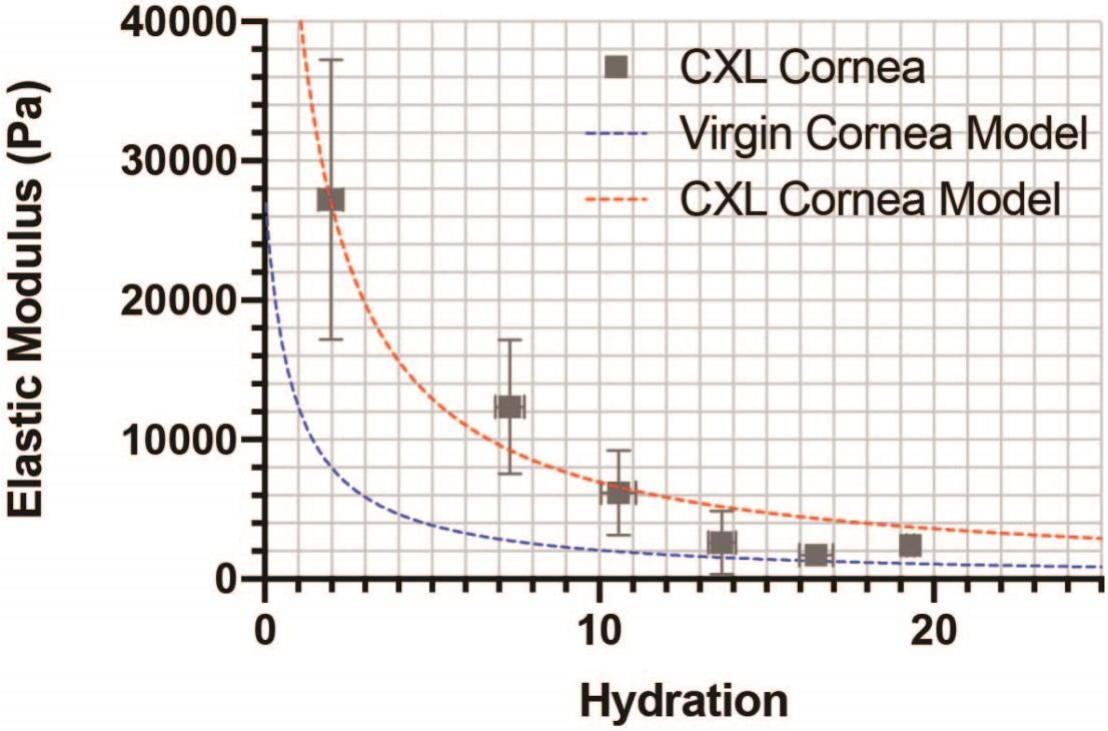

Figure 6.4: Average elastic modulus of (n = 22) cross-linked corneas versus the measured hydration (*squares)*. Samples were averaged across hydration increments of three. Computational model of the relationship between Brillouin frequency shift, hydration, and solid compressibility was plotted in which μ_s = 31.2kPa (*red line*). The virgin model in which μ_s = 9.3 kPa was represented (*blue line*). The cross-link model was in good agreement with the experimental data (R^2=0.95). Error bars represent SEM.

6.3.3 Dependence of Brillouin Modulus and Elastic Modulus on Corneal Hydration and Mechanical Properties of the Solid Matrix

We have confirmed our hypothesis that both Brillouin and elastic moduli are dependent on hydration and solid mechanics. Having validated a theoretical model for Brillouin modulus, $\mathrm{M}(H, B_s)$ and elastic modulus, $\mathrm{E}(H, \mu_s)$, we can explore a larger set of combinations to analyze the relationships with the underlying parameters comprehensively. **Figure 6.5** shows the Brillouin modulus derived using the measured frequency shift via *Equation 2.1* (**Fig. 6.5.A**) and the elastic modulus (**Fig.6.5.B**) as a combination of the hydration and solid mechanical properties of the cornea.

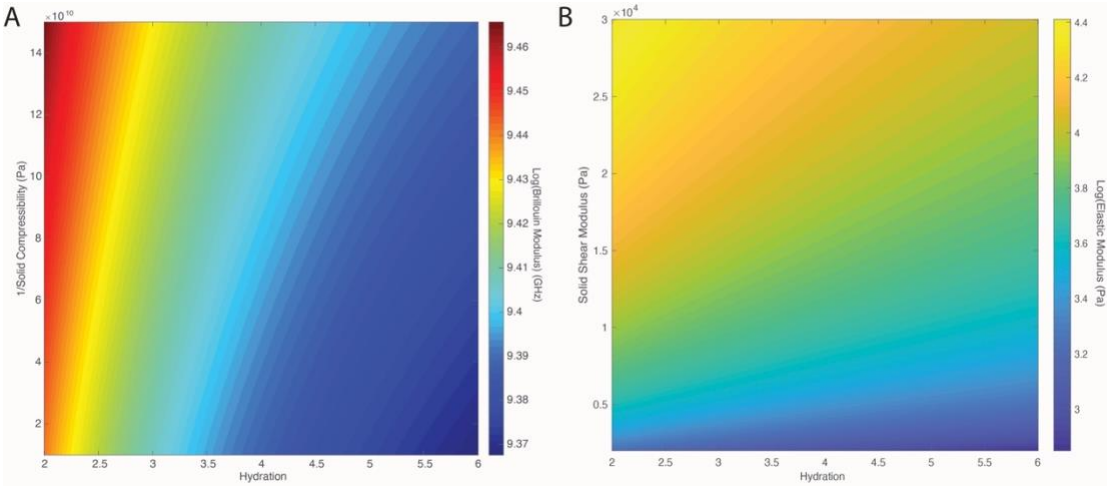

Figure 6.5: Three-dimensional relationship of **A**: Brillouin and **B**: elastic modulus on hydration and the solid matrix.

The above figures demonstrate the relationship of each modulus (*colors*) at vast combinations of hydration (*columns*) and solid mechanics (*rows*). For fair comparison, each figure covered a similar range of physiological hydration and solid mechanics as

per *Equation 6.2*. The wide range of solid mechanics was selected to include well-below physiological values as well as changes resulting from cross-linking procedures. As expected, both Brillouin frequency shift and elastic modulus were more sensitive to solid mechanical changes at lower hydration than at higher hydration, however, this sensitivity was more pronounced in frequency shift measurements. Additionally, as expected, Brillouin frequency shift was more sensitive to hydration than was elastic modulus. Both figures display a similar pattern in that the respective modulus monotonically decreases with larger hydration and monotonically increases with larger modulus of the solid component, leading to the diagonal-looking patterns observed above. The common dependence on hydration and solid mechanics thus explains the previously found empirical correlations between the two moduli. Previously, solid mechanics and hydration of the cornea were experimentally varied in procedures such as cross-linking. Under such procedures, the hydration of the sample was, at best, normalized through empirical, experimental controls or, at worst, unregulated and subjected to the natural hydration / dehydration of procedures. However, these experiments only measured the overall modulus information rather than the underlying parameters. Therefore, it could not be deciphered if changes in modulus were due to solid mechanical changes or hydration fluctuations inherent to the procedure. While imperfect, to demonstrate consistency with previous correlations, we too can obtain a log-log relationship between Brillouin and elastic modulus using our model. To do so, we converted the solid matrix component found in Brillouin frequency shift ($\frac{1}{\beta_s}$) to the solid matrix component used in elastic modulus (μ_0) using an expanded form of *Equation 6.2*:

$$M = \frac{1}{\beta_s} = \frac{2\mu_s(1-\nu)}{1-2\nu} \qquad (Eqn.\ 6.13)$$

Using this equation, we are making the assumption for Poisson ratio that reflects a nearly incompressible solid matrix. Now, we were able to calculate a Brillouin modulus and elastic modulus at any combination of hydration and solid shear parameters. In order to replicate previous experimental situations, for example at a controlled hydration, we constrained our model to only vary solid mechanics while fixing hydration to a physiological value (H = 3.2). The output from *Equations 6.7* and *6.12* were plotted on a log scale and fit to: log(M) = m*log(E) + b (**Figure 6.6**). Here, the log-log correlation yielded the linear fit (R^2 = 0.99): log(E) = 0.037 log(M) + 9.29.

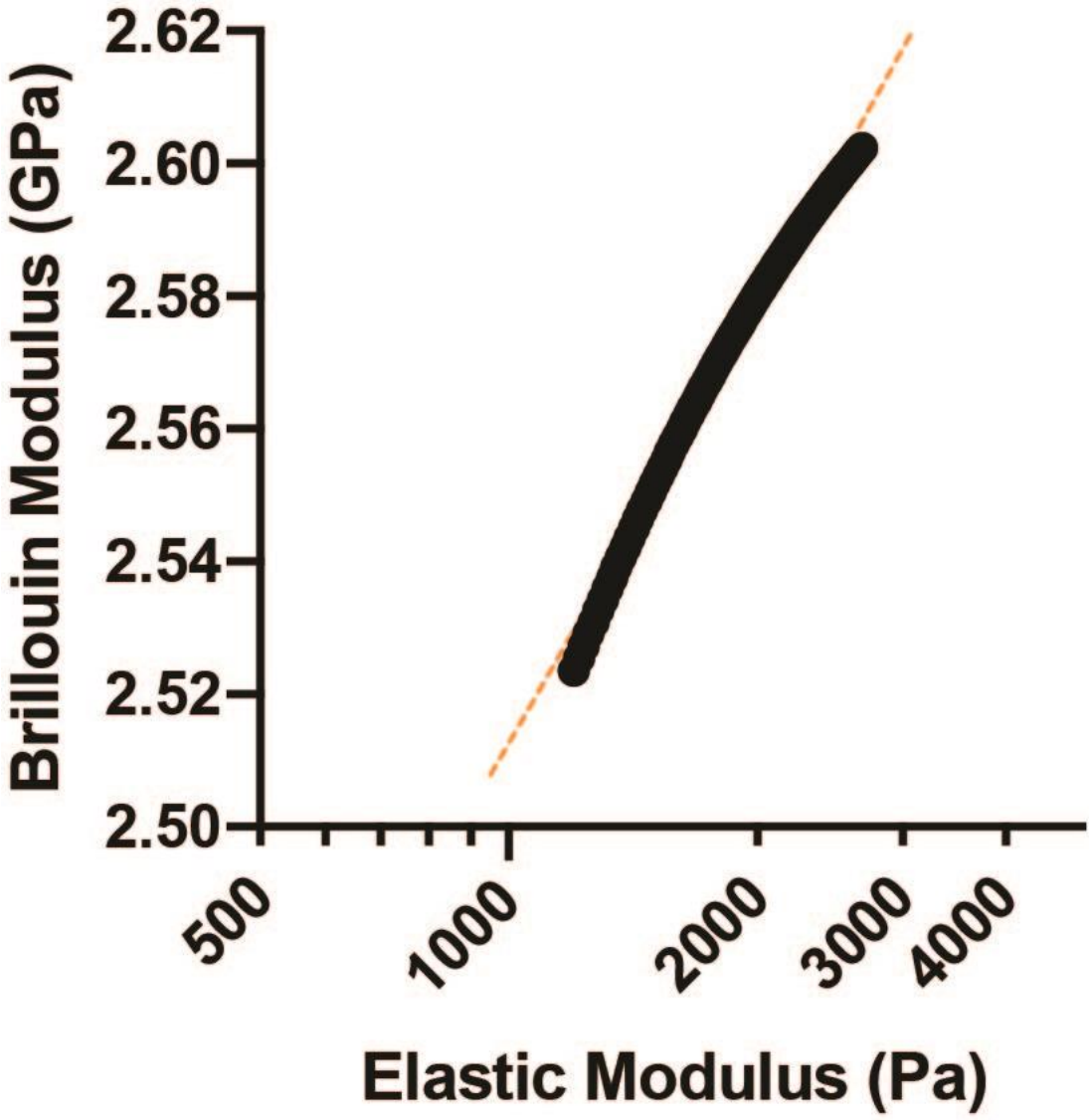

Figure 6.6: Log-log correlation between Brillouin derived longitudinal modulus. Our model output (*black*) was plotted with log-log line of best fit (*orange*).

The correlation found here is consistent with the range found previously, i.e. a log-log relationship where m = 0.033, b = 9.31 GPa by Shao *et. al.*[98] and a percent change relationship where m = 0.07 by Webb *et. al.*[101] The consistency between our model and previous experimental data clarifies why a log-log relationship was experimentally

observed before. The discrepancies between values can be explained by the inability to experimentally control hydration. Therefore, even in tightly controlled-settings, subtle fluctuations in hydration will affect the Brillouin and elastic modulus measurements.

6.3.4 Relating Brillouin Frequency Shift to Elastic Modulus of the Cornea

At this time, we have derived a quantitative relationship for Brillouin frequency shift depending on hydration and solid compressibility, $\Omega(H, B_s)$, (*Eqn. 6.7*) as well as for elastic modulus depending on hydration and solid shear matrix, $\mathrm{E}(H, \mu_s)$ (*Eqn. 6.12*). Using *Equation 6.13*, we can express both relationships in terms of solid shear modulus, yielding Brillouin frequency shift, $\Omega(H, \mu_s)$, and elastic modulus, $\mathrm{E}(H, \mu_s)$.

Despite the clear correlations shown in the previous sections, it is evident that Brillouin frequency measurements alone are insufficient to yield a unique value of elastic modulus. As shown in **Figure 6.5**, the dependencies of $\Omega(H, \mu_s)$ and $\mathrm{E}(H, \mu_s)$ are different. Therefore, there exists different combinations of $\Omega(H, \mu_s)$ that yield the same elastic modulus. However, Brillouin frequency shift paired with either hydration or solid shear modulus would yield two equations with two unknowns, thereby, allowing for the solving of elastic modulus. Importantly, hydration and Brillouin frequency shift can be measured in the clinics. Therefore, we combine *Equations 6.7* and *6.12* and rewrite the expression for elastic modulus in terms of Brillouin frequency shift and hydration. The resulting relationship was plotted (**Figure 6.7**) over a physiologically relevant range of hydration and frequency shift.

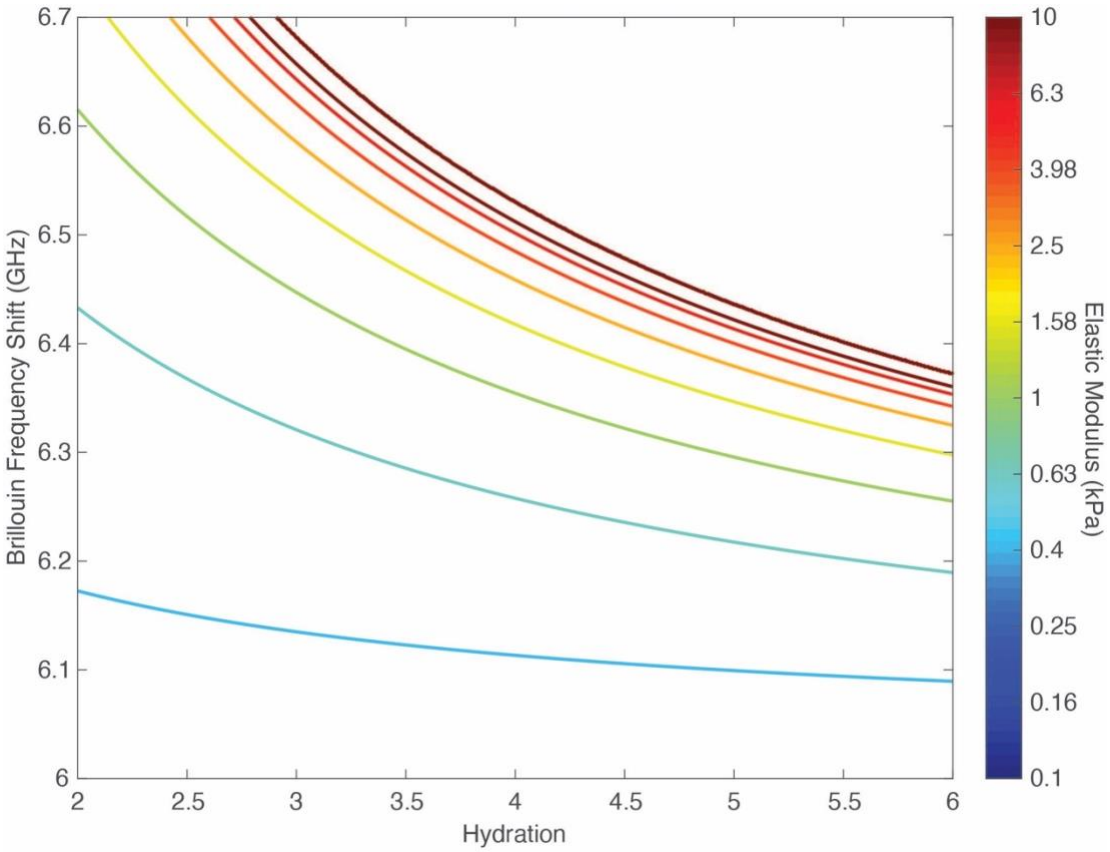

Figure 6.7: Correlation between Brillouin frequency shift, hydration, and elastic modulus.

Figure 6.7 depicts the various combinations of hydration and Brillouin frequency shift leading to an elastic modulus measurement. Each isoline corresponds to a different elastic modulus. Consistent with our previous observations, it is clear a single Brillouin frequency shift corresponds to different values of elastic modulus due to the distinct relationships with the underlying parameters. One can obtain the same elastic modulus at high Brillouin frequency shift and low hydration or a low Brillouin frequency shift and high hydration. Interesting, at lower elastic moduli, the isolines are nearly horizontal, indicating that the Brillouin shift relationship to elastic modulus is less

sensitive to changes in hydration. Instead, at higher values of elastic modulus, knowledge of the hydration state is clearly needed as the Brillouin-elastic relationship becomes much more sensitive to changes in hydration. The precision of our model is dependent on the precision of both of our parameters: Brillouin frequency shift and hydration. At a hydration of 3.2 (physiological level), our model has an elastic modulus precision of 0.291 kPa based on Brillouin measurements corresponding to our *in vivo* Brillouin microscope precision of 10 MHz. However, such precision degrades at higher hydration. At a hydration of 4.0 (severe Fuchs' Dystrophy level), the precision becomes 3.0 kPa based on this same Brillouin microscope precision. At a Brillouin frequency shift of 6.5 GHz (virgin physiological level), our model has an elastic modulus precision of 0.115 kPa based on hydration measurements corresponding to clinical ultrasound pachymetry precision of <10 μm (H = 0.074). In all regimes, though, it is evident that our derived relationships establish a method to extract accurate elastic modulus information from hydration and Brillouin shift measurements.

6.4 Discussion

We first constructed a theoretical model for Brillouin frequency shift that depends on hydration and solid mechanical properties independent of hydration. To do so, we constructed a biphasic model of the cornea consisting solely of a solid collagen matrix and water. To experimentally test our model, we measured the frequency shift of virgin and cross-linked corneas at a variety of hydration conditions as cross-linking was assumed to increase the mechanical properties of the collagen matrix. Our experimental data agreed with our theoretical model, validating the quantified

relationship between Brillouin frequency shift, hydration, and solid mechanical compressibility. Next, we theoretically and experimentally modeled the relationship of elastic modulus, hydration, and the solid matrix represented through solid shear modulus. Cross-linking has been shown to increase the shear modulus of the cornea with a particular increase in shear within the anterior stroma.[169] Therefore, like in the model for Brillouin frequency shift, we accounted for cross-linking by treating the solid mechanical component of our relationship as a free parameter to be fit. The theoretical model here agreed with experimental data, validating our relationship of elastic modulus, hydration, and solid shear modulus. Then, by converting the compressibility of the solid component to shear modulus, we were able to redefine elastic modulus in terms of Brillouin frequency shift and hydration.

The results presented here address the numerous shortcomings with clinical measurements of elastic modulus. Devices used to measure the elastic modulus of the cornea revolve around elastography techniques, measuring the displacement of the cornea in response to an external force.[61,66,72,170] Using the cross-sectional displacement response as input, Finite Element Modeling (FEM) can be employed to indirectly yield global corneal mechanical properties. However, these devices displace the cornea with a singular, centralized air puff and are limited to two dimensional cross-sections due to acquisition time. As ectatic disorders are characterized with spatially varying mechanical properties, the global and cross-sectional nature of current devices provide mixed results and prevent optimal keratoconus diagnostics.[171,172] More so, none of these devices are approved in the United States for biomechanical

measurements clinically. Our results present a method to yield elastic modulus from hydration and Brillouin shift measurements. Most notably, hydration and Brillouin shift both are currently performed noninvasively with spatial resolution *in vivo*. Therefore, using this technique, elastic modulus can be noninvasively extracted in three dimensions in the clinic.

There are a number of limitations in our study. First, the cornea, like most biological material, is viscoelastic.[135,173,174] Therefore, the frequency at which stress vs strain was performed will greatly affect the derived elastic modulus. The relationship described here is only at a single frequency but will vary with quasi-state frequency measurements. Additionally, the cornea is mechanically anisotropic. The results presented here are correlated along a single probing direction, measuring the modulus at perpendicular angles to the collagen fibers. Physiological stresses, for example that felt under intraocular pressure, greatly stresses the fibers in the parallel direction. In order to obtain a full, three-dimensional conversion from Brillouin to elastic modulus, future studies will be repeated at varying probing angles. For example, rather than the compression testing performed here, tensile testing may be employed to correlate a Brillouin shift measured parallel to the fiber direction.

6.5 Conclusion

There currently exists a clinical shortcoming of measuring *in vivo* corneal elastic modulus. While Brillouin microscopy could fill this gap, we first needed to understand

the relationship between Brillouin and elastic modulus. To do this, experimental and theoretical models were constructed describing the dependence of Brillouin and elastic moduli on hydration and solid components. This model was especially applicable for the cornea which is overwhelmingly biphasic being constructed of a solid collagen matrix and internally saturated with water / aqueous solution. Once independently constructed, the models were related using a general conversion factor between shear and compressibility. Finally, a quantitative relationship of elastic modulus was written in terms of hydration and Brillouin shift, two clinically measured parameters. Therefore, the results presented here allow for a separation of hydration dependent and independent contributions of elastic and Brillouin modulus. This distinction permits a needed detection of the long-term stiffening alterations associated with disease and treatments. More so, our relationship can be used to discern the spatially varying elastic modulus of the cornea The current study was performed *ex vivo*, however, future steps will include testing our model *in vivo* to predict long term shape changes associated with alterations of corneal mechanics.

CHAPTER 7: OUTLOOK AND SCIENTIFIC CONTRIBUTIONS

7.1 Summary of Scientific Contributions

The results from my work reshaped the understanding of clinical procedures. Corneal cross-linking is an accepted treatment for ectatic disorders by increasing the stiffness of the cornea. In short, the entire cornea is saturated with a photosensitizer, riboflavin, for 30 minutes. The cornea is the globally subjected to UV-A light for 30 minutes to begin a cascade of photochemical reactions, resulting in an increase of covalent bonds between adjacent collagen fibers within the cornea. As indicated, this is a lengthy and global procedure. To address the lengthy time requirement, researchers and clinicians have increased interest in accelerating cross-linking by, while keeping the same energy dose, decreasing the required time of UV-A exposure by increasing the required power of the light. However, results of accelerated CXL were mixed as no method could properly assess the stiffening affects in three dimensions. In Chapter 3, we used Brillouin microscopy to perform the first three-dimensional characterization of accelerated cross-linked corneas and comparison to standard cross-linked samples. Finding sub-optimal stiffening of accelerated CXL, our results suggested accelerating the procedure did not allow oxygen to diffuse back into the cornea; a process required for CXL to occur. In addition to bettering the understanding of cross-link as a whole, our results informed physicians of the particular effects of accelerating the procedure clinically. The work towards characterizing the effects of accelerated cross-linking

using Brillouin microscopy was published in the *Journal of Cataract and Refractive Surgery* in 2017 and has become one of the journal's top 10 most cited papers since its publication date. Additionally, in 2017, I presented the work at two different conferences including the Biomedical Engineering Society annual meeting in Phoenix, AZ.

In addition to accelerating the procedure, localizing the UV-A irradiation to the area of compromised stiffness has been shown to increase the refractive recovery of patients as well as decrease the unwanted side-effects associated with the procedure. However, no method could completely measure the mechanical effects of a localized procedure until now. In Chapter 4, we used Brillouin microscopy to observe the stiffening results of localized CXL in three dimensions. Interestingly, a significant transition zone between the section of the cornea exposed to UV-A and the section masked from UV-A was found. The results show a radius of stiffening outside the irradiated zone, suggesting potential movement of reactive species during the cross-linking procedure. More so, the results inform mechanical modelers and practicing physicians of the expanded stiffening effects of a localized cross-linking procedure; allowing for a better understanding of what is necessary to completely personalize the treatment. The findings of Chapter 4 have been published in the *Journal of Refractive Surgery* in 2019 and presented at 4 different meetings including at the Association for Research in Vision and Ophthalmology annual meeting in Honolulu, HI.

As demonstrated, Brillouin microscopy has emerged as a useful tool to measure corneal mechanics. However, the parameters in which affect Brillouin measurements, hydration and solid mechanical modulus, were not yet fully understood. To better understand the contributions of hydration and the solid modulus on Brillouin measurements, we first focused on detecting mechanical anisotropy within the cornea – a property purely reflected on characteristics of the solid matrix rather than isotropic water. In Chapter 5, our group not only became the first to detect mechanical anisotropy within the cornea using Brillouin microscopy, but also to determine the biphasic manner in which the solid matrix and hydration contribute to Brillouin frequency shift. The implications of these results validate Brillouin microscopy as a tool to clinically measure hydration, which naturally changes as well as through disorders such as Fuchs' Dystrophy, and the solid matrix, which varies as a result of a number of natural disorders such as keratoconus and treatments such as cross-linking. These results have been published in *Translational Vision & Technology* in 2020 and presented at 4 national and international conferences including the Photo-Optical Instrumentation Engineers annual conference in 2021.

Previously, Brillouin measurements required empirical calibrations to extract elastic modulus because a fundamental understanding of the two had not yet been established. More so, these correlations between Brillouin and elastic moduli were imperfect as they only measured the overall modulus information rather than the underlying parameters. Therefore, these measurements could not decipher if changes in modulus were due to solid mechanical changes or hydration fluctuations within the cornea. In Chapter 6, we

addressed these shortcomings by quantitatively defining the contributions of hydration and solid component on Brillouin shift and elastic modulus. Using these quantitative relationships, we were then able to yield an equation for elastic modulus that depends on hydration and Brillouin shift. Notably, Brillouin shift and hydration are measured in a clinical setting. Therefore, our relationship allows elastic modulus to be measured noninvasively in the clinic, ultimately allowing for a better understanding of Brillouin and elastic measurements, a more accurate characterization of cross-linking procedures, and improved diagnostics of various diseases.

In summary, my graduate research resulted in 4 first-authored publications and 1 publication as a contributing author in field-leading journals, as well as 1 publication in preparation. I am a co-owner of a filed provisional patent on the quantitative relationship between Brillouin measurements and elastic modulus. I presented my research, both orally and via poster format, at 10 international and nation conferences. I was received 7 different awards for my research, including The Fischell Fellowship in Biomedical Engineering, Fellowship, as well as work outside my research throughout the scientific community, including being named a Silver Reviewer by the Journal of Refraction Surgery.

A list of scientific contributions is summarized below:

1. Chapter 3
    a. First three-dimensional mechanical characterization of accelerated corneal cross-linking

i. Accelerated CXL results in suboptimal mechanical stiffening due first to a compromise within the posterior section

b. First log-log correlation between Brillouin and elastic modulus within the cornea

i. Underlying parameters of Brillouin and elastic measurements are similar within the cornea

ii. Brillouin microscopy is capable of measuring spatially varying changes to corneal mechanics

2. Chapter 4

a. First three-dimensional mechanical characterization of localized corneal cross-linking

i. Mechanical transition zone exists between areas of the cornea exposed to and masked from UV-A exposure

3. Chapter 5

a. First detection of mechanical anisotropy within an intact cornea using Brillouin microscopy

i. Brillouin microscopy is sensitive to both hydration-dependent and -independent changes within the cornea

b. The sensitivity of Brillouin microscopy to the solid collagen matrix was independent of hydration through 96% water volume fraction

i. Brillouin microscopy corneal measurements can be modeled as biphasic

4. Chapter 6

a. Established a quantitative relationship describing Brillouin frequency shift depending on hydration and solid collagen matrix
b. Established a quantitative relationship describing elastic modulus depending on hydration and solid collagen matrix
c. Derived a quantitative model for elastic modulus using Brillouin frequency shift and hydration, two clinically available parameters

7.2 Future Directions

The relationship for elastic modulus depending on Brillouin frequency shift and hydration was yielded through the combination of two, theoretically derived and experimentally verified models $\Omega(H, B_s)$ and $\mathrm{E}(H, \mu_s)$. To better relate the two solid matrix components, $\Omega(H, B_s)$ was converted to $\Omega(H, \mu_s)$ using an approximation described in *Equation 6.13*. Doing so allowed the derivation of our final relationship $\mathrm{E}(\Omega, H)$, however, this relationship has not yet been experimentally verified. To do so, we will conduct an experimental test of our model. In short, corneal buttons will be extracted and undergo a randomized cross-linking protocol followed by a randomized hydration protocol. Then, the hydration and Brillouin frequency shift will be measured and input into our model, yielding a theoretical elastic modulus. The same cornea will then undergo a compression test to yield an actual elastic modulus, which will be compared to our theoretical modulus. The comparison of actual and theoretical moduli will verify our relationship in a clinically practical method and demonstrate the precision and sensitivity of our model.

The relationships described here were based on porcine corneas. The fundamental composition of porcine corneas is similar to human corneas, however, human corneas display different mechanical properties (i.e. human corneas are stiffer than porcine corneas). For these reasons, we believe our model will accurately explain human corneas once the constant values (*Table 6.1*) are updated. In the future, this updated model will be tested using human corneal samples. Additionally, both the Brillouin measurements and elastic moduli were probed perpendicular to the collagen fibers. Corneas are mechanically anisotropic due to the organizational structure of their collagen matrix. More so, *in vivo* corneas, due to intraocular pressure, will exhibit a stress ~10 fold higher in the tangential direction compared to the radial. In order to establish complete clinical relevance, a relationship between Brillouin measurements and elastic modulus when probed parallel to collagen fibers is needed. To do so, we will measure Brillouin shift values by tilting the cornea 90° about the probing laser and yield elastic modulus values by undergoing tensile tests parallel to the collagen fibers. The differences between the model found within this dissertation and the model found at this new angle will reflect the clinical need to monitor the probing direction and allow for a more comprehensive relationship of $\mathrm{E}(\Omega, H)$.

In addition to direct clinical relevance, a three-dimensional map of corneal mechanical properties paves the way for accurate, personalized predictive modeling. The simplified equation $F = E \times U$, in which F is the force, E is the mechanical behavior, and U is the displacement, is the premise of Finite Element (FE) modeling. Current

modeling techniques use the known air puff force (F) and resulting corneal displacement (U) to back-calculate a global elastic modulus (E). Here, we demonstrated a method to yield mechanical measurements without the need for FE modeling. Therefore, we can use the localized, three-dimensional mechanical measurements (E) extracted via Brillouin Microscopy and the intraocular pressure over time (F) as input to direct FE modeling to predict long-term morphological behavior (U) of the cornea. Predicting morphological behavior could lead to personalized refractive / CXL procedures and more accurate screening / diagnostics of corneal disorders.

BIBLIOGRAPHY

1. Waring GO, Bourne WM, Edelhauser HF, Kenyon KR. The Corneal Endothelium: Normal and Pathologic Structure and Function. *Ophthalmology*. 1982;89(6):531-590.
2. Chen J, Li Z, Zhang L, et al. Descemet's Membrane Supports Corneal Endothelial Cell Regeneration in Rabbits. *Sci Rep*. 2017;7(1):1-13.
3. Wilson SE. Bowman's layer in the cornea– structure and function and regeneration. *Exp Eye Res*. 2020;195:108033.
4. Reinstein DZ, Archer TJ, Gobbe M, Silverman RH, Coleman DJ. Stromal thickness in the normal cornea: Three-dimensional display with artemis very high-frequency digital ultrasound. *J Refract Surg*. 2009;25(9):776-786.
5. Blackburn BJ, Jenkins MW, Rollins AM, Dupps WJ. A review of structural and biomechanical changes in the cornea in aging, disease, and photochemical crosslinking. *Front Bioeng Biotechnol*. 2019;7(MAR):66.
6. Nguyen TM, Aubry JF, Fink M, Bercoff J, Tanter M. In vivo evidence of porcine cornea anisotropy using supersonic shear wave imaging. *Investig Ophthalmol Vis Sci*. 2014;55(11):7545-7552.
7. DelMonte DW, Kim T. Anatomy and physiology of the cornea. *J Cataract Refract Surg*. 2011;37(3):588-598.
8. Roberts CJ, Liu J, Ambrosio R (Renato). *Corneal Biomechanics : From Theory to Practice*.
9. Winkler M, Chai D, Kriling S, et al. Nonlinear Optical Macroscopic Assessment of 3-D Corneal Collagen Organization and Axial Biomechanics.

Investig Opthalmology Vis Sci. 2011;52(12):8818.

10. McClelland RE, Dennis R, Reid LM, Stegemann JP, Palsson B, Macdonald JM. Tissue Engineering. In: *Introduction to Biomedical Engineering*. Elsevier Inc.; 2011:273-357.
11. Scarcelli G, Kling S, Quijano E, Pineda R, Marcos S, Yun SH. Brillouin Microscopy of Collagen Crosslinking: Noncontact Depth-Dependent Analysis of Corneal Elastic Modulus. *Investig Opthalmology Vis Sci*. 2013;54(2):1418.
12. Randleman JB, Dawson DG, Grossniklaus HE, McCarey BE, Edelhauser HF. Depth-dependent cohesive tensile strength in human donor corneas: Implications for refractive surgery. *J Refract Surg*. 2008;24(1):85-89.
13. Petsche SJ, Chernyak D, Martiz J, Levenston ME, Pinsky PM. Depth-dependent transverse shear properties of the human corneal stroma. *Investig Ophthalmol Vis Sci*. 2012;53(2):873-880.
14. Luo L, Liu Z, Chen J, et al. Normal human keratocyte density and corneal thickness by confocal microscopy in vivo. *Chinese Ophthalmic Res*. 2004;22(5):512-515.
15. Scarcelli G, Pineda R, Yun SH. Brillouin Optical Microscopy for Corneal Biomechanics. *Investig Opthalmology Vis Sci*. 2012;53(1):185.
16. Kerautret J, Colin J, Touboul D, Roberts C. Biomechanical characteristics of the ectatic cornea. *J Cataract Refract Surg*. 2008;34(3):510-513.
17. *Eye Banking Statistical Report*.; 2014.
18. Scarcelli G, Besner S, Pineda R, Kalout P, Yun SH. In Vivo Biomechanical Mapping of Normal and Keratoconus Corneas. *JAMA Ophthalmol*.

2015;133(4):480.

19. Godefrooij DA, Gans R, Imhof SM, Wisse RPL. Nationwide reduction in the number of corneal transplantations for keratoconus following the implementation of cross-linking. *Acta Ophthalmol*. 2016;94(7):675-678.
20. Wollensak G, Spoerl E, Seiler T. Stress-strain measurements of human and porcine corneas after riboflavin–ultraviolet-A-induced cross-linking. *J Cataract Refract Surg*. 2003;29(9):1780-1785.
21. Torres Netto EA, Al-Otaibi WM, Hafezi NL, et al. Prevalence of keratoconus in paediatric patients in Riyadh, Saudi Arabia. *Br J Ophthalmol*. 2018;102(10):1436-1441.
22. Hjortdal JØ, Møller-Pedersen T, Ivarsen A, Ehlers N. Corneal power, thickness, and stiffness: Results of a prospective randomized controlled trial of PRK and LASIK for myopia. *J Cataract Refract Surg*. 2005;31(1):21-29.
23. Karseras AG, Ruben M. Aetiology of keratoconus. *Brit J Ophthal*. 1976;6:522.
24. Zimmermann DR, Fischer RW, Winterhalter KH, Witmer R, Vaughan L. Comparative studies of collagens in normal and keratoconus corneas. *Exp Eye Res*. 1988;46(3):431-442.
25. Sawaguchi S, Yue BY, Sugar J, Gilboy JE. Lysosomal enzyme abnormalities in keratoconus. *Arch Ophthalmol (Chicago, Ill 1960)*. 1989;107(10):1507-1510.
26. Roberts CJ, Dupps WJ. Biomechanics of corneal ectasia and biomechanical treatments. *J Cataract Refract Surg*. 2014;40(6):991-998.
27. Girard MJA, Dupps WJ, Baskaran M, et al. Translating ocular biomechanics

into clinical practice: Current state and future prospects. *Curr Eye Res*. 2015;40(1):1-18.

28. Shao P, Eltony AM, Seiler TG, et al. Spatially-resolved Brillouin spectroscopy reveals biomechanical changes in early ectatic corneal disease and post-crosslinking in vivo. *arXiv*. February 2018.

29. Vinciguerra R, Ambrósio R, Roberts CJ, Azzolini C, Vinciguerra P. Biomechanical characterization of subclinical keratoconus without topographic or tomographic abnormalities. *J Refract Surg*. 2017;33(6):399-407.

30. Saad A, Lteif Y, Azan E, Gatinel D. Biomechanical properties of keratoconus suspect eyes. *Investig Ophthalmol Vis Sci*. 2010;51(6):2912-2916.

31. Vinciguerra R, Ambrósio R, Elsheikh A, et al. Detection of keratoconus with a new biomechanical index. *J Refract Surg*. 2016;32(12):803-810.

32. Abahussin M, Hayes S, Cartwright NEKK, et al. 3D collagen orientation study of the human cornea using X-ray diffraction and femtosecond laser technology. *Investig Ophthalmol Vis Sci*. 2009;50(11):5159-5164.

33. Scarcelli G, Kim P, Yun SH. In Vivo Measurement of Age-Related Stiffening in the Crystalline Lens by Brillouin Optical Microscopy. *Biophysj*. 2011;101:1539-1545.

34. Eyre D. Collagen Cross-Linking Amino Acids. *Methods Enzymol*. 1987;144(C):115-139.

35. Albon J, Karwatowski WSS, Avery N, Easty DL, Duance VC. Changes in the collagenous matrix of the aging human lamina cribrosa. *Br J Ophthalmol*. 1995;79(4):368-375.

36. Spoerl E, Huhle M, Seiler T. Induction of cross-links in corneal tissue. *Exp Eye Res*. 1998;66(1):97-103.

37. O'Brart DPS. Corneal collagen cross-linking: a review. *J Optom*. 2014;7(3):113-124.

38. Dendukuri D, Panda P, Haghgooie R, Kim JM, Hatton TA, Doyle PS. Modeling of Oxygen-Inhibited Free Radical Photopolymerization in a PDMS Microfluidic Device. *Macromolecules*. 2008;(22):21.

39. Kamaev P, Friedman MD, Sherr E, Muller D. Photochemical Kinetics of Corneal Cross-Linking with Riboflavin. *Investig Opthalmology Vis Sci*. 2012;53(4):2360.

40. McCall AS, Kraft S, Edelhauser HF, et al. Mechanisms of Corneal Tissue Cross-linking in Response to Treatment with Topical Riboflavin and Long-Wavelength Ultraviolet Radiation (UVA). *Investig Opthalmology Vis Sci*. 2010;51(1):129-138.

41. Ryu A, Naru E, Arakane K, et al. Cross-linking of collagen by singlet oxygen generated with UV-A. *Chem Pharm Bull (Tokyo)*. 1997;45(8):1243-1247.

42. Wollensak G, Spoerl E, Seiler T. Riboflavin/ultraviolet-A-induced collagen crosslinking for the treatment of keratoconus. *Am J Ophthalmol*. 2003;135(5):620-627.

43. Çerman E, Toker E, Ozarslan Ozcan D. Transepithelial versus epithelium-off crosslinking in adults with progressive keratoconus. *J Cataract Refract Surg*. 2015;41(7):1416-1425.

44. Kissner A, Spoerl E, Jung R, Spekl K, Pillunat LE, Raiskup F.

Pharmacological modification of the epithelial permeability by benzalkonium chloride in UVA/Riboflavin corneal collagen cross-linking. *Curr Eye Res*. 2010;35(8):715-721.

45. Caporossi A, Mazzotta C, Baiocchi S, Caporossi T, Paradiso AL. Transepithelial corneal collagen crosslinking for keratoconus: Qualitative investigation by in vivo HRT II confocal analysis. *Eur J Ophthalmol*. 2012;22(SUPPLEMENT N. 7):81-88.

46. Said DG, Elalfy MS, Gatzioufas Z, et al. Collagen Cross-Linking with Photoactivated Riboflavin (PACK-CXL) for the Treatment of Advanced Infectious Keratitis with Corneal Melting. *Ophthalmology*. 2014;121(7):1377-1382.

47. Mita M, Waring GO, Tomita M. High-irradiance accelerated collagen crosslinking for the treatment of keratoconus: Six-month results. *J Cataract Refract Surg*. 2014;40(6):1032-1040.

48. Wernli J, Schumacher S, Spoerl E, Mrochen M. The Efficacy of Corneal Cross-Linking Shows a Sudden Decrease with Very High Intensity UV Light and Short Treatment Time. *Investig Opthalmology Vis Sci*. 2013;54(2):1176.

49. Sinha Roy A, Dupps WJ, Jr. Patient-specific computational modeling of keratoconus progression and differential responses to collagen cross-linking. *Invest Ophthalmol Vis Sci*. 2011;52(12):9174-9187.

50. Cassagne M, Pierné K, Galiacy SD, Asfaux-Marfaing M-P, Fournié P, Malecaze F. Customized Topography-Guided Corneal Collagen Cross-linking for Keratoconus. *J Refract Surg*. 2017;33(5):290-297.

51. Nordström M, Schiller M, Fredriksson A, Behndig A. Refractive improvements and safety with topography-guided corneal crosslinking for keratoconus: 1-year results. *Br J Ophthalmol*. 2017;101(7):920-925.

52. Seiler TG, Fischinger I, Koller T, Zapp D, Frueh BE, Seiler TG. Customized Corneal Cross-linking: One-Year Results. *Am J Ophthalmol*. 2016;166:14-21.

53. Yu J, Bao F, Feng Y, et al. Assessment of Corneal Biomechanical Behavior Under Posterior and Anterior Pressure. *J Refract Surg*. 2013;29(1):64-71.

54. Elsheikh A, Wang D, Brown M, Rama P, Campanelli M, Pye D. Assessment of Corneal Biomechanical Properties and Their Variation with Age. *Curr Eye Res*. 2007;32(1):11-19.

55. Khaw PT, Shah P, Elkington AR. Glaucoma--1: diagnosis. *BMJ*. 2004;328(7431):97-99.

56. Ko MWL, Leung LKK, Lam DCC, Leung CKS. Characterization of corneal tangent modulus in vivo. *Acta Ophthalmol*. 2013;91(4):263-269.

57. Palko JR, Tang J, Cruz Perez B, Pan X, Liu J. Spatially heterogeneous corneal mechanical responses before and after riboflavin-ultraviolet-A crosslinking. *J Cataract Refract Surg*. 2014;40(6):1021-1031.

58. Elsheikh A, Alhasso D. Mechanical anisotropy of porcine cornea and correlation with stromal microstructure. *Exp Eye Res*. 2009;88(6):1084-1091.

59. Elsheikh A, Brown M, Alhasso D, Rama P, Campanelli M, Garway-Heath D. Experimental assessment of corneal anisotropy. *J Refract Surg*. 2008;24(2):178-187.

60. Worthington KS, Wiley LA, Bartlett AM, et al. Mechanical properties of

murine and porcine ocular tissues in compression. *Exp Eye Res*. 2014;121:194-199.

61. Luce DA. Determining in vivo biomechanical properties of the cornea with an ocular response analyzer. *J Cataract Refract Surg*. 2005;31(1):156-162.
62. Biomechanical eye model and measurement setup for investigating accommodating intraocular lenses. *Z Med Phys*. 2013;23(2):144-152.
63. Myers KJ, Lalle P, Litwak A, Campbell S, Ballinger R, Grolman B. XPERT NCT--a clinical evaluation. *J Am Optom Assoc*. 1990;61(11):863-869.
64. Fontes BM, Ambrósio R, Velarde GC, Nosé W. Ocular response analyzer measurements in keratoconus with normal central corneal thickness compared with matched normal control eyes. *J Refract Surg*. 2011;27(3):209-215.
65. Mohammadpour M, Etesami I, Yavari Z, Naderan M, Abdollahinia F, Jabbarvand M. Ocular response analyzer parameters in healthy, keratoconus suspect and manifest keratoconus eyes. *Oman J Ophthalmol*. 2015;8(2):102-106.
66. Hong J, Xu J, Wei A, et al. A new tonometer-the corvis ST tonometer: Clinical comparison with noncontact and goldmann applanation tonometers. *Investig Ophthalmol Vis Sci*. 2013;54(1):659-665.
67. Correia FF, Ramos I, Roberts CJ, Steinmueller A, Krug M, Ambrósio R. Impacto da pressão na câmara artificial e das propriedades do material sobre a resposta de deformação de modelos de córnea medido por imagem de Scheimpflug ultradinâmica de alta velocidade. *Arq Bras Oftalmol*. 2013;76(5):278-281.

68. Kling S, Bekesi N, Dorronsoro C, Pascual D, Marcos S. Corneal Viscoelastic Properties from Finite-Element Analysis of In Vivo Air-Puff Deformation. Boote C, ed. *PLoS One*. 2014;9(8):e104904.

69. Sinha Roy A, Kurian M, Matalia H, Shetty R. Air-puff associated quantification of non-linear biomechanical properties of the human cornea in vivo. *J Mech Behav Biomed Mater*. 2015;48:173-182.

70. Sinha Roy A, Rocha KM, Randleman JB, Stulting RD, Dupps WJ. Inverse computational analysis of invivo corneal elastic modulus change after collagen crosslinking for keratoconus. *Exp Eye Res*. 2013;113:92-104.

71. Metzler KM, Roberts CJ, Mahmoud AM, Agarwal G, Liu J. Ex vivo transepithelial collagen cross-linking in porcine and human corneas using human decorin core protein. *J Refract Surg*. 2016;32(6):410-417.

72. Elham R, Jafarzadehpur E, Hashemi H, et al. Keratoconus diagnosis using Corvis ST measured biomechanical parameters. *J Curr Ophthalmol*. 2017;29(3):175-181.

73. Alonso-Caneiro D, Karnowski K, Kaluzny BJ, Kowalczyk A, Wojtkowski M. Assessment of corneal dynamics with high-speed swept source Optical Coherence Tomography combined with an air puff system. *Opt Express*. 2011;19(15):14188.

74. Raghunathan R, Zhang J, Wu C, et al. Evaluating biomechanical properties of murine embryos using Brillouin microscopy and optical coherence tomography. *J Biomed Opt*. 2017;22(08):1.

75. Meng Z, Bustamante Lopez SC, Meissner KE, Yakovlev V V. Subcellular

measurements of mechanical and chemical properties using dual Raman-Brillouin microspectroscopy. *J Biophotonics*. 2016;9(3):201-207.

76. Koski KJ, Akhenblit P, McKiernan K, Yarger JL. Non-invasive determination of the complete elastic moduli of spider silks. *Nat Mater*. 2013;12(3):262-267.

77. Scarcelli G, Yun SH. Confocal Brillouin microscopy for three-dimensional mechanical imaging. *Nat Photonics*. 2008;2(1):39-43.

78. Palombo F, Winlove CP, Edginton RS, et al. Biomechanics of fibrous proteins of the extracellular matrix studied by Brillouin scattering. *J R Soc Interface*. 2014;11(101):20140739-20140739.

79. Zhang J, Nou XA, Kim H, Scarcelli G. Brillouin flow cytometry for label-free mechanical phenotyping of the nucleus. *Lab Chip*. 2017;17(4):663-670.

80. Besner S, Scarcelli G, Pineda R, Yun S-H, GB. B, P. S. In Vivo Brillouin Analysis of the Aging Crystalline Lens. *Investig Opthalmology Vis Sci*. 2016;57(13):5093.

81. Antonacci G, Pedrigi RM, Kondiboyina A, et al. Quantification of plaque stiffness by Brillouin microscopy in experimental thin cap fibroatheroma. *J R Soc Interface*. 2015;12(112):20150843.

82. Brillouin L. Diffusion de la lumière et des rayons X par un corps transparent homogène. *Ann Phys (Paris)*. 1922;9(17):88-122.

83. Sandercock JR. Brillouin scattering study of SbSI using a double-passed, stabilised scanning interferometer. *Opt Commun*. 1970;2(2):73-76.

84. Okamoto PR, Rehn LE, Pearson J, Bhadra R, Grimsditch M. Brillouin scattering and transmission electron microscopy studies of radiation-induced

elastic softening, disordering and amorphization of intermetallic compounds. *J Less-Common Met*. 1988;140(C):231-244.

85. Lees S, Tao NJ, Lindsay SM. Studies of compact hard tissues and collagen by means of brillouin light scattering. *Connect Tissue Res*. 1990;24(3-4):187-205.

86. Lee SA, Lindsay SM, Powell JW, et al. A Brillouin scattering study of the hydration of Li- and Na-DNA films. *Biopolymers*. 1987;26(10):1637-1665.

87. Dil JG. Brillouin scattering in condensed matter. *Reports Prog Phys*. 1982;45(3):285-334.

88. Matsui G, Kojima S, Itoh S. Rapid Brillouin Scattering Measurement of the Fast Relaxation Process in a Glass-Forming Intermediate Liquid. *Jpn J Appl Phys*. 1998;37(Part 1, No. 5B):2812-2814.

89. Itoh S, Yamana T, Kojima S. Quick Measurement of Brillouin Spectra of Glass-Forming Material Trimethylene Glycol by Angular Dispersion-Type Fabry-Perot Interferometer System. *Jpn J Appl Phys*. 1996;35(Part 1, No. 5B):2879-2881.

90. Liptak DC, Reber JC, Maguire JF, Amer MS. On the development of a confocal Rayleigh-Brillouin microscope. *Rev Sci Instrum*. 2007;78(1):016106.

91. Koski KJ, Yarger JL. Brillouin imaging. *Appl Phys Lett*. 2005;87(6):061903.

92. Scarcelli G, Yun SH. Multistage VIPA etalons for high-extinction parallel Brillouin spectroscopy. *Opt Express*. 2011;19(11):10913.

93. Kikkawa Y, Hirayama K. Uneven swelling of the corneal stroma (preliminary report). *J Japanese Ophthalmol Soc*. 1971;75(10):218-223.

94. Nikolić M, Scarcelli G. Long-term Brillouin imaging of live cells with reduced

absorption-mediated damage at 660nm wavelength. *Biomed Opt Express*. 2019;10(4):1567.

95. Kohlhaas M, Spoerl E, Schilde T, Unger G, Wittig C, Pillunat LE. Biomechanical evidence of the distribution of cross-links in corneastreated with riboflavin and ultraviolet a light. *J Cataract Refract Surg*. 2006;32(2):279-283.

96. Scarcelli G, Besner S, Pineda R, Hyun Yun S, Yun SH. Biomechanical Characterization of Keratoconus Corneas Ex Vivo With Brillouin Microscopy. *Investig Opthalmology Vis Sci*. 2014;55(7):4490.

97. Meek KM, Tuft SJ, Huang Y, et al. Changes in collagen orientation and distribution in keratoconus corneas. *Investig Ophthalmol Vis Sci*. 2005;46(6):1948-1956.

98. Shao P, Eltony AM, Seiler TG, et al. Spatially-resolved Brillouin spectroscopy reveals biomechanical abnormalities in mild to advanced keratoconus in vivo. *Sci Rep*. 2019;9(1):1-12.

99. Mofrad MRK, Kamm RD. *Cytoskeletal Mechanics: Models and Measurements*. Vol 9780521846. Cambridge University Press; 2006.

100. Scarcelli G, Polacheck WJ, Nia HT, et al. Noncontact three-dimensional mapping of intracellular hydromechanical properties by Brillouin microscopy. *Nat Methods*. 2015;12(12):1132-1134.

101. Webb JN, Su JP, Scarcelli G. Mechanical outcome of accelerated corneal crosslinking evaluated by Brillouin microscopy. *J Cataract Refract Surg*. 2017;43(11):1458-1463.

102. Sollich P, Lequeux F, Hébraud P, Cates ME. Rheology of Soft Glassy Materials. *Phys Rev Lett*. 1997;78(10):2020-2023.

103. Wu PJ, Kabakova I V., Ruberti JW, et al. Water content, not stiffness, dominates Brillouin spectroscopy measurements in hydrated materials. *Nat Methods*. 2018;15(8):561-562.

104. Shao P, Seiler TG, Eltony AM, et al. Effects of corneal hydration on brillouin microscopy in vivo. *Investig Ophthalmol Vis Sci*. 2018;59(7):3020-3027.

105. Wang Z, Chen J, Yang B. Posterior corneal surface topographic changes after laser in situ keratomileusis are related to residual corneal bed thickness. *Ophthalmology*. 1999;106(2):406-410.

106. Hammer A, Richoz O, Mosquera SA, Tabibian D, Hoogewoud F, Hafezi F. Corneal Biomechanical Properties at Different Corneal Cross-Linking (CXL) Irradiances. *Investig Opthalmology Vis Sci*. 2014;55(5):2881.

107. Chai D, Gaster RN, Roizenblatt R, Juhasz T, Brown DJ, Jester J V. Quantitative assessment of UVA-riboflavin corneal cross-linking using nonlinear optical microscopy. *Investig Ophthalmol Vis Sci*. 2011;52(7):4231-4238.

108. Kymionis GD, Tsoulnaras KI, Grentzelos MA, et al. Evaluation of corneal stromal demarcation line depth following standard and a modified-accelerated collagen cross-linking protocol. *Am J Ophthalmol*. 2014;158(4):671-675.

109. Aldahlawi NH, Hayes S, O'Brart DPS, Meek KM. Standard versus accelerated riboflavin–ultraviolet corneal collagen crosslinking: Resistance against enzymatic digestion. *J Cataract Refract Surg*. 2015;41(9):1989-1996.

110. Richoz O, Hammer A, Tabibian D, Gatzioufas Z, Hafezi F. The Biomechanical Effect of Corneal Collagen Cross-Linking (CXL) With Riboflavin and UV-A is Oxygen Dependent. *Transl Vis Sci Technol*. 2013;2(7):6.

111. Brittingham S, Tappeiner C, Frueh BE. Corneal Cross-Linking in Keratoconus Using the Standard and Rapid Treatment Protocol: Differences in Demarcation Line and 12-Month Outcomes. *Invest Ophthalmol Vis Sci*. 2014;55(12):8371-8376.

112. Ruberti JW, Sinha Roy A, Roberts CJ. Corneal Biomechanics and Biomaterials. *Annu Rev Biomed Eng*. 2011;13(1):269-295.

113. Kymionis GD, Portaliou DM, Diakonis VF, Kounis GA, Panagopoulou SI, Grentzelos MA. Corneal Collagen Cross-linking With Riboflavin and Ultraviolet-A Irradiation in Patients With Thin Corneas. *Am J Ophthalmol*. 2012;153(1):24-28.

114. Sachdev G, Sachdev M. Recent advances in corneal collagen cross-linking. *Indian J Ophthalmol*. 2017;65(9):787.

115. Kashiwabuchi RT, Quinto GG, Castro-Combs J, Behrens A. Corneal Collagen Cross-linking with Riboflavin/Lumiflavin and Blue Light (450nm) to Reduce Posterior Lamellar Dislocation in Endothelium Keratoplasty. In: *ARVO Annual Meeting Abstract.* ; 2009:5495.

116. Wollensak G, Spoerl E, Wilsch M, Seiler T. Keratocyte Apoptosis after Corneal Collagen Cross-linking Using Riboflavin/UVA Treatment. *Cornea*. 2004;23(1):43-49.

117. Olsen T. Light scattering from the human cornea. *Invest Ophthalmol Vis Sci*.

1982;23(1):81-86.

118. Spadea L, Maraone G, Verboschi F, Vingolo EM, Tognetto D. Effect of corneal light scatter on vision: a review of the literature. *Int J Ophthalmol*. 2016;9(3):459-464.

119. Seifert J, Hammer CM, Rheinlaender J, et al. Distribution of young's modulus in porcine corneas after riboflavin/UVA-induced collagen cross-linking as measured by atomic force microscopy. *PLoS One*. 2014;9(1):88186.

120. Chalmers RL. A review of the metabolism of hydrogen peroxide by external ocular structures. *Int Contact Lens Clin*. 1995;22(7-8):143-147.

121. Beckman Rehnman J, Janbaz CC, Behndig A, Lindén C. Spatial distribution of corneal light scattering after corneal collagen crosslinking. *J Cataract Refract Surg*. 2011;37(11):1939-1944.

122. Wollensak G, Wilsch M, Spoerl E, Seiler T. Collagen Fiber Diameter in the Rabbit Cornea After Collagen Crosslinking by Riboflavin/UVA. *Cornea*. 2004;23(5):503-507.

123. USHIKI T. Collagen Fibers, Reticular Fibers and Elastic Fibers. A Comprehensive Understanding from a Morphological Viewpoint. *Arch Histol Cytol*. 2002;65(2):109-126.

124. Meek KM, Knupp C. Corneal structure and transparency. *Prog Retin Eye Res*. 2015;49:1-16.

125. Pallikaris IG, Kymionis GD, Astyrakakis NI. *Corneal Ectasia Induced by Laser in Situ Keratomileusis*. Vol 27. No longer published by Elsevier; 2001:1796-1802.

126. Tervo TM, Amoils SP. Iatrogenic keratectasia after laser in situ keratomileusis [2] (multiple letters). *J Cataract Refract Surg*. 2001;27(4):490-491.

127. Wollensak G. Crosslinking treatment of progressive keratoconus: new hope. *Curr Opin Ophthalmol*. 2006;17(4):356-360.

128. Li J, Singh M, Han Z, et al. Revealing anisotropic properties of cornea at different intraocular pressures using optical coherence elastography. In: Larin K V., Sampson DD, eds. ; 2016:97100T.

129. Latour G, Gusachenko I, Kowalczuk L, Lamarre I, Schanne-Klein M-C. In vivo structural imaging of the cornea by polarization-resolved second harmonic microscopy. *Biomed Opt Express*. 2012;3(1):1.

130. Morishige N, Wahlert AJ, Kenney MC, et al. Second-harmonic imaging microscopy of normal human and keratoconus cornea. *Investig Ophthalmol Vis Sci*. 2007;48(3):1087-1094.

131. Winkler M, Shoa G, Xie Y, et al. Three-dimensional distribution of transverse collagen fibers in the anterior human corneal stroma. *Investig Ophthalmol Vis Sci*. 2013;54(12):7293-7301.

132. Hatami-Marbini H, Etebu E. A new method to determine rate-dependent material parameters of corneal extracellular matrix. *Ann Biomed Eng*. 2013;41(11):2399-2408.

133. McKee CT, Last JA, Russell P, Murphy CJ. Indentation versus tensile measurements of young's modulus for soft biological tissues. *Tissue Eng - Part B Rev*. 2011;17(3):155-164.

134. Hatami-Marbini H, Etebu E. An experimental and theoretical analysis of

unconfined compression of corneal stroma. *J Biomech*. 2013;46(10):1752-1758.

135. Hatami-Marbini H. Viscoelastic shear properties of the corneal stroma. *J Biomech*. 2014;47(3):723-728.

136. Hatami-Marbini H, Rahimi A. The relation between hydration and mechanical behavior of bovine cornea in tension. *J Mech Behav Biomed Mater*. 2014;36:90-97.

137. Singh M, Han Z, Li J, et al. Quantifying the effects of hydration on corneal stiffness with noncontact optical coherence elastography. *J Cataract Refract Surg*. 2018;44(8):1023-1031.

138. Dias J, Ziebarth NM. Impact of hydration media on ex vivo corneal elasticity measurements. In: *Eye and Contact Lens*. Vol 41. Lippincott Williams and Wilkins; 2015:281-286.

139. Greenstein SA, Shah VP, Fry KL, Hersh PS. Corneal thickness changes after corneal collagen crosslinking for keratoconus and corneal ectasia: One-year results. *J Cataract Refract Surg*. 2011;37(4):691-700.

140. Kontadakis GA, Ginis H, Karyotakis N, et al. In vitro effect of corneal collagen cross-linking on corneal hydration properties and stiffness. *Graefe's Arch Clin Exp Ophthalmol*. 2013;251(2):543-547.

141. Hayes S, Boote C, Kamma-Lorger CS, et al. Riboflavin/UVA Collagen Cross-Linking-Induced Changes in Normal and Keratoconus Corneal Stroma. Connon CJ, ed. *PLoS One*. 2011;6(8):e22405.

142. Webb JN, Langille E, Hafezi F, Randleman JB, Scarcelli G. Biomechanical

impact of localized corneal cross-linking beyond the irradiated treatment area. *J Refract Surg*. 2019;35(4):253-260.

143. Eltony AM, Clouser F, Shao P, Pineda R, Yun S-H. Brillouin Microscopy Visualizes Centralized Corneal Edema in Fuchs Endothelial Dystrophy. *Cornea*. October 2019:1.

144. Mercatelli R, Mattana S, Capozzoli L, et al. Morpho-mechanics of human collagen superstructures revealed by all-optical correlative micro-spectroscopies. *Commun Biol*. 2019;2(1):1-10.

145. He X, Liu J. A Quantitative Ultrasonic Spectroscopy Method for Noninvasive Determination of Corneal Biomechanical Properties. *Investig Opthalmology Vis Sci*. 2009;50(11):5148.

146. Ortiz S, Siedlecki D, Grulkowski I, et al. Optical distortion correction in Optical Coherence Tomography for quantitative ocular anterior segment by three-dimensional imaging. *Opt Express*. 2010;18(3):2782.

147. Berghaus K V., Yun SH, Scarcelli G. High Speed Sub-GHz Spectrometer for Brillouin Scattering Analysis. *J Vis Exp*. 2015;(106):e53468.

148. Hodson S, O'Leary D, Watkins S. The measurement of ox corneal swelling pressure by osmometry. *J Physiol*. 1991;434(1):399-408.

149. Cusack S, Miller A. Determination of the elastic constants of collagen by Brillouin light scattering. *J Mol Biol*. 1979;135(1):39-51.

150. Scarcelli G, Yun SH. Reply to 'Water content, not stiffness, dominates Brillouin spectroscopy measurements in hydrated materials.' *Nat Methods*. 2018;15(8):562-563.

151. Pircher N, Beer F, Holzer S, et al. Large Field of View Corneal Epithelium and Bowman's Layer Thickness Maps in Keratoconic and Healthy Eyes. *Am J Ophthalmol*. 2020;209:168-177.

152. Beer F, Patil RP, Sinha-Roy A, Baumann B, Pircher M, Hitzenberger CK. Ultrahigh resolution polarization sensitive optical coherence tomography of the human cornea with conical scanning pattern and variable dispersion compensation. *Appl Sci*. 2019;9(20):4245.

153. Piñero DP, Alio JL, Barraquer RI, Michael R, Jiménez R. Corneal biomechanics, refraction, and corneal aberrometry in keratoconus: An integrated study. *Investig Ophthalmol Vis Sci*. 2010;51(4):1948-1955.

154. Edmund C. Corneal topography and elasticity in normal and keratoconic eyes. A methodological study concerning the pathogenesis of keratoconus. *Acta Ophthalmol Suppl (Oxf)*. 1989;193:1-36.

155. Webb JN, Zhang H, Roy AS, Randleman JB, Scarcelli G. Detecting mechanical anisotropy of the cornea using brillouin microscopy. *Transl Vis Sci Technol*. 2020;9(7):1-11.

156. Hatami-Marbini H, Etebu E. Hydration dependent biomechanical properties of the corneal stroma. *Exp Eye Res*. 2013;116:47-54.

157. Mow VC, Kuei SC, Lai WM, Armstrong CG. Biphasic creep and stress relaxation of articular cartilage in compression: Theory and experiments. *J Biomech Eng*. 1980;102(1):73-84.

158. Mak AF, Lai WM, Mow VC. Biphasic indentation of articular cartilage-I. Theoretical analysis. *J Biomech*. 1987;20(7):703-714.

159. Doughty MJ, Zaman ML. Human corneal thickness and its impact on intraocular pressure measures: A review and meta-analysis approach. *Surv Ophthalmol*. 2000;44(5):367-408.

160. Bilaniuk N, Wong GSK. Speed of sound in pure water as a function of temperature. *J Acoust Soc Am*. 1993;93(3):1609-1612.

161. Leonard DW, Meek KM. Refractive indices of the collagen fibrils and extrafibrillar material of the corneal stroma. *Biophys J*. 1997;72(3):1382-1387.

162. Meek KM, Dennis S, Khan S. Changes in the refractive index of the stroma and its extrafibrillar matrix when the cornea swells. *Biophys J*. 2003;85(4):2205-2212.

163. Danielsson M, Parks DM, Boyce MC. Constitutive modeling of porous hyperelastic materials. *Mech Mater*. 2004;36(4):347-358.

164. Gao X, Gu W. A new constitutive model for hydration-dependent mechanical properties in biological soft tissues and hydrogels. *J Biomech*. 2014;47(12):3196-3200.

165. Holz M, Heil SR, Sacco A. Temperature-dependent self-diffusion coefficients of water and six selected molecular liquids for calibration in accurate 1H NMR PFG measurements. *Phys Chem Chem Phys*. 2000;2(20):4740-4742.

166. Gu WY, Yao H, Huang CY, Cheung HS. New insight into deformation-dependent hydraulic permeability of gels and cartilage, and dynamic behavior of agarose gels in confined compression. *J Biomech*. 2003;36(4):593-598.

167. Rosenblat E, Hersh PS. Intraoperative corneal thickness change and clinical outcomes after corneal collagen crosslinking: Standard crosslinking versus

hypotonic riboflavin. *J Cataract Refract Surg*. 2016;42(4):596-605.

168. Hatami-Marbini H, Jayaram SM. Effect of UVA/riboflavin collagen crosslinking on biomechanics of artificially swollen corneas. *Investig Ophthalmol Vis Sci*. 2018;59(2):764-770.

169. Søndergaard AP, Ivarsen A, Hjortdal J. Corneal resistance to shear force after UVA-riboflavin cross-linking. *Investig Ophthalmol Vis Sci*. 2013;54(7):5059-5069.

170. Shah S, Laiquzzaman M, Bhojwani R, Mantry S, Cunliffe I. Assessment of the Biomechanical Properties of the Cornea with the Ocular Response Analyzer in Normal and Keratoconic Eyes. *Investig Opthalmology Vis Sci*. 2007;48(7):3026.

171. Touboul D, Bénard A, Mahmoud AM, Gallois A, Colin J, Roberts CJ. Early biomechanical keratoconus pattern measured with an ocular response analyzer: Curve analysis. *J Cataract Refract Surg*. 2011;37(12):2144-2150.

172. Bak-Nielsen S, Pedersen IB, Ivarsen A, Hjortdal J. Dynamic scheimpflug-based assessment of keratoconus and the effects of corneal cross-linking. *J Refract Surg*. 2014;30(6):408-414.

173. Elsheikh A, Kassem W, Jones SW. Strain-rate sensitivity of porcine and ovine corneas. *Acta Bioeng Biomech*. 2011;13(2):25-36.

174. Boyce BL, Jones RE, Nguyen TD, Grazier JM. Stress-controlled viscoelastic tensile response of bovine cornea. *J Biomech*. 2007;40(11):2367-2376.